The Pennsylvania State University

The Graduate School

INDIRECT HYBRID MANUFACTURING – INTEGRATING 3D SAND-PRINTING FOR METAL CASTING

A Thesis in

Additive Manufacturing and Design

by

Daniel Sebastian Martinez Lepp

Submitted in Partial Fulfillment
of the Requirements
for the Degree of

Master of Science

December 2019

The thesis of Daniel Sebastian Martinez Lepp was reviewed and approved* by the following:

Guha P. Manogharan
Assistant Professor of Mechanical and Nuclear Engineering
Thesis Advisor

Robert Voigt
Professor of Industrial and Manufacturing Engineering

Timothy W. Simpson
Paul Morrow Professor of Engineering Design and Manufacturing
Director of the Additive Manufacturing and Design Graduate Program

*Signatures are on file in the Graduate School

ABSTRACT

Additive manufacturing (AM) has been demonstrated to be a transformative technology for rapid manufacturing from three-dimensional digital models. Due to the disruptive nature of the technology, its integration into manufacturing settings is still difficult to assess. Factors like the large upfront investment required and limited number of certified materials (specially for metal components) available represent challenges for its adoption in industry at a larger scale. One manufacturing sector where these difficulties are lessened is the metal casting industry. The American Foundry Society (AFS) estimates that the metal casting industry amounts to 33.7 billion USD and within the United States, employs directly about 200,000 people. Binder jetting technology and specifically 3D sand-printing (3DSP) offers the possibility of leveraging the freedom of design of AM using comparatively low-cost materials (i.e., silica sand vs. metallic powders) to enhance casting performance. By printing the sand mold, the full range of metals and alloys already qualified for conventional casting applications can continue to be used without any need for further certification.

Two important opportunities for reducing casting defects arise when using 3DSP. In the first case, the ability to manufacture complex mold geometries previously unfeasible using conventional methods, means that the flow of liquid metal or alloy circulating through the mold can be controlled by designing rigging components that direct the flow in accordance with predetermined conditions. These design criterions can be set by running numerical simulations of the filling process. In this thesis, the effectiveness of novel sprue geometries designed mathematically for alloys of different flow and solidification behavior is examined. The use of these sprues is simulated and experimentally tested for alloys at separate ends of the freezing range (i.e., gray cast iron Class 30, a very short-freezing range alloy and aluminum alloy 319, a very long-

freezing range alloy). Computed tomography (CT) scanning, scanning electron microscopy and three-point bending tests are used to characterize the results in each sprue case.

The casting mechanical properties can also be altered by controlling cooling behavior of the casting. Due to the layer-by-layer nature of binder and sand deposition in the 3DSP process, precise control on the thermo-physical properties of the mold such as thermal conductivity, thermal diffusivity, permeability and mechanical strength can be achieved. The second part of this thesis presents experimental procedures used to characterize 3DSP samples obtained from different printing conditions. Permeability and mechanical properties of the mold are examined using AFS standards. Thermal properties are obtained using laboratory techniques to determine thermal conductivity and diffusivity. Casting experiments are monitored to obtain thermal properties using a linear model to solve the backward heat conduction problem. The mechanical and microstructural properties of pure aluminum samples casted using the 3DSP molds are examined using three-point bending and microscopy of etched samples. A framework for integrating these thermomechanical properties into a design loop for metal casting mold design is proposed.

Finally, 3DSP samples are examined using micro computed tomography scanning. This technique allows for the creation of a 3D model of the sand mold to determine void spaces and pore interconnectedness. An understanding of the pore network properties of 3DSP samples and how printing conditions affect mold permeability are essential to creating defect-free castings. During mold filling, air present in the mold and gasses generated by the binder burn-out must be evacuated through the mold. Insufficient void space and pore interconnectedness will lead to the appearance of a backpressure within the mold. If this happens, then volumes within the mold will remain unfilled, creating serious casting defects. Samples printed using different printing parameters are examined via CT scanning and permeability simulations are performed to create an understanding of how air flow through the mold occurs.

TABLE OF CONTENTS

LIST OF TABLES

LIST OF FIGURES

ABREVIATIONS AND NOMENCLATURE

η	Absolute Viscosity (mPa.s)
AM	Additive Manufacturing
AFS	American Foundry Society
ASTM	American Society of Testing & Materials
α, r	Angular Frequency and Radius of the Conical-Helix
F	Applied Force on Sample in Three-Point Bending Test
CT	Computed Tomography
CHC	Conical-Helix Sprue Design Casting
DfAM	Design for Additive Manufacturing
EDS	Energy Dispersive X-Ray Spectroscopy
C_{air}	Entrainment Rate Sensitivity Coefficient
σ_{flex}	Flexural Stress in Three-Point Bending Test
ρ	Fluid Density (kg/m^3)
a, b	Geometric Parameters of the Parabolic Profile
GFN	Grain Fineness Number
g_n	Gravity Normal to Melt Surface (m/s^2)
LSD	Least Significant Difference Test
L	Length Between Supports in Three-Point Bending Test
LOI	Loss on Ignition Test
Me	Maximum Entropy algorithm
T_m	Melting Temperature (K)
MIP	Mercury Intrusion Porosimetry

PC	Parabolic Sprue Design Casting
PNM	Pore Network Model
Re	Rényi Entropy Algorithm
SEM	Scanning Electron Microscopy
SC	Straight Sprue Design Casting
σ	Surface Tension Coefficient (kg/s^2)
3DSP	Three-Dimensional Sand-Printing
3PB	Three-Point Bending Test
t	Three-Point Bending Test Sample Thickness
w	Three-Point Bending Test Sample Width
h_{sprue}	Total Sprue Height (m)
TPS	Transient Plane Source Technique
k	Turbulence Kinetic Energy (J/kg)
L_t	Turbulence Length Scale (m)
UFS	Ultimate Flexural Strength (MPa)
UTS	Ultimate Tensile Strength (MPa)
∀	Volume of Air (m^3)
YMT	Yen Multilevel Thresholding Algorithm

ACKNOWLEDGEMENTS

Firstly, I thank God, who has given me immeasurably more than I could ask for or imagine. I thank my parents and brother for supporting me throughout all my graduate studies. I am deeply indebted to my advisor Dr. Guha Manogharan, for welcoming me into his research team, for his encouraging support and for sharing important insight during my research.

I am grateful to Dr. Timothy Simpson, for his shared insight in the classroom and during the preparation of this thesis. I would like to express my thanks to Dr. Robert Voigt, for his offering his time and knowledge into refining my research project and this thesis.

I am thankful to professors and fellow researchers who have contributed to this work in one way or another, to Dr. Todd Palmer, Andrew Iams, Timothy Stecko, and Shawn Siroka, among others.

I am also grateful to members of my lab and friends who collaborated directly or indirectly in my research with their support and constructive criticism, to Santosh, Xi, Hakan, Maryam, Greg, Casey, Jay, Nick, and Phil. I also thank friends I have made outside of my academic and research related tasks, to Alex Versiput, and Jade and Jomara Sandbulte. Their support has been invaluable to me.

Finally, I would like to thank LASPAU, the Fulbright Scholarship and the scholarship Beca Carlos Antonio López (BECAL) for sponsoring my graduate studies at Penn State University.

Chapter 1

Introduction

Additive manufacturing (AM) technology as defined by the ASTM F42 standard introduces the concept of creating components beginning from a 3D design [1]. The possibility of materializing models directly from parametric data has driven both designers and manufacturers towards a paradigm shift, where rapid iteration and versatility allow earlier quality outputs [2]. Manufacturing platforms for metallic components via AM have been commercially available since the middle of the 1990's [3,4]. However, difficulties such as post-processing [5], material certification [6] and lack of standards remain challenges for massive adoption of direct metal AM. One of the proposed solutions is its implementation via a hybrid manufacturing approach [7]. Among hybrid-AM processes, the combined use of binder jetting technology and metal casting has demonstrated to be as a highly productive and efficient method for fabrication of metallic components [8], both via investment and sand casting [9]. A hybrid framework in metal sand casting introduces the intrinsic advantages of AM such as: (1) design complexity, opening opportunities for part consolidation and topology optimization [10,11]; (2) by using simulation software in combination with the freedom of mold design, optimum melt-flow conditions can be created during pouring to minimize defect formation [11,12]; and (3) reductions in manufacturing lead times [13].

Casting represents one of the oldest manufacturing techniques for producing metal parts, dating back to 3000-3500 BC [14]. This class of manufacturing includes processes such as gravity sand casting, low-pressure sand casting, lost foam and investment casting. In all cases, the metallic component is created by pouring metal within a cavity and letting it solidify. On a worldwide scale, it is estimated that 1.2 million tons of steel products were manufactured via casting only in 2017

[15]. The American Foundry Society (AFS) estimates that within the United States over 6.9 million tons of iron alloys were cast in 2016 [16]. As of the year 2019, the same organization states that the metalcasting industry amounts to 33.7 billion USD and employs directly about 200,000 people. Metal sand casting consist in using an expendable sand mold that is shaped using patterns that are imprinted on the sand that is either mixed with chemical binding agents or water. The mold is then assembled, and in some cases, cores are used to create internal features. After pouring the molten metal, the mold is cooled down and broken to extract the metal component [14]. The basic parts in a conventional sand-casting mold are seen in Fig. 1-1. The casted part cavity is divided in two sections, where the top side of the mold is called cope, and the bottom side is called drag. Runners and sprues are responsible for directing the molten metal from the top of the mold to the cavity and can be either shaped using patterns or by carving the sand. The function of the riser is to serve as a reservoir of molten material that can feed the casting during the solidification phase, during which most alloys will tend to shrink. Sand cores are generally fabricated using patterns and the sand is kept together by using binders [17].

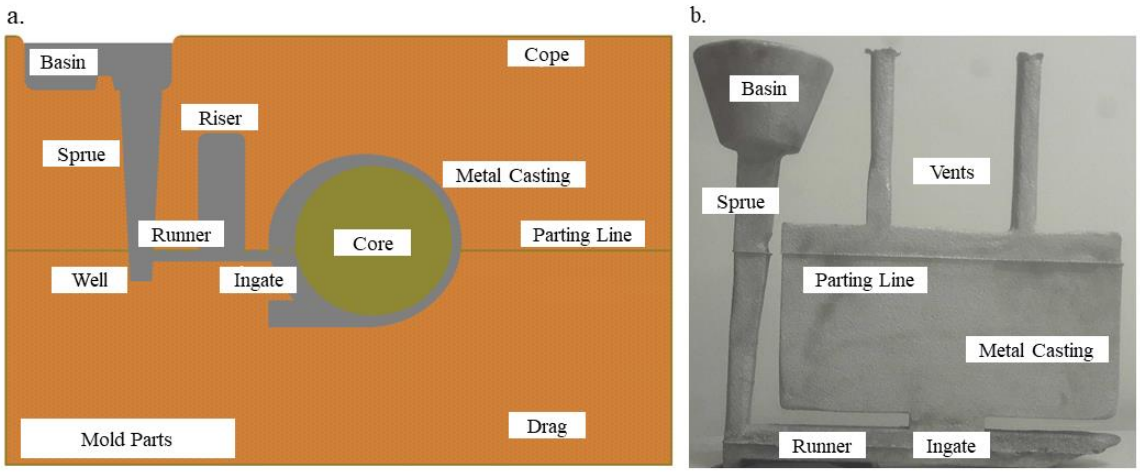

Figure 1-1. (a) Main mold components and (a) how they are seen in an actual metal casting

Binder jetting additive manufacturing consists in a layer-by-layer deposition of a porous material with binder in consecutive steps building a component [18]. Developed in the late 1980's [19], the technology has since been adopted to print components in metal [20–24], ceramics [25,26] and plastics [27]. In the case of 3DSP, parameters that can be modified during the printing process include recoater speed, layer thickness, frequency of activation of the binder head [28–30]. All of these have been demonstrated to affect the mechanical characteristics of the built mold. These properties can also be modified by changing the binder composition [31–33], type and size of the sand grains [34] and by performing curing processes after printing [35]. Two main types of commercial systems are available up to date. The main difference between these is the fact that in systems such as the ExOne [36] and Voxeljet [37] family of printers, the building box is enclosed within the printing machine. The second type of printers are built using off-the-shelf robotic arms that are adapted to perform the functions of sand deposition, layer leveling and binder deposition. Among these is the Viridis3D RAM [38] system, used this study. Fig. 1-2 represents the three basic functions and the general setup of the system.

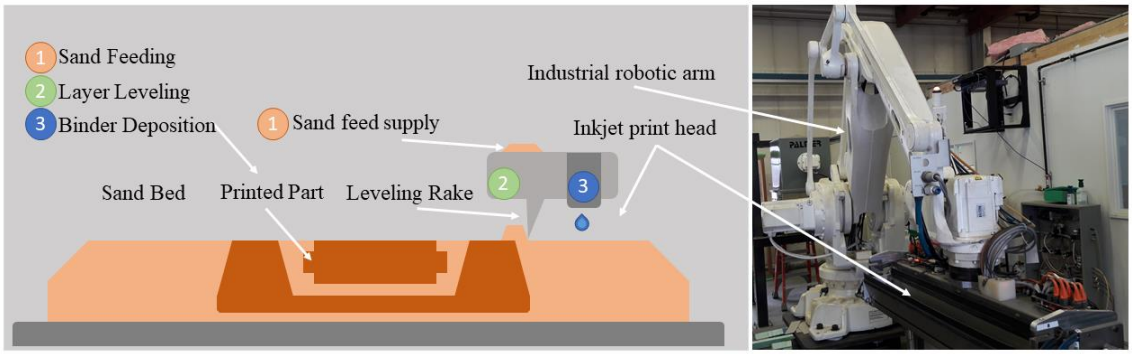

Figure 1-2. Functions performed during 3DSP process

The first part of this thesis deals with the mechanical properties of sand molds, the objective is to determine optimum binder concentration levels that will increase mold strength, while maintaining proper pore network properties that allow for maximum degassing. These results

represent the first phase in developing functionally graded sand molds that can be optimized for proper strength and degassing, engineered thermal behavior and minimum binder usage.

A second approach to taking advantage of the freedom of design offered by 3DSP, is explored in the second section of this work. In this case, the effect of a novel approach to sprue design on alloy systems of very different flowing and solidification characteristics. These alloys are expected to have dissimilar behaviors given their chemical composition and physical properties. Aluminum alloy 319 is used as a representative of long-freezing alloys, types of alloys that pass from liquid to solid via an intermediate state sometimes called mushy-zone [39,40]. This solidification behavior leads to the appearance of micro porosity finely dispersed across the casting as well as very short feeding distances [41]. Aluminum alloys are also known to be highly sensitive to turbulence during the filling process, tending to form oxide layers that are the origin of defects within the casting [42,43]. The alloys of long-freezing range are represented in this study by pouring gray iron Class 30. Gray iron solidifies from the outer walls inward, as is typical of long-freezing range alloys that do not have the mushy transition zone [44]. The chemistry of gray iron also makes it less sensitive to the formation of oxides at very high pouring temperatures, but as the melt begins to cool during filling, oxide bifilms will appear and result in casting defects [17,45]. Fig. 1-3 presents a graphical organization of this thesis.

Chapter 2 presents an experimental characterization of 3DSP molds printed using different binder concentrations, noting its effects on mechanical strength, permeability and thermal properties of the sand molds. These mold properties have been shown to be governed by binder proportions for different printing systems [25,46–48]. However, no previous published results exist on the mold properties printed on a VIRIDIS 3D RAM system. This work also represents the first know efforts to determine thermal properties of 3DSP molds, to the authors knowledge. Finally, a framework for developing functionally graded 3DSP molds using experimental data with numerical modeling for optimized strength, permeability and thermal properties is proposed.

Chapter 3 focuses on the effects of binder concentration on the permeability of 3DSP molds. Micro-computed tomography scanning is used to create 3D image data of molds manufactured using different printing parameters. This image data is then examined, and an in-depth pore network characterization is performed using image analysis tools. Numerical simulations of air flow across the samples are run, to describe flow patterns and levels of permeability for each mold type.

Chapter 4 describes casting experiments performed using analytically developed sprue designs and their effect on mechanical properties of two alloys on different ends of the freezing range spectrum. The objective was to extend previously developed work using the same procedure for a single alloy of intermediate fluidity characteristics [49]. Various characterizing techniques are used to evaluate the effectiveness of the novel sprue designs in reducing defect formation during mold filling. Numerical simulations are presented modeling the differing filling process of these two alloys.

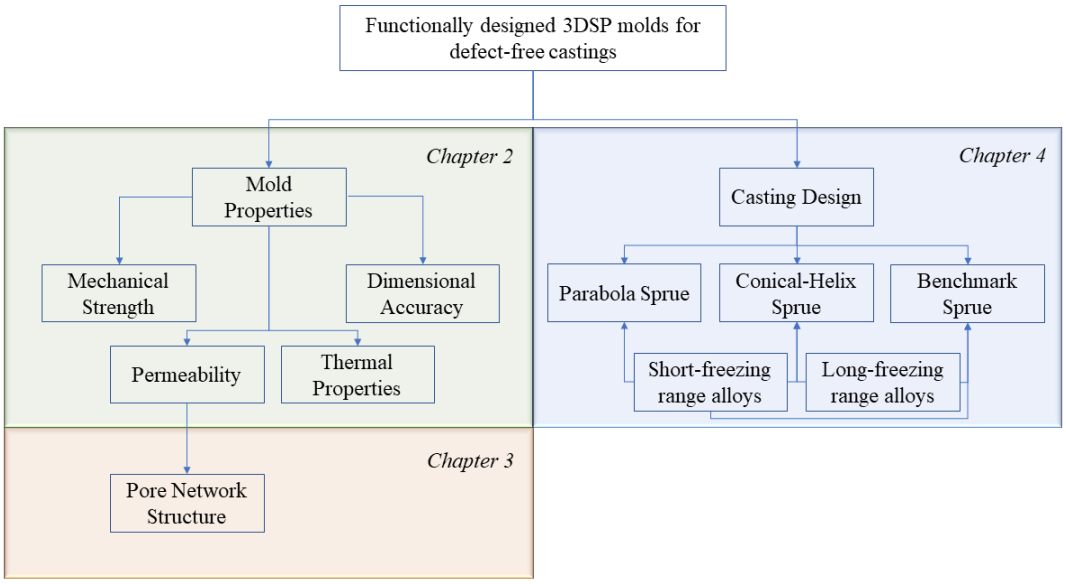

Figure 1-3. Chapter organization

References

[1] ASTM International. ASTM F2792-12a. Rapid Manuf Assoc 2013:1–3. doi:10.1520/F2792-12A.2.

[2] Rayna T, Striukova L. From rapid prototyping to home fabrication: How 3D printing is changing business model innovation. Technol Forecast Soc Change 2016;102:214–24. doi:10.1016/j.techfore.2015.07.023.

[3] Wohlers T. Rapid Prototyping & Tooling State of the Industry: 1998 Worldwide Progress Report. Mater Technol 1998;13:174–6. doi:10.1080/10667857.1998.11752797.

[4] Inovar Communications Ltd. Background to Additive Manufacturing. Met AM n.d. https://www.metal-am.com/introduction-to-metal-additive-manufacturing-and-3d-printing/background-to-additive-manufacturing/ (accessed September 18, 2019).

[5] Kochan D, Kai CC, Zhaohui D. Rapid prototyping issues in the 21st century. Comput Ind 1999;39:3–10. doi:10.1016/S0166-3615(98)00125-0.

[6] Seifi M, Salem A, Beuth J, Harrysson O, Lewandowski JJ. Overview of Materials Qualification Needs for Metal Additive Manufacturing. JOM 2016;68:747–64. doi:10.1007/s11837-015-1810-0.

[7] Karunakaran KP, Bernard A, Suryakumar S, Dembinski L, Taillandier G. Rapid manufacturing of metallic objects. Rapid Prototyp J 2012;18:264–80. doi:10.1108/13552541211231644.

[8] Rosochowski A, Matuszak A. Rapid tooling: the state of the art. J Mater Process Technol 2000;106:191–8. doi:10.1016/S0924-0136(00)00613-0.

[9] Chhabra M, Singh R. Rapid casting solutions: A review. Rapid Prototyp J 2011;17:328–50. doi:10.1108/13552541111156469.

[10] Wang J. Part Design and Topology Optimizationfor Rapid Sand and Investment Casting.,

M.Sc. Thesis Engineering Design, Pennsylvania State University, 2017.

[11] Sama SR, Wang J, Manogharan G. Non-conventional mold design for metal casting using 3D sand-printing. J Manuf Process 2018;34:765–75. doi:https://doi.org/10.1016/j.jmapro.2018.03.049.

[12] Sama SR, Badamo T, Lynch P, Manogharan G. Novel sprue designs in metal casting via 3D sand-printing. Addit Manuf 2019;25:563–78. doi:10.1016/J.ADDMA.2018.12.009.

[13] Almaghariz ES, Conner BP, Lenner L, Gullapalli R, Manogharan GP, Lamoncha B, Fang, M. Quantifying the Role of Part Design Complexity in Using 3D Sand Printing for Molds and Cores. Int J Met 2016;10:240–52. doi:10.1007/s40962-016-0027-5.

[14] Ravi B. Metal casting: computer-aided design and analysis. PHI Learning Pvt. Ltd.; 2005.

[15] World Steel Association. World Steel in Figures 2018. Brussels: 2018.

[16] WFO. WFO Global Foundry Report. 2018.

[17] Campbell J. Castings. 2nd Editio. Oxford: Butterworth-Heinemann; 2003.

[18] Sachs E, Cima M, Cornie J, Brancazio D, Bredt J, Curodeau A, Fan, T, Khanuja, S, Lauder, A, Lee, J, Michaels, S. Three-Dimensional Printing: The Physics and Implications of Additive Manufacturing. CIRP Ann - Manuf Technol 1993;42:257–60. doi:10.1016/S0007-8506(07)62438-X.

[19] Sachs EM, Haggerty JS, Cima MJ, Williams PA. Three-dimensional printing techniques 1993.

[20] Mostafaei A, Stevens EL, Hughes ET, Biery SD, Hilla C, Chmielus M. Powder bed binder jet printed alloy 625: Densification, microstructure and mechanical properties. Mater Des 2016;108:126–35. doi:10.1016/j.matdes.2016.06.067.

[21] Rojas-Nastrucci EA, Nussbaum JT, Crane NB, Weller TM. Ka-Band Characterization of Binder Jetting for 3-D Printing of Metallic Rectangular Waveguide Circuits and Antennas. IEEE Trans Microw Theory Tech 2017;65:3099–108. doi:10.1109/TMTT.2017.2730839.

[22] Mostafaei A, Behnamian Y, Krimer YL, Stevens EL, Luo JL, Chmielus M. Brief data overview of differently heat treated binder jet printed samples made from argon atomized alloy 625 powder. Data Br 2016;9:556–62. doi:10.1016/j.dib.2016.09.042.

[23] Seetharaman S, Krishnan M, Goh F, Wen C, Khan NA, Lai, G. Research Updates on the Additive Manufacturing of Nickel Based Superalloys. Solid Free. Fabr. 2016 Proc. 27th Annu. Int. Solid Free. Fabr. Symp. – An Addit. Manuf. Conf., 2016, p. 469–86.

[24] Nandwana P, Elliott AM, Siddel D, Merriman A, Peter WH, Babu SS. Powder bed binder jet 3D printing of Inconel 718: Densification, microstructural evolution and challenges. Curr Opin Solid State Mater Sci 2017;21:207–18. doi:10.1016/j.cossms.2016.12.002.

[25] Mitra S, Rodríguez de Castro A, El Mansori M. On the rapid manufacturing process of functional 3D printed sand molds. J Manuf Process 2019;42:202–12. doi:10.1016/j.jmapro.2019.04.034.

[26] Butscher A, Bohner M, Roth C, Ernstberger A, Heuberger R, Doebelin N, von Rohr, PR, Muller, R. Printability of calcium phosphate powders for three-dimensional printing of tissue engineering scaffolds. Acta Biomater 2012;8:373–85. doi:10.1016/j.actbio.2011.08.027.

[27] Lauridsen H, Hansen K, Nørgård MØ, Wang T, Pedersen M. From tissue to silicon to plastic: three-dimensional printing in comparative anatomy and physiology. R Soc Open Sci 2016;3:150643. doi:10.1098/rsos.150643.

[28] Coniglio N, Sivarupan T, El Mansori M. Investigation of process parameter effect on anisotropic properties of 3D printed sand molds. Int J Adv Manuf Technol 2018;94:2175–85. doi:10.1007/s00170-017-0861-5.

[29] Sivarupan T, El Mansori M, Daly K, Mavrogordato MN, Pierron F. Characterisation of 3D printed sand moulds using micro-focus X-ray computed tomography. Rapid Prototyp J 2019;25:404–16. doi:10.1108/RPJ-04-2018-0091.

[30] Mitra S, Rodríguez de Castro A, El Mansori M. On the rapid manufacturing process of functional 3D printed sand molds. J Manuf Process 2019;42:202–12. doi:10.1016/J.JMAPRO.2019.04.034.

[31] Stauder BJ, Kerber H, Schumacher P. Foundry sand core property assessment by 3-point bending test evaluation. J Mater Process Technol 2016;237:188–96. doi:https://doi.org/10.1016/j.jmatprotec.2016.06.010.

[32] Thole J, Beckermann C. Measurement of Elastic Modulus of PUNB Bonded Sand as a Function of Temperature. Int J Met 2010;4:7–18. doi:10.1007/BF03355499.

[33] Fox JT, Cannon FS, Brown NR, Huang H, Furness JC. Comparison of a new, green foundry binder with conventional foundry binders. Int J Adhes Adhes 2012;34:38–45. doi:https://doi.org/10.1016/j.ijadhadh.2011.11.011.

[34] Tsumura O, Narita H, Tomigashi D, Okino M, Miyauchi K. Effects of sand grain size distribution on strength of mold. J Japan Foundry Eng Soc 2009;81:77–82. doi:https://doi.org/10.11279/jfes.81.77.

[35] Mitra S, Rodríguez de Castro A, El Mansori M. The effect of ageing process on three-point bending strength and permeability of 3D printed sand molds. Int J Adv Manuf Technol 2018;97:1241–51. doi:10.1007/s00170-018-2024-8.

[36] ExOne. Sand 3D Printers n.d. https://www.exone.com/en-US/3D-printing-systems/sand-3d-printers (accessed September 24, 2019).

[37] Voxeljet. 3D Printing with Sand: Fast and Economical Sand Molds n.d. https://www.voxeljet.com/anwendungen/sandguss/ (accessed September 24, 2019).

[38] EnvisionTEC. Viridis3D n.d. https://envisiontec.com/3d-printers/robotic-additive-manufacturing/ (accessed September 24, 2019).

[39] Reis A, Xu ZA, Tol R V, Houbaert Y, Duarte JF, Santos AD, Magalhaes, AB. Model for prediction of shrinkage defects in long and short freezing range materials. Int J Cast Met

Res 2007;20:171–5. doi:10.1179/136404607X239771.

[40] Reis A, Houbaert Y, Xu Z, Tol R Van, Santos AD, Duarte JF, Magalhaes, AB. Modeling of shrinkage defects during solidification of long and short freezing materials. J Mater Process Technol 2008;202:428–34. doi:https://doi.org/10.1016/j.jmatprotec.2007.10.030.

[41] Sigworth GK, Wang C. Evolution of porosity in long freezing range alloys. Metall Trans B 1993;24:365–77. doi:10.1007/BF02659139.

[42] Campbell J. Entrainment defects. Mater Sci Technol 2006;22:127–45. doi:10.1179/174328406X74248.

[43] Runyoro J, Boutorabi SMA, Campbell J. Critical gate velocities for film-forming casting alloys. A basis for process specification. Trans Am Foundrymens Soc 1992;100:225–34.

[44] Campbell J. Review of fluidity concepts in casting. Cast Met 1995;7:227–37. doi:10.1080/09534962.1995.11819183.

[45] Modaresi A, Safikhani A, Noohi A, Hamidnezhad N, Mostafa Maki S. Gating System Design and Simulation of Gray Iron Casting to Eliminate Oxide Layers Caused by Turbulence. Int J Met 2016;11. doi:10.1007/s40962-016-0061-3.

[46] Hodder KJ, Chalaturnyk RJ. Bridging Additive Manufacturing and Sand Casting: Utilizing Foundry Sand. Addit Manuf 2019. doi:10.1016/j.addma.2019.06.008.

[47] Geng H, Li J, Xiong J, Lin X, Zhang F. Geometric Limitation and Tensile Properties of Wire and Arc Additive Manufacturing 5A06 Aluminum Alloy Parts. J Mater Eng Perform 2017;26:621–9. doi:10.1007/s11665-016-2480-y.

[48] Hackney P, Wooldridge R. Optimisation of Additive Manufactured Sand Printed Mould Material for Aluminium Castings. Procedia Manuf 2017;11:457–65. doi:10.1016/j.promfg.2017.07.136.

[49] Sama SR, Badamo T, Lynch P, Manogharan G. Novel sprue designs in metal casting via 3D sand-printing. Addit Manuf 2019;25:563–78.

doi:https://doi.org/10.1016/j.addma.2018.12.009.

Chapter 2

Towards Functionally Graded Sand Molds for Metal Casting: Engineering Thermo-Mechanical Properties using 3D Sand-Printing

This chapter is currently under-review for publication in JOM: Martinez, D., Bate, C., & Manogharan, G. (2019). Towards Functionally Graded Sand Molds for Metal Casting: Engineering Thermo-Mechanical Properties using 3D Sand Printing.

Abstract

Growing applications of additive manufacturing (AM) have now been adopted for metal-castings via indirect hybrid AM, i.e., 3D Sand-Printing (3DSP). A comprehensive study on thermo-physical properties of 3DSP molds and its effects on aluminum castings is presented in this chapter. The effect of furan binder content (i.e. 1-3%) is evaluated for as-printed 3DSP molds to determine changes in: dimensional accuracy, density (helium pycnometry), actual binder content (Loss on Ignition) and mechanical strength (3-point bending and tensile testing) and thermal properties (Transient plane source technique and casting runs). Pore network characterization via mercury intrusion porosimetry does not reveal any significant differences in the morphology of pore structures due to varying binder concentration. However, bulk permeability is reduced with increasing binder content. Thermal analysis shows a reduction in conductivity and heat capacity due to binder degradation. Findings from this study will enable the optimum selection of binder content for functional grading of 3DSP molds/cores for adequate degassing and mechanical strength which is ready for adoption by both foundries and 3DSP service providers.

2.1 Introduction and Background

As automotive, energy and aviation industries continue to increase demand for high-performance aluminum production parts, the market for aluminum castings is expected to increase at a compounded annual growth rate (CARG) of 9.1% to USD 86.5 billion by the year 2025 [1]. As this demand for high-quality castings continues to grow, additive manufacturing (AM) via 3D Sand-Printing (3DSP, a - binder jetting AM technique) has been proven to offer a novel approach to tooling-less manufacturing [2,3] of complex castings [4,5] with increased mechanical properties [6,7] and lower lead times [2,8]. 3DSP offers both technological and economic advantages to the aluminum casting industry when compared to traditional sand-casting. Another advantage of 3DSP is the large array of alloys qualified for sand-casting when compared to direct metal AM processes such as laser-powder bed fusion and directed energy deposition [9]. The basic principle of 3DSP is selective deposition of an acid catalyst mix (e.g., furan) on a layer of silica (e.g., foundry sand) based on layer-by-layer CAD information until the final mold/core is printed. Once molds are completely 3D-sand printed, they are de-powdered and assembled for pouring similar to traditional sand casting. Similar to most other AM processes, unbound material (i.e., foundry sand) is retrieved, sieved and reused in subsequent 3DSP builds.

Advancements in 3DSP have led to the development of "Rapid Casting Technology" [10–12], where the process part of designing final casting to pouring can be compressed using digital design, simulation, and printing. In order to achieve seamless integration and adoption of 3DSP in traditional foundry operations, it is critical to understand the mechanical and thermal characteristics of 3DSP molds and cores. These critical characteristics have been the focus of several studies ranging from mechanical strength and dimensional accuracy [10,13,14] to porosity and permeability [13,15]. However, there is a lack of fundamental knowledge on the effects of thermo-mechanical properties of 3DSP molds based on printing conditions and resulting materials

properties of resulting metal castings. This original research is intended to present a comprehensive examination of 3DSP mold characteristics, including thermo-mechanical properties of both sand molds and final aluminum castings under the varying influence of a critical 3DSP parameters - binder saturation, i.e., binder content.

The final objective in this research is to leverage the capabilities of layer-by-layer controlled deposition of sand and binder in a 3DSP system to simultaneously control local distribution of mechanical strength (i.e., handling strength), thermal diffusivity (i.e., solidification rate) and gas permeability (i.e., outgassing) within different sections of the sand molds. This study also aims to demonstrate the unique opportunities to engineer both the mold and casting properties that are not otherwise feasible via traditional molding methods. For instance, binder content can be functionally graded across the volume of molds and cores such that higher mechanical strength is achieved near the mold walls and higher permeability via networked pores is incorporated for outgassing of mold gas away from the mold walls. This study presents a systematic framework to study the influence of binder saturation on thermal properties and porosity. In addition, it aims to provide insights into the correlation between sand-binder content relationship to achieve adequate mold strength, printing accuracy and casting characteristics. To the best of the authors' knowledge, this study is the first reported comprehensive study that reports on the unexplored process map to achieve functionally graded 3DSP sand-molds to enable production of high-performance casting.

In traditional sand molds, mold composition has been modified to obtain different characteristics in the final metal casting [16–18]. The capabilities of 3DSP have been explored by redesigning the mold to accommodate novel insulation capabilities [19–21]. Hackney and Wooldridge [22] focused on characterizing an ExOne S-Max system for changes in dimensional accuracy, density, tensile, compressive, and impact strength using manufacturer-recommended settings. Mitra et al. [13] analyzed the effect of aging, i.e., mold curing temperature and time on flexural strength (3-point bending) and permeability in a similar study using ExOne S-Print

machine. Mechanical strength and permeability were observed to remain approximately constant over time at curing temperatures of 100 °C or less. More recently, they reported that binder saturation has a drastic effect on flexural strength and no significant change is observed in permeability when curing occurs at room temperature [23]. However, the possibility of altering intrinsic mold properties, such as permeability, heat capacity and conductivity, along with varying mechanical properties by modifying printing parameters remains largely unexplored. Binder saturation simultaneously influences multiple mold properties such as dimensional accuracy and density. Therefore, a process map that establishes this complex interaction of mold properties is required to obtain optimum mold and casting results. To the best of the author's knowledge, there has been no prior reported study that establishes this critical process map for varying 3DSP process conditions (e.g., binder saturation).

2.2 Materials and Methodology

3DSP samples were fabricated in a Viridis3D RAM sand printer (Enviosiontec, Woburn, MA) using silica sand of grain fineness number (GFN) 65 round or subangular with a dry premixed acid catalyst and furan binder. Six different binder deposition settings were selected to vary binder content between 1% and 3%. In this study, the levels are labelled as $B_{1.5}$, $B_{2,}$ $B_{2.5,}$ $B_{3,}$ B_4 and B_5 which refers to the number of printer-head activation pulses per second as set by the manufacturer's convention. Specifications of the samples are presented in Table 2-1. Samples of the same binder content were printed in a single build box.

The large cylinders, pouring cups and 3PB specimens were used to measure dimensional tolerance using a digital caliper. The diameter was measured multiple times (n=4) at the midline section in two orthogonal directions, and results were averaged to report the overall diameter along

with cylinder height. Loss on Ignition (LOI) testing was conducted as per AFS Standard 5100-00-S [24] using the 20Ø x 20mm samples (12g) for consistency across all binder conditions. Humidity content was determined by recording mass of the samples before and after heating in an oven for 150 minutes at 107°C. Samples were weighed at 0, 90 and 150 minutes. Lack of change in sample weight between measurements showed that water content was completely evaporated. Subsequently, burn-out of binder content was performed by heating the samples 986 °C. Furan resin degrades at 180°C [22] and ignites at 595°C [25]. Samples were weighed at 60, 120 and 180 minutes. Lack of change in sample weight between measurements proved that all binder had been burned out from the samples. The amount of binder in the samples was quantified based on the difference in weight of the samples after 180 minutes at 986°C and 190 minutes at 107°C.

Table 2-1. 3D sand printed samples - Design of Experiments

Sample	Dimensions (mm)	Test	Number of Tests per Condition (n)
Pour Cup	130 x 130 x 105	Experimental Solidification Time Heat Diffusivity	1
Large Cylinder	100Ø x 50	Transient Heat Plane Source	1
MIP Cylinder	7Ø x 20	Mercury Intrusion Porosimetry (MIP)	1
LOI Cylinder	20Ø x 20	LOI Helium Pycnometry	2 3
Permeability	50.8Ø x 50.8	AFS Permeability	9
Flexural Sample	15 x 15 x 150	3 Point Bending	8
Tensile Coupon	44 x 76 x 25	AFS Tensile	9

In order to characterize pore network properties, mercury intrusion porosimetry (MIP) was employed since MIP is a well-established technique used in petroleum industry [26–28],

construction engineering [29–31], and pharmacy [32–34] to identify pore sizes ranging from 3nm to 360nm diameters [35].

A common experimental approach to determine thermal properties in molding materials is the one-dimensional steady heat flux set-up [36,37]. Other techniques for determining thermal properties include the laser flash technique and inverse-heat method. The former requires a smooth and polished sample such that laser reflection can be measured. However, it is not a feasible technique for rough surfaces of sand molds [38]. The latter inverse-heat method involves reproducing measured temperatures in a casting experiment via numerical modeling by back-calculating unknown thermal variables [39,40].

Using the one-dimensional analytical representation of the system, a diffusion equation can be developed with known boundary temperatures [41], i.e., recorded temperatures at known locations within the mold using thermocouples. The diffusion equation can be expressed based on an error function as follows:

$$\frac{T_{x,t}-T_s}{T_{air}-T_s} = \mathrm{erf}\left(\frac{x}{2\sqrt{h_d \cdot t}}\right) \tag{2-1}$$

where thermal diffusivity h_d $(\frac{m^2}{s})$ of the mold material is calculated knowing the temperature $T_{x,t}$ (K) at a given point x (m) in the mold. T_s and T_{air} represent the temperatures (K) at the inner surface of the mold which is in contact with metal and ambient temperature respectively.

Another method to measure thermal properties is the transient plane source (TPS) or “hot disk” technique. Thermal properties of solid material can be back-calculated by measuring the increase in temperature of a double spiral Wheatstone bridge. The temperature of a heated sensor through electric current [42] is used in the conduction equation of a hot disk within an infinitely large sample to back-calculate the thermal conductivity and diffusivity of the sample. The tested

material must be large enough and the temperature sampling time should be short enough to prevent the boundary conditions to influence the experiment [43]. It is also important to have uniform flat surface contact between the sensor and sample. TPS has been demonstrated has an effective technique to measure a wide range of thermal conductivities with an accuracy of ±5% [44].

Subsequently, these results can be employed in Chvorinov's law to determine mold constant and thermal properties of 3DSP sand molds using the following equation:

$$T_s = \mathrm{B}\left(\frac{V}{A}\right)^2 \tag{2-2}$$

This analytical expression relates the solidification time T_s (s) of a casting with total volume V (m^3), surface area (m^2) and mold constant B (s/m^2) [45–47]. The mold constant is related to the thermal properties of the alloy being poured and hence, in order to isolate the impact of mold properties, a coefficient of heat accumulation bf can be defined as a function of the mold density ρ_m (kg/m^3), specific heat c_m (J/m^3K) and thermal conductivity k_m (W/mK) as shown in Eq. 2-3:

$$b_f = \sqrt{\rho_m c_m k_m} \tag{2-3}$$

Density measurements were determined using a Micrometrics AccuPyc II 1340 helium pycnometer. The technique was selected because of relative ease of execution, accurate results based on reported studies and recent application in binder jetting parts to determine skeletal density [48–50]. Gas pycnometry involves the measurement of gas volume (e.g., helium which was used in the study) required to fill a vacuum chamber with the test sample. With known gas volume for a given pressure and temperature, volume of the testing chamber and weight of the sample, skeletal

density can be determined. The accuracy of this technique depends on the assumption that most voids within the sample are interconnected between each other and with the sample surface.

2.2.1 Mechanical Properties of 3DSP Molds

3DSP samples were tested for mechanical strength via tensile and flexural experiments. Tensile specimens were tested as per AFS 3301-08-S [51] in a Simpson Analytics universal sand strength testing machine using the standard 25.4mm tensile specimen design (see Table 2-1). These samples were printed in the horizontal position with the mechanical loading axis along the recoating direction. Nine samples per binder condition were tested to minimize deviation from true mean strength [52].

Flexural tests are generally used to determine mold and core properties in both the AFS [53] and German [54] standards. 3DSP samples were tested for ultimate flexural strength using 3-point bending tests as per ASTM E290 [55] standard on samples of dimensions 15mm x 15mm x 100mm (see Table 2-1) for eight samples per bending condition. Four samples were tested with the applied force normal to print direction and four samples with the applied force along the print direction. An MTS WTest 100 machine with a 100 kN load cell was used to determine ultimate flexural strength based on the length between supports L (mm), width w (mm) and thickness t (mm) of the specimen to determine the stress curve σ_{flex} (MPa) based on recorded force F (kN) from Eq. 2-4:

$$\sigma_{flex} = \frac{3FL}{2wt^2} \tag{2-4}$$

The span length, loading rate and data acquisition rate were set to 60 mm, 2.5 mm/min and 10Hz, respectively.

2.2.2 Permeability and Mercury Porosimetry of 3DSP Molds

Permeability tests were performed in accordance to AFS 5224-13-S standards [53]. Nine cylindrical specimens per binder condition with dimensions of Ø50.8mm x 50.8mm were tested with direction of flow normal to print direction. The AFS permeability number was obtained using a Simpson Analytics Digital Absolute Permmeter using Eq.3-5, where Q is the volume of air of the permmeter pneumatic cylinder (m^3), h and A are the height (m) and cross-section (m^2) of the 3DSP sample, respectively, P is the differential pressure (Pa), and t is the time for the complete flow of air across the cylinder (s).

$$P = \frac{Q \times h}{A \times P \times t} \tag{2-5}$$

MIP tests were performed on one Ø7mm x 20mm sample for each binder condition. This technique involves measurement of volumes of liquid mercury that intrudes the sample at precisely controlled pressures [35]. The tests were performed in a Micromeritics AutoPore V system and MicroActive Software (Norcross, GA) was used for data processing. By applying the Washburn model [56], the pore structure can be analyzed as a conglomeration of cylinders of length L (m) which is progressively filled with increasing driving pressure P (Pa) using the following rule:

$$\frac{\partial l}{\partial t} = \frac{P(r^2 + 4\varepsilon r)}{8\eta L} \tag{2-6}$$

where r is the radius of the cylinder (m), ε is the friction coefficient between mercury and sand, and η is the kinematic viscosity $\left(\frac{m^2}{s}\right)$ of mercury. Subsequently, three unique quantitative measures of the porous media can be calculated: (a) pore size distribution, (b) pore surface area per gram of material, and (c) average and median pore diameter.

2.2.3 Thermal Properties of 3DSP Molds

Cooling curves of 99.9% pure aluminum were determined from pouring of 3DSP cooling cups for every binder condition (n =5) based on solidification time and thermal diffusivity measurements. The latter was back-calculated from the one-dimensional steady-state solution to thermal diffusion equation. The highest binder ratio batch (i.e., B_5) failed to consistently print the pouring coups and hence, pouring experiment could not be performed at this binder condition. Pure aluminum was selected in order to achieve a definite freezing point in the cooling curve using an open top pour cup (25mm thick walls to hold 80mm^3 of pure aluminum of about 1.4 kg. as shown in Fig. 2-1).

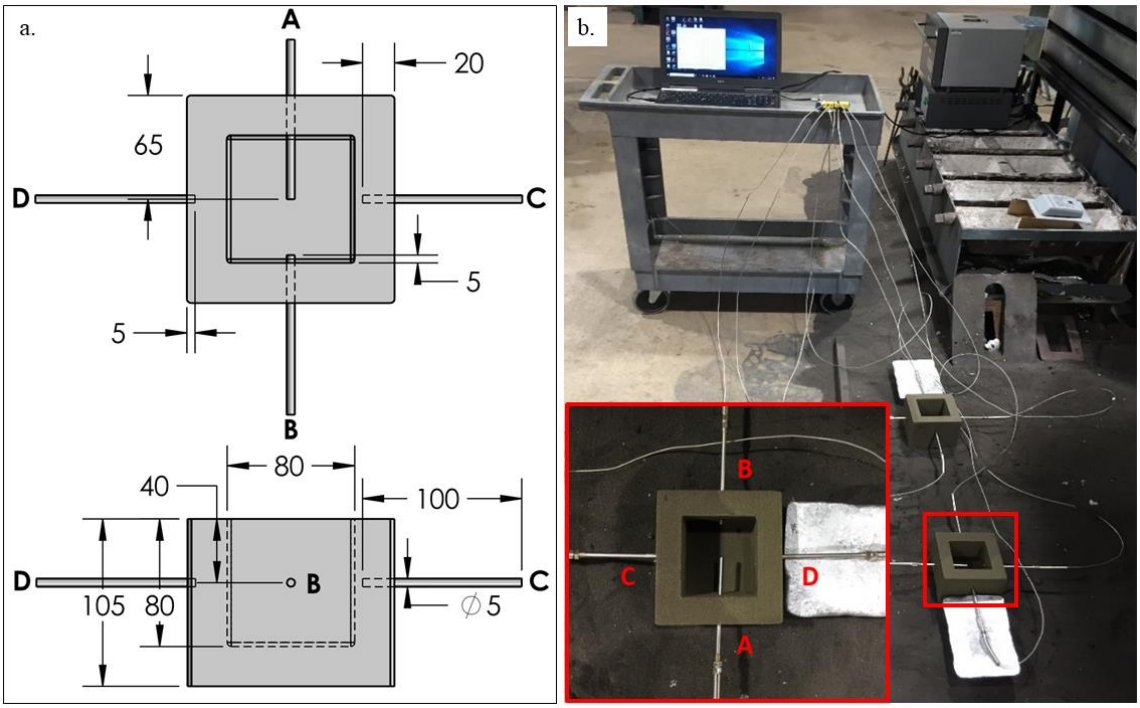

Figure 2-1. (a) 3DSP pour cup dimensions in mm and (b) experimental setup

Four TL1815 k-type thermocouples rated for maximum temperature of 800 °C with an accuracy of ± 0.1°C were used to measure the temperature at four unique location within the mold. All probes were placed at identical distance of 40mm from the top of the cup as shown in Fig. 2-1a: (A) middle of the casting volume, (B) 5 mm from the mold wall in contact with the metal, (C) 5mm from the mold wall in contact with ambient air and (D) 5mm from the ambient air within the mold wall (see Fig. 2-1b). Temperature was recorded using a data acquisition unit from National Instruments cDAQ-9171 and NI-9212 through a LabView script at a sampling rate of 10 Hz. The melt temperature prior to pouring was measured using OMEGA OS204 infrared thermometer and was found to be 765 ± 4 °C in the ladle. Data collection was prior to melt pour and continued through the liquid cooling phase, liquid-solid transition, and solid cooling to room temperature.

Results obtained via analytical one-dimensional solution to the conduction equation are compared to transient plane source (TPS) technique which was performed in a Kapton 8563 F1 hot-disk sensor (ϕ19.6mm) with an output power of 90 mW placed between two 3DSP samples. The samples were measured every 80 seconds while heating the sample to 50°C, 100°C and 250°C in order to observe variations in thermal properties (see Fig. 2-8). Five measurements were performed per binder condition at each temperature level. The samples were heated at a rate of 0.42°C per minute with a rest time of 60 minutes at each temperature level to reach steady state. This test was carried out for 4 binder levels, $B_{1.5}$, B_2, $B_{2.5}$ and B_5. Due to setup error, results for $B_{2.5}$ level were only obtained during the heating phase.

2.2.4 Mechanical Testing of Aluminum Castings

Flexural bending tests were performed as per ASTM E290 standard [55] on six aluminum samples per binder condition. The samples of dimensions 20mm x 70mm x 4.5mm were machined from center of the castings to eliminate edge effects (see Fig. 2-9). The span length, loading rate and data acquisition rate were set to 60 mm, 2.5 mm/min and 10Hz, respectively.

2.2.5 Microstructure of Aluminum Castings

Grain microstructure was evaluated from 12mm x 12mm x 6mm specimens machined from the bottom corner of the castings to include edge effects of solidification sand molds which could be correlated to thermal properties of the 3DSP molds (see Fig. 2-9). Surface nearest to the bottom surface was ground and polished down to 1µm using diamond polishing suspension. In order to observe grain structure, samples were etched for 6-8min using Keller's reagent of the following chemical composition: 95ml H_2O (water), 2.5ml HNO_3 (nitric acid), 1.5ml HCl (hydrochloric acid)

and 1ml HF (hydrofluoric acid) [57]. Images were captured with an Olympus SZH10 Research Stereo microscope with an Omax A3530U 3.2MP digital camera using Toupview software from ToupTek Photonics (Hangzhou, Zheijiang). Postprocessing and analysis were performed using open-source ImageJ.

2.3 Results and Discussion

2.3.1 Loss on Ignition of 3DSP Molds

Loss on ignition (LOI) testing reveals significant deviation from expected values provided by the equipment manufacturer, specifically at lower binder content levels (see Fig. 2-2a). Intermediate pulse levels result in binder contents that are closer to measured values, with an error near 10%. Binder conditions of $B_{2.5}$, B_3 and B_4 show comparatively small changes in binder content which was also observed in dimensional tolerances (see Fig. 2-3) and mechanical testing (see Fig. 2-4). Actual binder content ranges between 1.49% and 2.74%. Water content remains below 0.2% in all binder conditions (Fig. 2-2b). The experimental values represent the average of two LOI tests, except for B_5 level, for which only 1 result was obtained due to measurement error in one of the trials. The values of binder content as expected by the manufacturer is supposed to follow a nearly linear relation (R^2 value of 0.9696) with the number of pulses applied to the binder head.

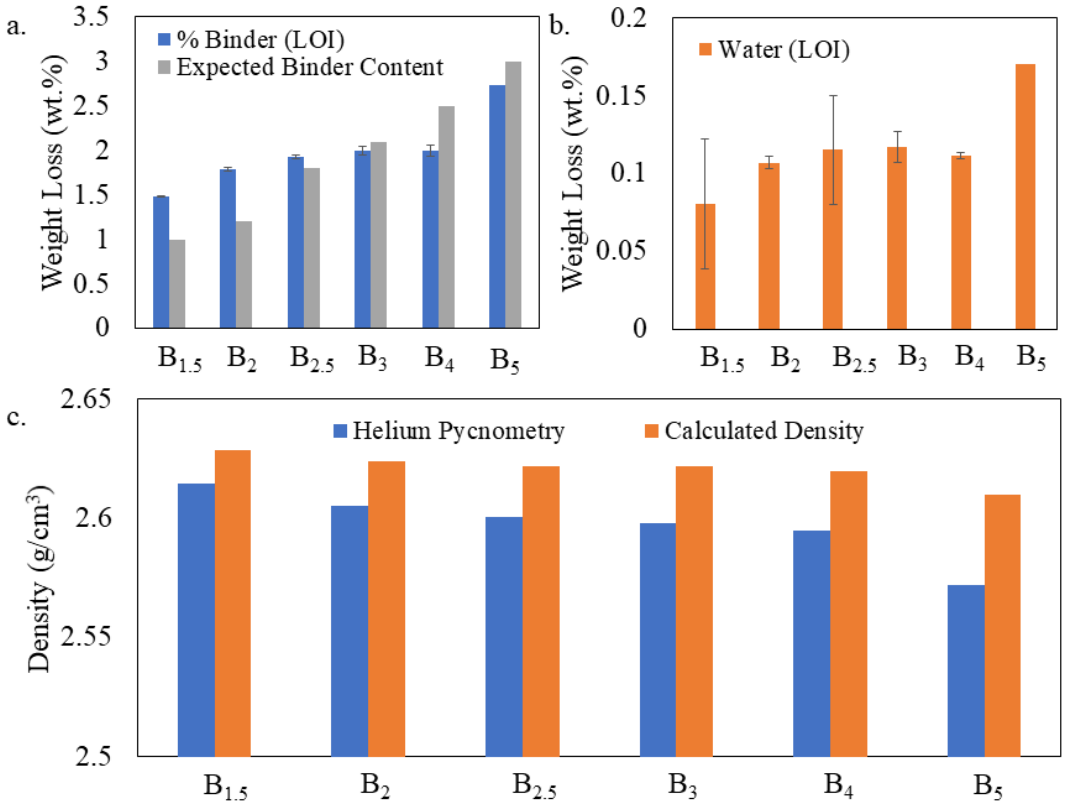

Figure 2-2. (a) Expected and actual binder contents within the samples tested via AFS Loss on Ignition test, and (b) density measurements obtained via Helium Pycnometry and calculated using a linear relation between silica sand and furan binder

Using helium pycnometry (n=3), a nearly linear reduction in density with increase in binder concentration is observed, following the expression:

$$\rho = -3.4222x + 2.6659 \tag{2-7}$$

where x is the concentration of binder in the sample (% weight) with an R^2 value of 0.9931.

This linear relationship suggests that the arrangement of silica particles in each sample is not altered due to sand-binder interactions. The density of loose sand and liquid furan binder were

determined as 2.651g/cm^3 and 1.142g/cm^3 respectively. A linear equation to predict density values as function of binder condition (% weight) can be derived:

$$\rho_{printed\ smaple} = x\rho_{sand} + y\rho_{Binder} \tag{2-8}$$

Bias towards overestimating the actual density with increase in binder content is observed when using this linear equation (see Fig. 2-2c). This could be attributed to the accumulation of acid catalysts with relatively lower weight [13] which is not considered in this study. Since binder concentration of over 3% wt. results in inconsistent print quality and higher costs [58] to print molds, this analytical approximation of mold density is considered accurate for normal printing conditions with acceptable accuracy (% Error < 1.5%).

2.3.2 Dimensional Accuracy of 3DSP Molds

The flexural bending samples, pouring cups and large cylinders are measured and analyzed for dimensional accuracy after 3DSP. These samples where measured several days after printing and hence, it is assumed that shrinkage due to binder cross-linking will have reached steady state conditions. It must be noted that the rate of shrinkage during the initial few hours after printing (when it is challenging to handle the molds) has been demonstrated to change based different binder and catalyst concentrations [59]. However, this study is not relevant to practice due to the need for higher green strength to both handle and transport 3DSP molds.

It is observed that increase in binder content reduces printing accuracy which is consistent with reported studies [60,61] and is attributed to binder bleeding, which is the phenomenon of capillary flow of binder beyond the deposited zone. The flow of binder out of the immediate droplet area will agglomerate additional sand grains which result printed parts with higher dimension when

compared to nominal dimension. Another study reports an opposite effect in binder jetting of finer materials [62].

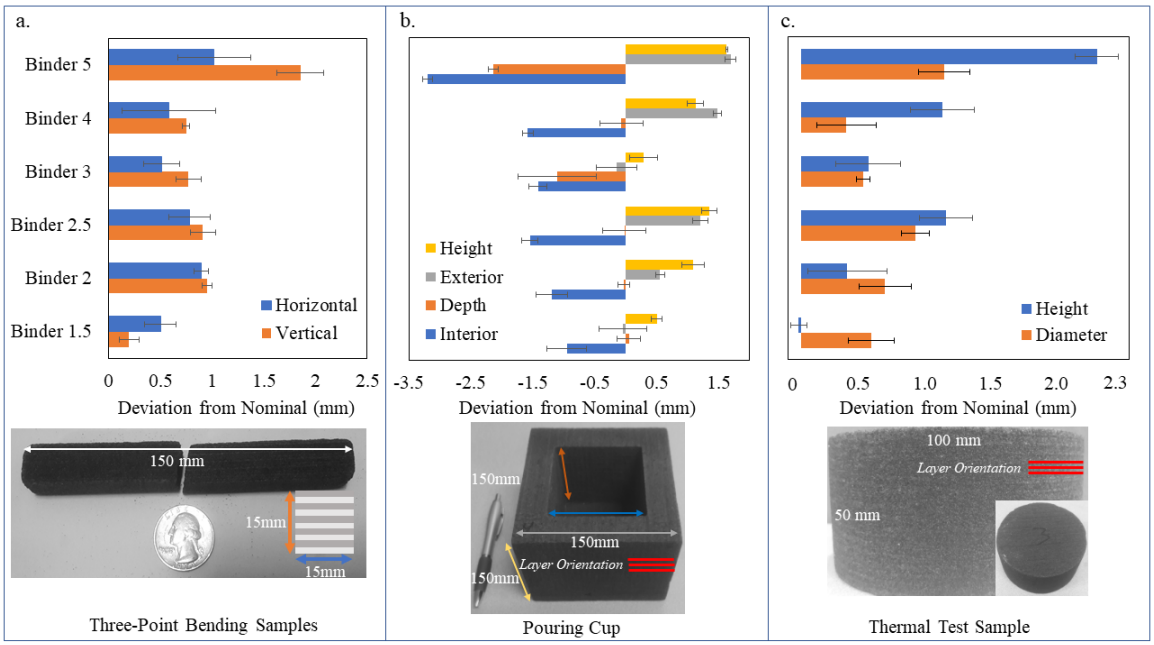

Figure 2-3. Average deviation from the nominal dimensions (in mm) along and across the printing direction for (a) flexural samples, (b) pouring cups and (c) cylinders. The print orientation is presented for every geometry condition.

The deviation from nominal dimension is smaller across the print direction in all three samples with the exception of distance between the interior walls of the pouring cup where maximum deviation from the nominal is at the highest binder concentration level (>3mm). However, this is explained by the fact that the measurement is composed of two different printed sections (i.e., binder bleeding in the two walls of the cup). However, deviation of wall thickness is similar to trends in other samples. At the lowest binder level, the deviation is around 0.5mm in

across the print direction. At the intermediate levels (i.e., B_2, $B_{2.5}$, B_3 and B_4) deviation is between 0.5 and 1mm which follow similar trend to reported LOI results.

Similarly, increase in dimensional deviation is observed with increase in binder concentration along the print direction. However, the deviation is lower across all samples when compared to measurements along the print direction which can be attributed to the compressive effect that the recoating rake has been demonstrated to exert on the printing bed [60]. This compression could be accentuating the binder bleeding in the direction perpendicular to the printing plane and further research is required to verify this hypothesis. In the case of deviation in depth of the pouring cup (see Fig. 2-3b), an opposite trend is observed which could be attributed to retrieval and cleaning of loose sands from the build box using compressed air. This final cleaning step is believed to have affected the printed depth of the cups.

2.3.3 Mold Mechanical Properties

Ultimate tensile strength 3DSP samples has a non-linear relation to binder content. Optimum strength is obtained at the $B_{2.5}$ level across build orientation (see Fig. 2-4). At the highest binder content level, tensile strength increases again. The mean strength regardless of binder content for this system is lower than reported values for tensile strength of chemically bonded sand using furan binder in a ZCorp machine [63]. This could be attributed to the coarser grain size distribution used in this study, which has been identified as an important factor that influences tensile strength [64,65]. As expected, fracture was brittle in all cases.

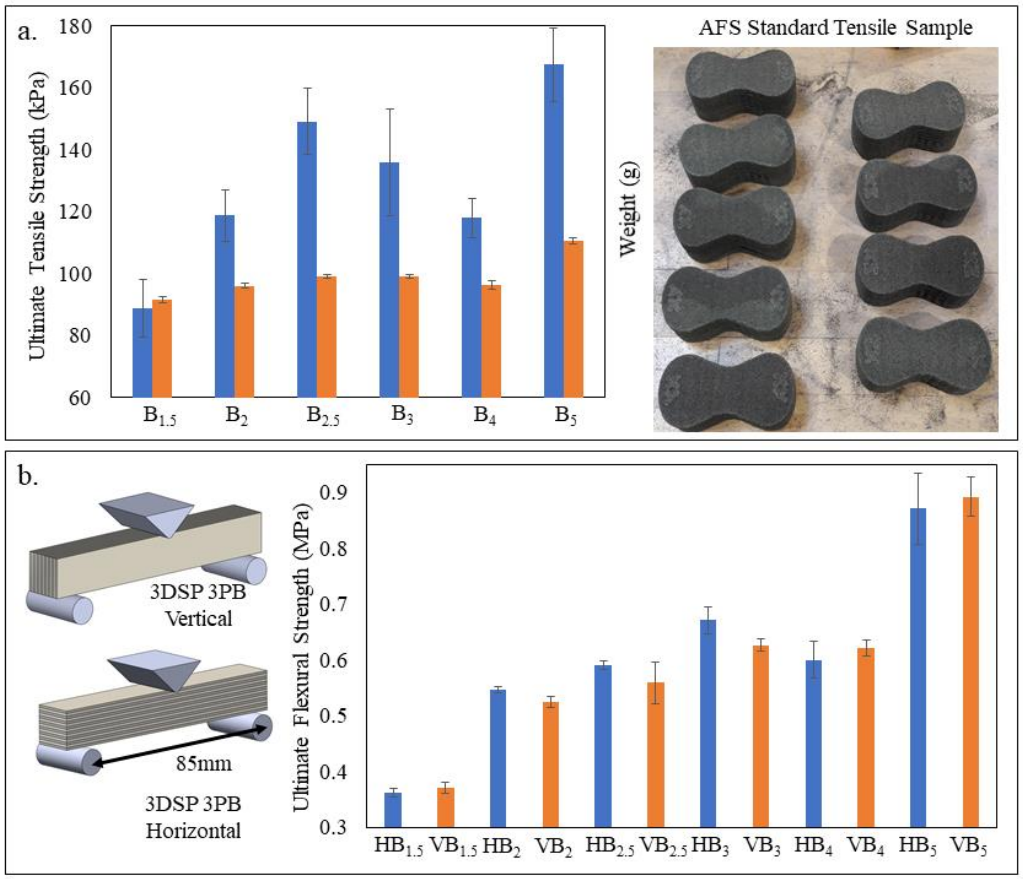

Figure 2-4. (a) Ultimate tensile strength and sample weight, and (b) ultimate flexural strength in two orientations with respect to print direction

Ultimate flexural strength shows a similar trend to that of ultimate tensile strength, with increasing strength as binder concentration reaches the B_3 level, a drop in B_4 and a final increase with the maximum binder concentration level. Flexural strengths along and across build orientations show very similar results; however, at intermediate binder levels, a lower maximum strength can be observed when the force is applied parallel to the printing plan. Ultimate flexural strengths are lower than reported values in the literature for other 3DSP systems using furan binder, which employed ExOne [13,60] and Voxeljet [14] systems. Tensile strength is also shown to be lower than flexural strength, coinciding with other reported values for 3DSP systems [14]. It must

be noted that exact comparison to other 3DSP systems is difficult since in some cases layer thickness and sand grain size are not reported. Table 2-2 presents a summary the reported values for ultimate flexural strengths in cold box, heat cured and 3DSP cases. The 3DSP system reported in this study has lower strength when compared to previously reported studies [66].

Table 2-2. Comparison of ultimate flexural strength for different binder types

System	Sand Type	Binder	UFS [MPa]	Ref.
Cold-box (phenolic urethane)	Round silica GFN 55.56	1.25 wt.% Phenolic Urethane	1.8	[67]
Cold-box (phenolic)	H32 Silica	1.2-1.9 wt.% phenolic resin	0.38*	[68]
Warm-box (furanic)	H32 Silica	Between 1.2 and 1.9 wt.% Furan resin	0.72*	[68]
Warm-box (urea-furanic)	H32 Silica	Urea-furanic resin	0.44*	[68]
Voxeljet VX 1000	-	Furan resin 1 wt.%	1.3	[14]
ExOne SPrint	Round silica, GFN 97	Furan resin 1-3 wt.%	3.2*	[13]
Viridis 3D RAM	Round silica, GFN 65	Furan resin 1-3 wt.%	0.89	This study

*These values were shown to change with curing time, maximum flexural strength at room temperature curing is reported in this table.

2.3.4 Permeability and Mercury Porosimetry

MIP results are expressed as pore volume distribution per diameter. Translating these results to pore count per diameter is difficult due to the assumption about pore geometry [69]. B_2 and B_4 samples shows pore sizes of larger median (67µm and 64µm, respectively) and mean (62µm and 59µm, respectively) based on the Washburn model (see Fig. 2-5). These samples also display broader distributions in both cumulative area and incremental intrusion. Calculations of mean pore size based on the assumption of straight cylindrical pores of circular cross-section ranges between

57µm and 62µm. No distinctive correlation can be drawn between pore size and binder content. Samples used for MIP test were destroyed at final pressure due to permanent deformation.

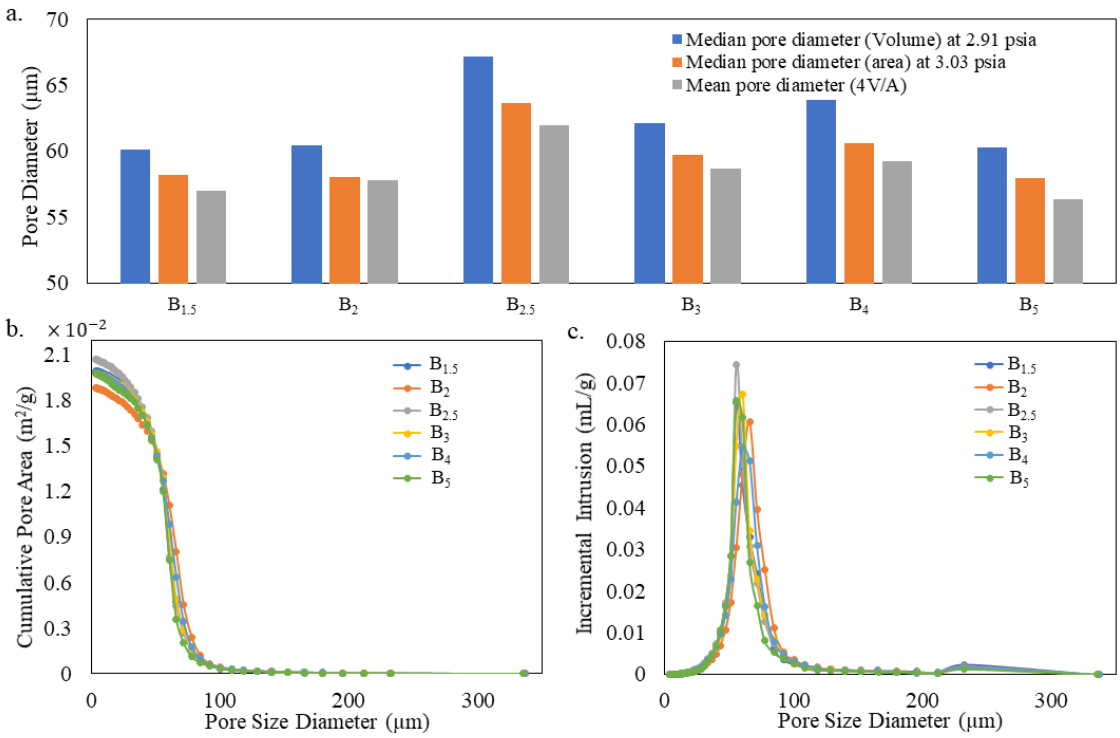

Figure 2-3. (a) Pore size, (b) pore area, and (c) incremental volume obtained via Mercury Intrusion Porosimetry (MIP)

Permeability measurements validates the hypothesis that increasing difficulty in degassing will occur during casting with increase in binder concentration (see Fig. 2-5a). This could be attributed to the reduction in pore space and/or higher tortuosity of the pore network. MIP results suggest no significant difference in pore network but does not provide detailed information on the geometric properties of the pores to understand the reduction in permeability. Future tests will

include micro computed tomography to analyze the exact geometric characteristics of the pore networks.

Fig. 2-5b shows a very nearly linear relation between mold density and permeability results, which is not seen as clearly when analyzing it as a function of binder concentration. The relation between permeability and density is direct, which might seem counterintuitive but is due to the fact that the furan binder is less dense than the silica sand, therefore as binder content increases, the total density decreases.

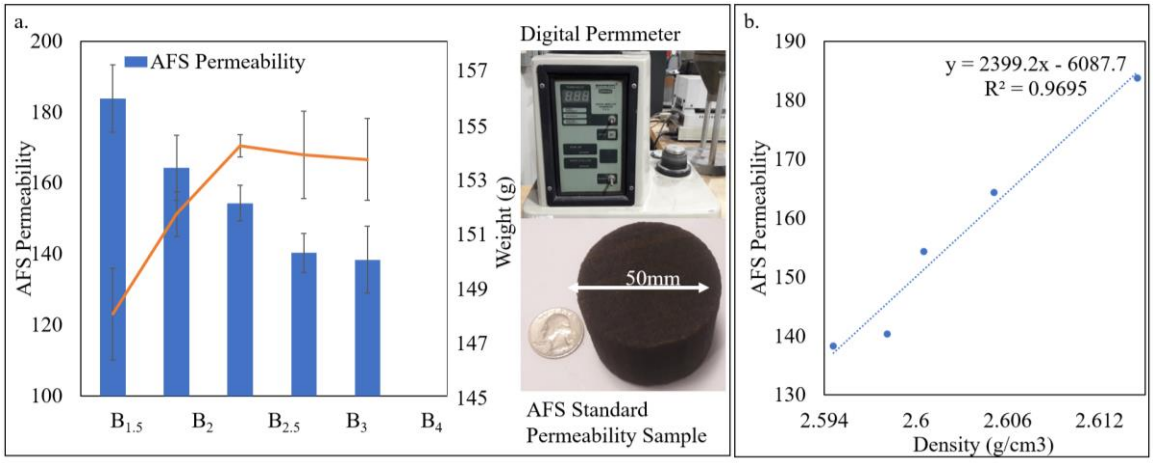

Figure 2-4. (a) AFS Permeability and weight of standard AFS samples (n=9) as a function of binder concentration and (b) mold density

2.3.5 Mold Thermal Properties

Mold and casting temperatures for each 3DSP sample were measured during and after pouring. Fig. 2-6a shows representative temperature curves at the four locations in the mold during pouring-filling-solidification. The cooling curve for location A corresponds to the thermocouple at the center of the casting which shows the characteristic horizontal line between 80s and 730s representing the transition from liquid to solid in a pure metal [70]. All binder conditions showed

a similar solidification time. The temperature in locations C and D were used to calculate thermal diffusivity across the thickness of the mold at 5mm and 20mm from the molds internal wall, using Eq. 2-1. The average thermal diffusivity calculated at these two points during solidification is shown in Fig. 2-6b. The change in heat diffusivity and corresponding heat transfer coefficient are associated with binder decomposition and water vapor transport across the mold [36,37]. Since temperatures remain below 500 °C at the locations measured within the wall, binder decomposition can be assumed to occur only within the 5mm of the wall nearest to the solidifying aluminum.

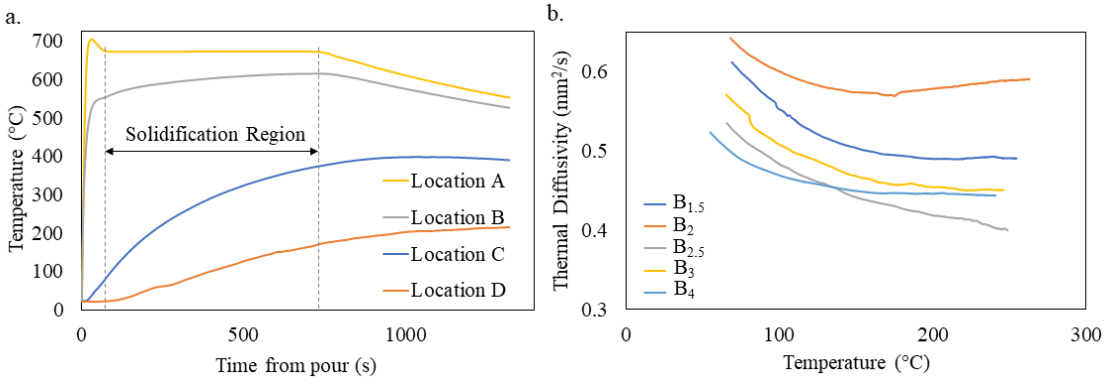

Figure 2-5. (a) A representative cooling curve for the four thermocouple positions, (b) thermal diffusivity vs. temperature is calculated using the average temperature measured at locations C and D

TPS results show a clearer effect of increased thermal diffusivity and conductivity at lower temperatures due to increase in binder content (see Fig. 2-7) which increases the heat capacity of the mold. All binder levels show a drastic reduction in thermal conductivity during the cooling cycle. The most pronounced effect is observed at the highest binder level B_5 with a reduction of 36% that is attributed to both binder degradation at 180°C and evaporation effect of humidity within the samples [25].

Similar heating cycles is reported in the literature to simulate mold aging during extended storage of molds [13]. These results suggest that heat capacity and conductivity will be significantly reduced due to mold aging and additional experimentation is required to confirm this effect. Thermal diffusivity is found to be in the same order of magnitude based on both casting and TPS runs.

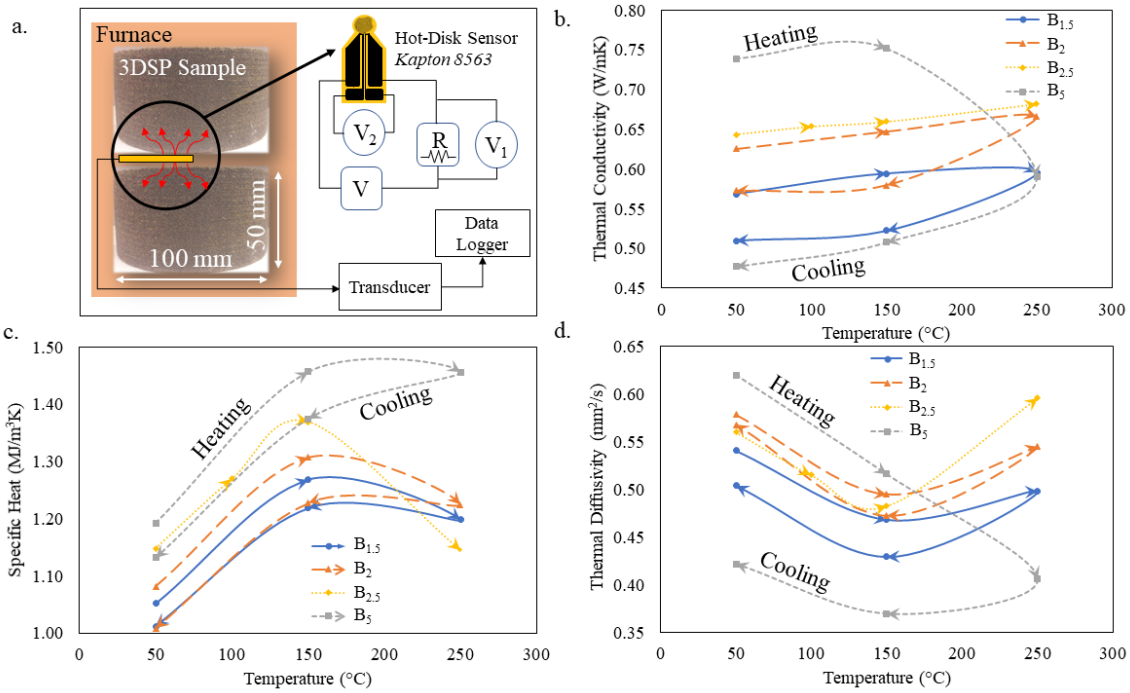

Figure 2-6. (a) Experimental setup for transient plane source (TPS) technique, (b) thermal conductivity, (c) specific heat and (d) thermal diffusivity for varying binder contents

2.3.6 Mechanical Testing of Aluminum Castings

Mechanical testing of castings was performed via 3-point bending tests on six samples at each binder level. Maximum flexural stress is reported since none of the samples suffered fracture

at peak stress (see Fig. 2-9). An ANOVA test was performed, showing statistically significant differences between the binder levels. Subsequently, a Fisher least significant difference test (LSD) was performed, which is a pairwise t-test used to determine differences between pairs of samples compared against each other [71]. The lowest binder levels, $B_{1.5}$ and B_2 show highest mean strength.

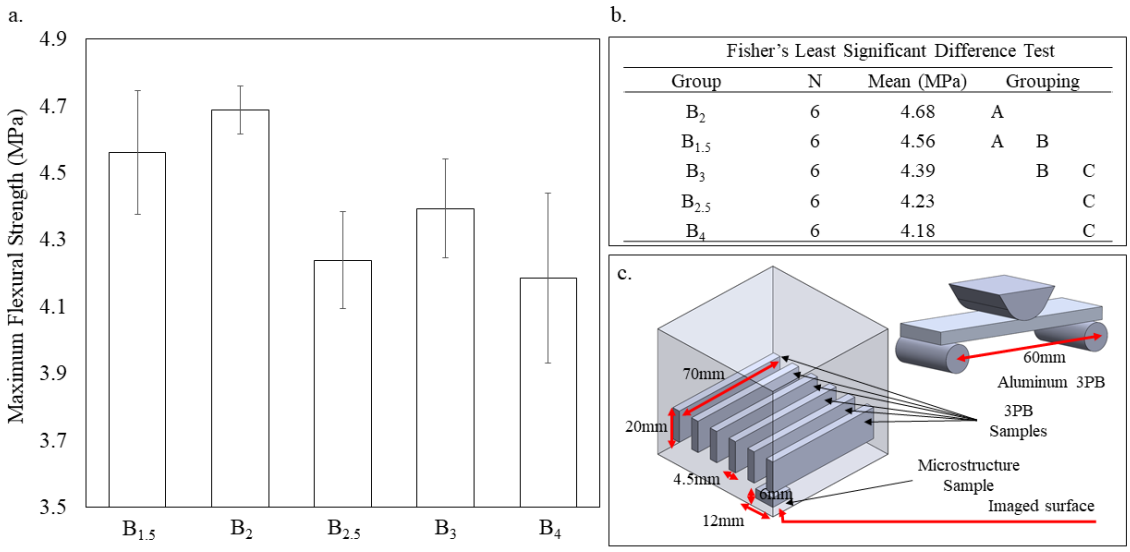

Figure 2-7. (a) Mean maximum flexural stress, (b) Fisher pairwise comparison of groups with significantly different means with 95% confidence, (c) location of extracted samples within the casting and 3-point bending

In order to differentiate between the direct effect of binder on maximum flexural strength of the casting from that of mold density, Fig. 2-9 shows the casting strength as a function of this mold parameter. Two notable regions can be observed, where lower density molds have a negative effect on mechanical strength.

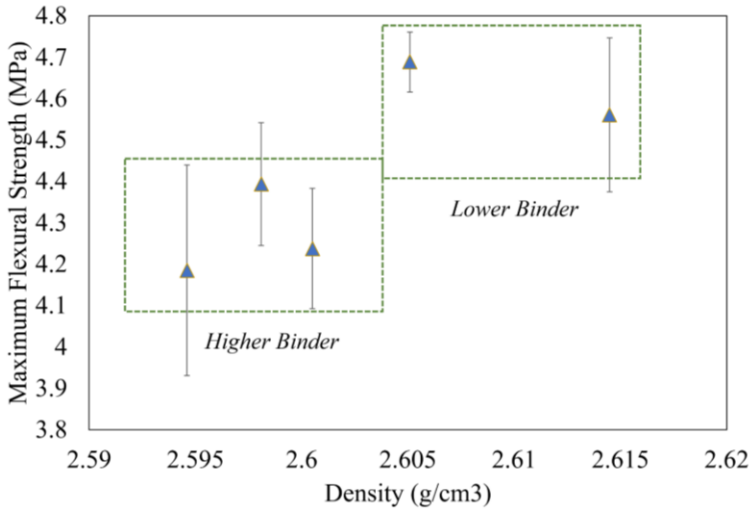

Figure 2-8. Casting maximum flexural strength as a function of mold density

2.3.7 Grain Structure of Aluminum Castings

Grain structure observed in cast aluminum samples (see Fig. 2-10) are counted via visual inspection and percentage area of casting defects (inclusions and pores) are determined using ImageJ. The larger differences in grain number and size across each face reveals that the analyzed surface area is insufficient to represent the castings as a whole and therefore, no conclusions on microstructural differences are drawn. Grain morphology is expected to be columnar near the mold surface [72]; however, only cross-sectional images are visible. The types of defects observed are dispersed micro porosity, gas pores, and possible bifilm defects. This last defect is identifiable as irregular pores with visible cracks with entrapped air (see Fig. 2-10c) [73]. The defects are common to samples across binder content levels.

a.

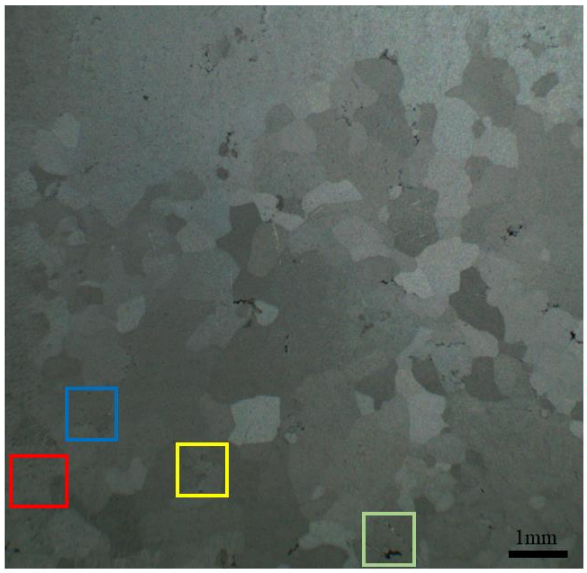

b.

Groups	Number of grains	% Area of Cracks/Film Defects
$B_{1.5}$	61	0.052
B_2	80	0.04
$B_{2.5}$	70	0.041
B_3	144	0.055
B_4	16	0.037

c.

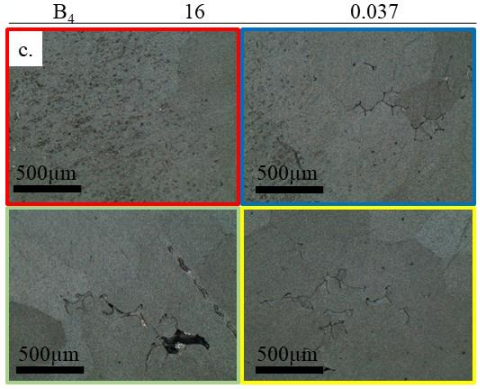

Figure 2-9. (a) Representative micrograph of etched casting, (b) grain morphology, and (c) typical casting defects including micro porosity and solidification shrinkage

2.4 Discussion

Analysis of density measurements obtained via helium pycnomentry and thermal properties obtained using the TPS technique, enables analytical calculation of heat accumulation coefficient b_f (see Fig. 2-11) based on Eq.2-3 for 3DSP printed molds of varying binder content. Thermal data obtained at 50°C is used in this calculation since density measurements are obtained at room temperature conditions. The value of b_f at higher temperatures could be lower due to binder degradation and loss of humidity which could lead to reduced density.

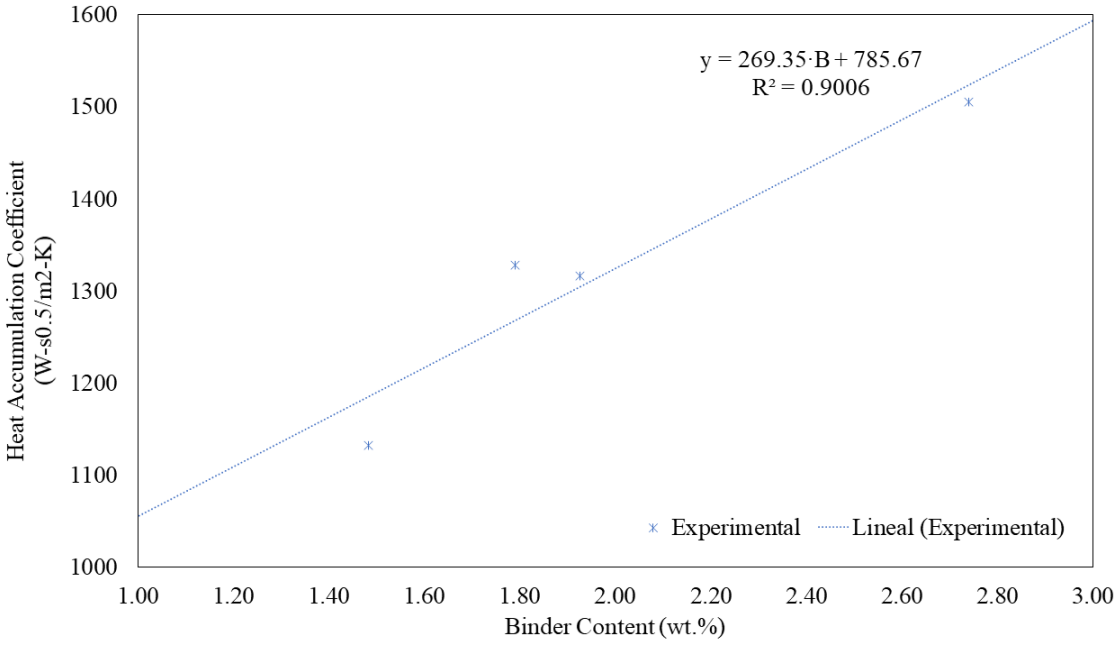

Figure 2-10. Heat accumulation coefficient (b_f) for $B_{1.5}$, B_2, $B_{2.5}$ and B_5 3DSP samples for different binder content. The B value in the lineal tendency line is the binder content in wt.%

Heat accumulation coefficient determined from this study lies within the range of typical rammed sand molds when compared to the comprehensive report by Jelinek and Elbel [45]. It should be noted that our present study is the first to report the wider chilling effect that can be achieved by modifying binder deposition during printing. Future work will address the temperature effects on mold density and subsequently on heat accumulation coefficient.

This study aimed to quantify the thermal, mechanical and permeability properties of 3D printed sand molds due to varying binder content in3DSP. This represents an initial stage in a novel approach towards creating functionally graded sand molds by applying Design for AM (DfAM) approaches. Such a framework to leverage 3DSP through this novel approach is proposed in Fig. 2-12. Findings on thermos-mechanical properties of 3DSP properties from this study and future efforts serve as inputs for design-simulation-optimization-3DSP-casting framework.

This unique approach will enable production of 3DSP molds with optimized mechanical strength, point-by-point control of permeability across the mold and venting designs. In addition, it can be extended to accurately simulate filling and solidification that will lead superior design of sand molds (e.g., ingate location and number, runner profiles, riser volumes, etc.) and/or create directional solidification within the casting.

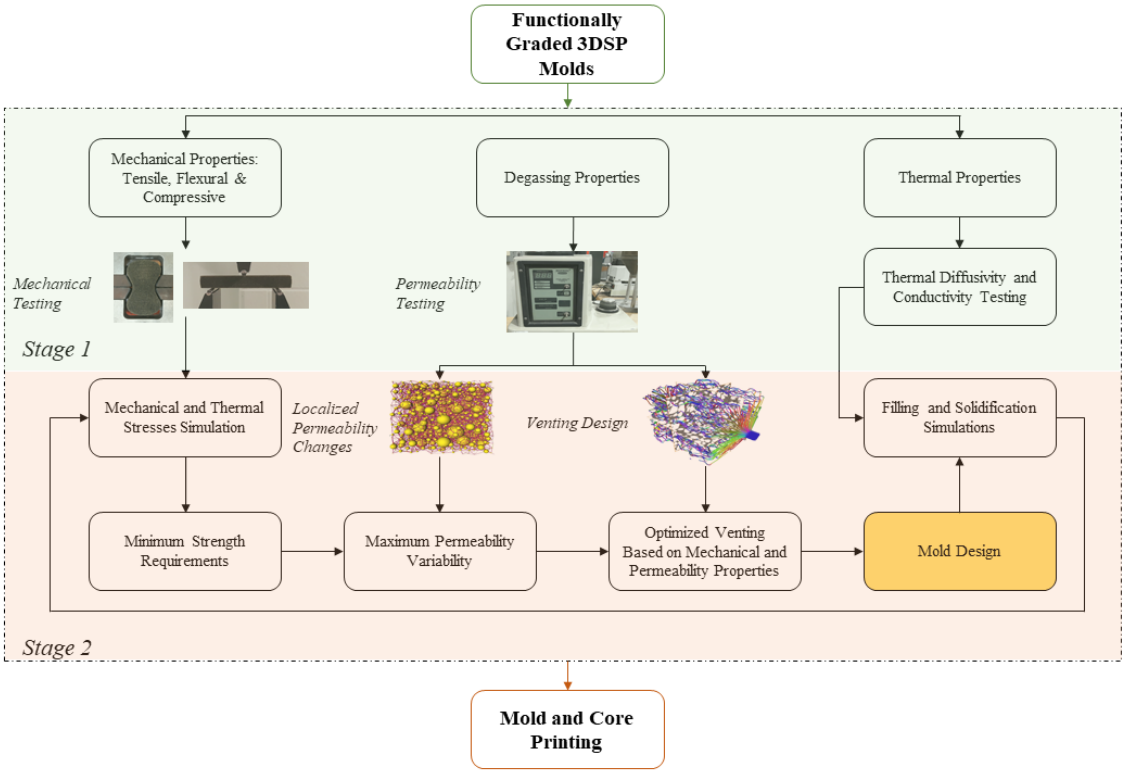

Figure 2-11. Proposed framework for functionally graded 3DSP mold to control thermal, mechanical and degassing properties of sand molds

2.5 Conclusions

In summary, this study reports on comprehensive experimental testing of 3DSP samples at 6 different binder concentrations ranging from 1.49% to 2.76% which rendered the following results:

- Variation in mechanical strength of 3DSP molds ranges between 25% and 50% based on actual binder content when compared to expected values presented by the manufacturer. Actual binder content was lower than expected value due to higher concentration at lower three pulse values and lower concentration at higher three pulse values.

- Increasing binder content had a negative effect on part tolerance.

- Tensile strength increased with binder content up to a binder content of wt.% 1.95. At the highest binder concertation, 2.76% (i.e., B_5) the maximum tensile strength was observed. Flexural strength followed a similar trend.

- Permeability decreased with higher binder content. The pore mean size is experimentally determined to range between 56µm and 62µm, calculated using mercury intrusion porosimetry.

- Density decreased with higher binder content, ±-1% from the median value of 2.600 g/cm^3based on helium pycnometry. This suggests that reordering of sand grains does not occur as binder content changes, and therefore, density can be predicted accurately by knowing the binder content in the mold.

- Thermal conductivity, diffusivity and heat capacity increases with increasing binder content at room temperature. Binder degradation affects thermal properties, particularly, at higher binder levels.

- A solidification analysis of 99.9% pure aluminum showed that binder content had no significant effect on casting solidification time. Grain morphology was shown to be similar in all

cases. A slight increase in flexural strength of the aluminum casting was observed at lower binder levels.

Acknowledgments

Authors would like to thank Dr. Robert Voigt for his expert advice, and Chris Anderson and Travis Richner for helping with casting trials. This work was partially funded by a PA Manufacturing Fellows Grant from PA Department of Community & Economic Development.

References

[1] Grand View Research. Aluminum Casting Market Worth $86.5 Billion by 2025 n.d. https://www.grandviewresearch.com/press-release/global-aluminum-casting-market (accessed May 21, 2019).

[2] Almaghariz ES, Conner BP, Lenner L, Gullapalli R, Manogharan GP, Lamoncha B, et al. Quantifying the Role of Part Design Complexity in Using 3D Sand Printing for Molds and Cores. Int J Met 2016;10:240–52. doi:10.1007/s40962-016-0027-5.

[3] Strong D, Sirichakwal I, Manogharan GP, Wakefield T. Current state and potential of additive - hybrid manufacturing for metal parts. Rapid Prototyp J 2017;23:577–88. doi:https://doi.org/10.1108/RPJ-04-2016-0065.

[4] Almaghariz ES. Determining When to Use 3D Sand Printing : Quantifying the Role of Complexity, MSc Thesis, Youngstown State University, 2015.

[5] Wang J, Sama SR, Manogharan G. Re-Thinking Design Methodology for Castings: 3D Sand-Printing and Topology Optimization. Int J Met 2019;13:2–17. doi:10.1007/s40962-018-0229-0.

[6] Sama SR, Wang J, Manogharan G. Non-conventional mold design for metal casting using 3D sand-printing. J Manuf Process 2018;34:765–75. doi:https://doi.org/10.1016/j.jmapro.2018.03.049.

[7] Sama SR, Badamo T, Lynch P, Manogharan G. Novel sprue designs in metal casting via 3D sand-printing. Addit Manuf 2019;25:563–78. doi:10.1016/J.ADDMA.2018.12.009.

[8] Weller C, Kleer R, Piller FT. Economic implications of 3D printing: Market structure models in light of additive manufacturing revisited. Int J Prod Econ 2015;164:43–56. doi:10.1016/j.ijpe.2015.02.020.

[9] Snelling D, Li Q, Meisel N, Williams CB, Batra RC, Druschitz AP. Lightweight Metal Cellular Structures Fabricated via 3D Printing of Sand Cast Molds. Adv Eng Mater 2015;17:923–32. doi:10.1002/adem.201400524.

[10] Hackney P, Wooldridge R. Optimisation of Additive Manufactured Sand Printed Mould Material for Aluminium Castings. Procedia Manuf 2017;11:457–65. doi:10.1016/j.promfg.2017.07.136.

[11] Rooks B. Rapid tooling for casting prototypes. Assem Autom 2002;22:40–5. doi:10.1108/01445150210416664.

[12] Bernard A, Delplace J-C, Perry N, Gabriel S. Integration of CAD and rapid manufacturing for sand casting optimisation. Rapid Prototyp J - RAPID Prototyp J 2012;9. doi:10.1108/13552540310502220.

[13] Mitra S, Rodríguez de Castro A, El Mansori M. The effect of ageing process on three-point bending strength and permeability of 3D printed sand molds. Int J Adv Manuf Technol 2018;97:1241–51. doi:10.1007/s00170-018-2024-8.

[14] Nyembwe K, Mashila M, van Tonder PJM, de Beer DJ, Gonya E. Physical Properties of Sand Parts Produced Using a Voxeljet Vx1000 Three- Dimensional Printer. South African J Ind Eng 2016;27:136–42. doi:10.7166/27-3-1661.

[15] Sivarupan T, El Mansori M, Daly K, Mavrogordato MN, Pierron F. Characterisation of 3D printed sand moulds using micro-focus X-ray computed tomography. Rapid Prototyp J 2019;25:404–16. doi:10.1108/RPJ-04-2018-0091.

[16] Adedayo AV. Effects of addition of iron (Fe) filings to green moulding sand on the microstructure of grey cast iron. J Brazilian Soc Mech Sci Eng 2010;32:171–5.

[17] Adedayo A V, Aremo B, Si P. Influence of Mould Heat Storage Capacity on Properties of Grey Iron. J Miner Mater Charact Eng 2011;10:387–96.

[18] Saikaew C, Wiengwiset S. Optimization of molding sand composition for quality improvement of iron castings. Appl Clay Sci 2012;67–68:26–31. doi:https://doi.org/10.1016/j.clay.2012.07.005.

[19] Deng C, Kang J, Shangguan H, Huang T, Zhang X, Hu Y, Huang T. Insulation effect of air cavity in sand mold using 3D printing technology. China Foundry 2018;15:37–43. doi:10.1007/s41230-018-7243-y.

[20] Deng C, Kang J, Shangguan H, Hu Y, Huang T, Liu Z. Effects of hollow structures in sand mold manufactured using 3D printing technology. J Mater Process Technol 2018;255:516–23. doi:10.1016/j.jmatprotec.2017.12.031.

[21] Shangguan H, Kang J, Deng C, Yi J, Hu Y, Huang T. 3D-printed rib-enforced shell sand mold for aluminum castings. Int J Adv Manuf Technol 2018;96:2175–82. doi:10.1007/s00170-018-1783-6.

[22] Hackney PM, Wooldridge R. Characterisation of direct 3D sand printing process for the production of sand cast mould tools. Rapid Prototyp J 2017;23:7–15. doi:10.1108/RPJ-08-2014-0101.

[23] Mitra S, Rodríguez de Castro A, El Mansori M. On the rapid manufacturing process of functional 3D printed sand molds. J Manuf Process 2019;42:202–12. doi:10.1016/J.JMAPRO.2019.04.034.

[24] AFS 5100-00-S. Schaumburg: n.d.

[25] Gardziella A, Pilato L, Knop A. Phenolic Resins - Chemistry, Applications, Standardization, Safety and Ecology. 2nd ed. Springer - Verlag Berlin Heidelberg; 2000. doi:10.1007/978-3-662-04101-7.

[26] Chatzis I, Dullien FAL. The Modelling of Mercury Porosimetry and the Relative Permeability of Mercury in Sandstones Using Percolation Theory. Int Chem Eng 1985;25:47–66.

[27] Yuan HH, Swanson BF. Resolving Pore-Space Characteristics by Rate-Controlled Porosimetry. SPE Form Eval 1989;4:17–24. doi:10.2118/14892-PA.

[28] Labani MM, Rezaee R, Saeedi A, Hinai A. Evaluation of pore size spectrum of gas shale reservoirs using low pressure nitrogen adsorption, gas expansion and mercury porosimetry: A case study from the Perth and Canning Basins, Western Australia. J Pet Sci Eng 2013;112:7–16. doi:https://doi.org/10.1016/j.petrol.2013.11.022.

[29] Cook RA, Hover KC. Mercury porosimetry of hardened cement pastes. Cem Concr Res 1999;29:933–43. doi:https://doi.org/10.1016/S0008-8846(99)00083-6.

[30] Abell AB, Willis KL, Lange DA. Mercury Intrusion Porosimetry and Image Analysis of Cement-Based Materials. J Colloid Interface Sci 1999;211:39–44. doi:https://doi.org/10.1006/jcis.1998.5986.

[31] Gallé C. Effect of drying on cement-based materials pore structure as identified by mercury intrusion porosimetry: A comparative study between oven-, vacuum-, and freeze-drying. Cem Concr Res 2001;31:1467–77. doi:https://doi.org/10.1016/S0008-8846(01)00594-4.

[32] Selkirk AB, Ganderton D. An investigation of the pore structure of tablets of sucrose and lactose by mercury porosimetry. J Pharm Pharmacol 1970;22:79S-85S. doi:10.1111/j.2042-7158.1970.tb08584.x.

[33] Carli F, Motta A. Particle Size and Surface Area Distributions of Pharmaceutical Powders by Microcomputerized Mercury Porosimetry. J Pharm Sci 1984;73:197–203. doi:https://doi.org/10.1002/jps.2600730213.

[34] Juppo AM. Porosity parameters of lactose, glucose and mannitol tablets obtained by mercury porosimetry. Int J Pharm 1996;129:1–12. doi:https://doi.org/10.1016/0378-5173(95)04201-6.

[35] Webb PA. An Introduction To The Physical Characterization of Materials by Mercury Intrusion Porosimetry with Emphasis On Reduction And Presentation of Experimental Data Paul A . Webb Norcross , Georgia. vol. 22. 2001. doi:10.1177/004057368303900411.

[36] Krajewski PK, Suchy JS, Piwowarski G, Krajewski WK. High temperature thermal properties of bentonite foundry sand. Arch Foundry Eng 2015;15:47–50. doi:10.1515/afe-2015-0036.

[37] Krajewski PK, Piwowarski G, Suchy JS. Thermal Conductivity of the Green-Sand Mould Poured with Copper. Arch Foundry Eng 2014;14:67–70.

[38] Xu Y, Chung D. Effect of Sand Addition on the Specific Heat and Thermal Conductivity of Cement. Cem Concr Res 2000;30:59–61. doi:10.1016/S0008-8846(99)00206-9.

[39] Williams TJ. Determination of effective riser sleeve thermophysical properties for simulation and analysis of riser sleeve performance Recommended Citation. University of Iowa, 2016.

[40] Williams TJ, Hardin RA, Beckermann C. Thermophysical Properties for ASK Chemical and Exochem Riser Sleeves for Steel Castings. Proc. 68th SFSA Tech. Oper. Conf., Chicago, IL: Steel Founders' Society of America; 2014, p. 23.

[41] Sun M-T, Chang C-H. The Error Analysis of a Steady-State Thermal Conductivity Measurement Method With Single Constant Temperature Region. J Heat Transf Asme - J HEAT Transf 2007;129. doi:10.1115/1.2739585.

[42] Coquard R, Coment E, Flasquin G, Baillis D. Analysis of the hot-disk technique applied to low-density insulating materials. Int J Therm Sci 2013;65:242–53. doi:https://doi.org/10.1016/j.ijthermalsci.2012.10.008.

[43] Gustafsson SE. Transient plane source techniques for thermal conductivity and thermal diffusivity measurements of solid materials. Rev Sci Instrum 1991;62:797–804. doi:10.1063/1.1142087.

[44] Log T, Gustafsson SE. Transient plane source (TPS) technique for measuring thermal transport properties of building materials. Fire Mater 1995;19:43–9. doi:10.1002/fam.810190107.

[45] Jelinek P, Elbel T. Chvorinov's rule and determination of coefficient of heat accumulation of moulds with non-quartz base sands. Arch Foundry Eng 2010;10:77–82.

[46] Chvorinov N. Control of the Solidification of Castings by Calculation. Proc Inst Br Foundrym 1938;32:229–36.

[47] Beeley P. Foundry Technology. 2nd ed. Butterworth-Heinemann; 2001.

[48] Atre S, Porter J, Batchelor T, Matthew Bulger KK, Gangopadhya P. Process Parameter Optimization for Binder Jetting using 420 Stainless Steel. Eur Congr Exhib Powder Metall Eur PM Conf Proc 2016:1–6.

[49] Hong D, Chou D-T, Velikokhatnyi OI, Roy A, Lee B, Swink I, et al. Binder-jetting 3D printing and alloy development of new biodegradable Fe-Mn-Ca/Mg alloys. Acta Biomater 2016;45:375–86. doi:https://doi.org/10.1016/j.actbio.2016.08.032.

[50] Yun B, Williams C. An exploration of binder jetting of copper. Rapid Prototyp J 2015;21:177–85. doi:10.1108/RPJ-12-2014-0180.

[51] AFS. Procedure 3301-08-S. Mold Core Handb. Third, Shaumburg, IL: AFS; 2001, p. 1–4.

[52] Primkulov B, Chalaturnyk J, Chalaturnyk R, Zambrano Narvaez G. 3D Printed Sandstone Strength: Curing of Furfuryl Alcohol Resin-Based Sandstones. 3D Print Addit Manuf 2018;4:149–56. doi:10.1089/3dp.2017.0032.

[53] AFS. Procedure 5224-13-S. Mold Core Test Handb. Third, Shaumburg, IL: AFS; 2001, p. 1–4.

[54] VDG. Biegefestigkeit von warmhärtenden, kunstharzgebundenen feuchten Formstoffen. Düsseldorf: 1999.

[55] ASTM. E290-09: Standard Test Methods for Bend Testing of Material for Ductility 2009:1–10. doi:10.1520/E0290-14.

[56] Washburn EW. The Dynamics of Capillary Flow. Phys Rev 1921;17:273–83. doi:10.1103/PhysRev.17.273.

[57] Vander Voort GF. Metallography - Principles and Practice. Materials Park, OH: ASM International; 1999.

[58] Sirivimonpan P, Osothsilp N. Effects of resin coated sand mixture on bending strength and cost. Key Eng. Mater., vol. 765 KEM, Trans Tech Publications Ltd; 2018, p. 255–9. doi:10.4028/www.scientific.net/KEM.765.255.

[59] Khandelwal H, Ravi B. Effect of binder composition on the shrinkage of chemically bonded sand cores. Mater Manuf Process 2015;30:1465–70. doi:10.1080/10426914.2014.994779.

[60] Coniglio N, Sivarupan T, El Mansori M. Investigation of process parameter effect on anisotropic properties of 3D printed sand molds. Int J Adv Manuf Technol 2018;94:2175–85. doi:10.1007/s00170-017-0861-5.

[61] Hodder KJ, Chalaturnyk RJ. Bridging Additive Manufacturing and Sand Casting: Utilizing Foundry Sand. Addit Manuf 2019. doi:10.1016/j.addma.2019.06.008.

[62] Tamas S, Dermot B. Analysis of the effects of 3DP parameters on part feature dimensional accuracy. Solid Free Fabr Symp Proc 2007:470–81.

[63] Snelling D, Williams CB, Druschitz AP. A Comparison of Binder Burnout and Mechanical Characteristics of Printed and Chemically Bonded Sand Molds. Solid Free Fabr Symp 2014:197–209.

[64] Tsumura O, Narita H, Tomigashi D, Okino M, Miyauchi K. Effects of sand grain size distribution on strength of mold. J Japan Foundry Eng Soc 2009;81:77–82. doi:https://doi.org/10.11279/jfes.81.77.

[65] Khandelwal H, Ravi B. Effect of molding parameters on chemically bonded sand mold properties. J Manuf Process 2016;22:127–33. doi:https://doi.org/10.1016/j.jmapro.2016.03.007.

[66] EnvisionTEC. Viridis3D n.d. https://envisiontec.com/3d-printers/robotic-additive-manufacturing/ (accessed September 24, 2019).

[67] Thole J, Beckermann C. Measurement of Elastic Modulus of PUNB Bonded Sand as a Function of Temperature. Int J Met 2010;4:7–18. doi:10.1007/BF03355499.

[68] Stauder BJ, Kerber H, Schumacher P. Foundry sand core property assessment by 3-point bending test evaluation. J Mater Process Technol 2016;237:188–96. doi:https://doi.org/10.1016/j.jmatprotec.2016.06.010.

[69] Meyer K, Klobes P. Comparison between different presentations of pore size distribution in porous materials. Fresenius J Anal Chem 1999;363:174–8. doi:10.1007/s002160051166.

[70] Gau C, Viskanta R. Melting and Solidification of a Pure Metal on a Vertical Wall. J Heat Transf Asme - J HEAT Transf 1986;108. doi:10.1115/1.3246884.

[71] Williams LJ, Abdi H. Fisher's Least Significant Difference (LSD) Test. In: Neil Salkind, editor. Encycl. Res. Des., Thousand Oaks, CA: Sage; 2010.

[72] Stefanescu D, Ruxanda R. Solidification Structure of Aluminum Alloys. ASM Handb. vol. 9 – Metallogr. Microstruct., ASM International; 2004, p. 107–15. doi:10.13140/RG.2.1.2892.0169.

[73] Stefanescu D. Science and Engineering of Casting Solidification. New York: Springer Science + Business Media; 2002. doi:10.1007/978-1-4757-6472-7.

Chapter 3

Pore Network in 3D Sand-Printed Molds – A Computed Tomography Scanning Study

This chapter is under review for the AFS Metalcasting Conference 2020 Proceedings: Martinez, D., Stecko, T., & Manogharan, G. (2019). Pore Network in 3D Sand-Printed Molds – A Computed Tomography Scanning Study.

Abstract

In sand casting there is a need to critically balance mold strength and porosity to promote handling strength and outgassing. The effect of binder concentration in 3D sand-printed molds for metalcasting applications is examined using Micro Computed Tomography (Micro-CT). Characterization of porosity and pore network are performed on sand molds with six different levels of binder concentration. Porosity is found to range between 39% and 43% which will influence outgassing during metal pouring. Air flow simulations are performed to examine its effects on permeability along different directions with respect to print direction. Results show an increase in tortuosity as well as a reduction in permeability along the direction orthogonal to the printing plane. Findings from this study can lead to fabricating sand molds via 3D Sand-printing by selectively engineering pore networks within the mold to increase degassing in critical sections.

3.1 Introduction

Three-dimensional sand printing (3DSP) technology has been demonstrated to provide novel opportunities to improve mechanical strength and reduce casting defects through increased control of melt filling during casting [1] and greater design complexity of castings [2, 3] and molds [4-6]. A critical aspect in 3DSP that has not been well understood and leveraged is its ability to

selectively engineer mold thermal, mechanical and degassing properties by regulating printing parameters such as layer thickness and binder deposition.

It has been shown that binder saturation, i.e., volumetric concentration of binders in no-bake sand molds affects metalcasting quality by changing the mechanical strength of the mold [7], dimensional stability of the mold due to thermal cycle [8] and binder bridge contraction during aging [9, 10]. Finally, binder concentration has been shown to change permeability which could affect outgassing of the mold during pouring in sand casting [11].

An optimum level of interconnected porosity and mechanical strength of sand mold is fundamental to produce quality castings. Firstly, if porosity is insufficient, a backpressure within the mold is created that impedes the melt from reaching every part of the sand mold. The effects of this backpressure have been observed in experimental observations using X-rays during mold filling [12] and via numerical simulation [13].

Secondly, as the mold contacts molten metal, it will generate gasses resulting from the decomposition of the binder [14] which will generate a differential pressure that must be relieved by outgassing [15].

The introduction of 3DSP adds a new dimension to these previously discussed properties due to the layer-by-layer technique of mold fabrication by selectively depositing binder (e.g., furan) to produce the mold. This characteristic introduces anisotropy which has been demonstrated to affect mechanical strength as well as permeability [16]. Micro-Computed Tomography Scanning (Micro-CT) is a non-destructive technique for high resolution imaging of 3DSP samples that has begun to be utilized [17].

Micro-CT can be employed to characterize total porosity, unconnected porosity and enables the creation of pore network models that describe pore size distribution, neck radius and tortuosity. Tortuosity is a term used to describe two different concepts, depending on the literature and approach to calculation. On the one hand, geometric tortuosity specifies the ratio between the

shortest path available to a tracer and a straight line within the sample [18]. On the other hand, flow tortuosity uses the path of least resistance as calculated based on transport modeling. Therefore, this definition of tortuosity depends on both the porous media and circulating fluid properties [19]. This work presents calculations based on the first definition of tortuosity. Based on a 3D model of the porous media (i.e., sand mold) generated through Micro-CT, numerical flow simulations must be run to determine absolute permeability.

To the best of authors' knowledge, this is the first reported study on understanding these critical properties of pore networks in 3DSP molds of varying binder saturation. The objective of this research is to study the effects of binder concentration in a no-bake mold manufactured via 3DSP, on pore structures and outgassing characteristics of sand molds via image analysis and numerical simulation. Findings from this study will provide direction for increased design and control of mold properties via 3DSP for sand casting.

3.2 Materials and Methods

3.2.1. 3D Sand Printing

3DSP samples were manufactured using a VIRIDIS 3D RAM binder jetting system with samples of each binder concentration produced in different batches. The orientation of the printed parts is shown in Fig. 3-1, here X and Y axes define the printing plane and Z axis is the build direction (i.e., the direction in which the successive layers of sand and binder are deposited on the printing bed). The expected binder concentration ranges between 1 and 3 wt.% of furan-based binder. This binder is deposited by a robotic arm in a layer-by-layer manner using printer heads activated by electric pulses.

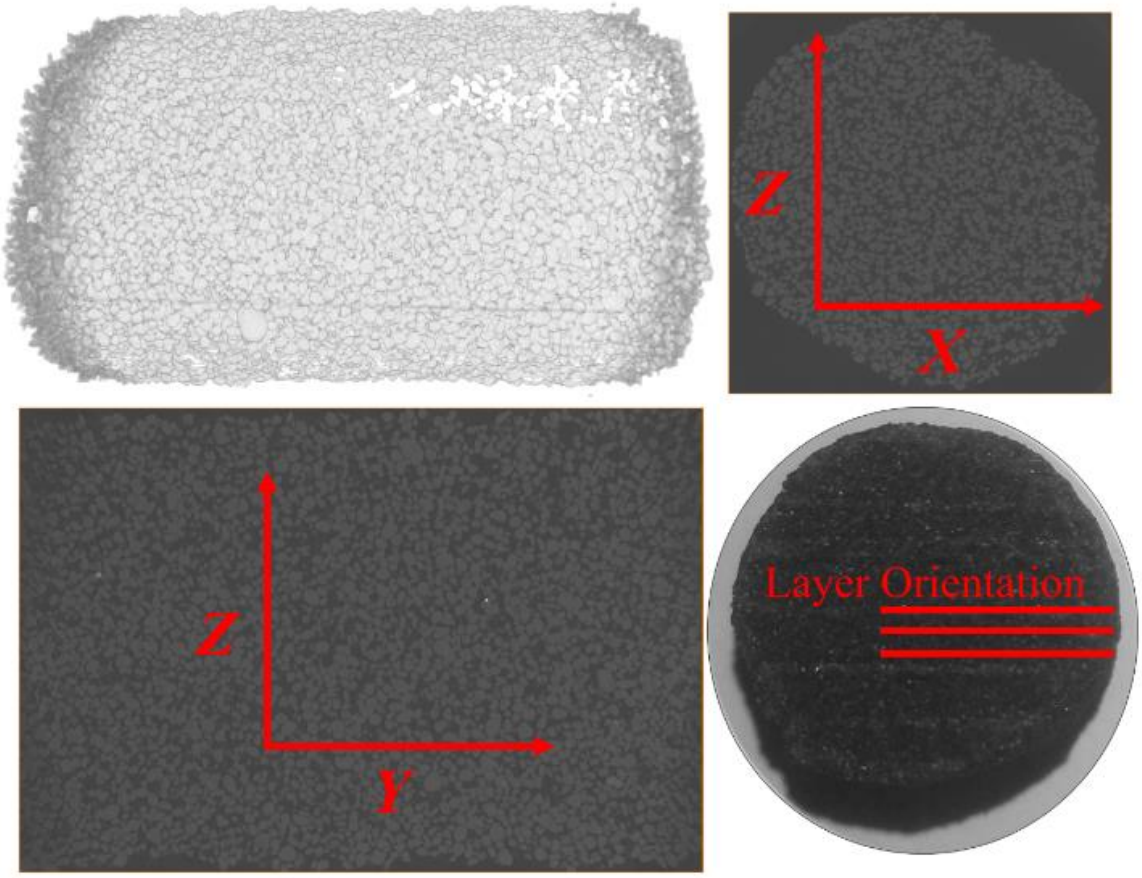

Figure 3-1. Representative Micro-CT scanning reconstructions, here axis X and Y represent the printing plane and axis Z is the direction of layer deposition

The number of electrical pulses per second sent to the printer head define the different levels of binder concentration examined in this work. The expected binder concentration per level, based on information provided by the printer manufacturer can be seen in Table 3-1.

Table 3-1. Binder concentration expected at each pulse level (wt.%)

Binder Level	Binder wt.%
$B_{1.5}$	1
B_2	1.2
$B_{2.5}$	1.8
B_3	2.1
B_4	2.5
B_5	3

3.2.2 Micro Computed Tomography Scanning

Micro-CT scanning was conducted on Ø7mm (0.2755 in) x 20mm (0.7874 in) 3DSP samples in a GE v|tome|x L300 nano/micro CT machine. Sample was scanned per binder condition at 120kV and 40mA, at a voxel resolution size of 5µm (0.000196 in). Correction for beam pre-hardening was performed using two 0.2mm (0.0078 in) aluminum filters on the detector. When the sample is rotated over 360°, grayscale images were recorded across 2100 sections using 3 images to obtain average grayscale at each section. The samples were vertically held in place during imaging using a clear glass cylinder (see Fig. 3-2).

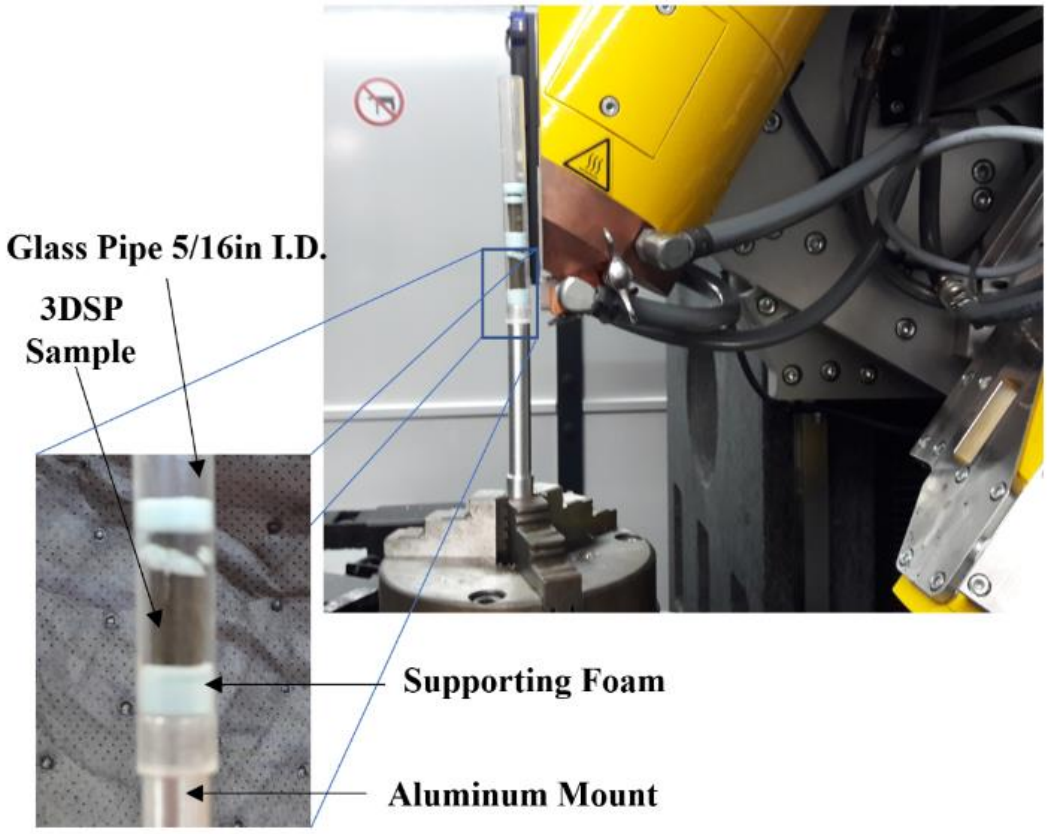

Figure 3-2. Micro-CT scanning setup showing orientation of the 3DSP sample within the machine

3.2.3 Image Processing

The first step in postprocessing of the CT scanning data was done using open-source software ImageJ. Advanced image analysis was performed in Avizo v9.4 (Thermo Fisher Scientific, Waltham, MA). A cubic sub-volume was extracted from the center of each reconstructed 3D image to focus this study on the 3D volume least affected by CT scanning artifacts that appear along the edges of the cylinder. Image segmentation was performed using auto thresholding via the “IsoData” function because of most consistent results across all samples.

Total pore volume was obtained from the number of voxels in each thresholding bin. This total porosity included unconnected and connected porosity. In order to isolate unconnected pores, the "Axis Connectivity" function was used to determine whether an individual voxel was interconnected to others of the same grayscale across adjacent voxels. The difference in the sum of interconnected voxels and total pore volume obtained in the previous step represents the volume of unconnected porosity.

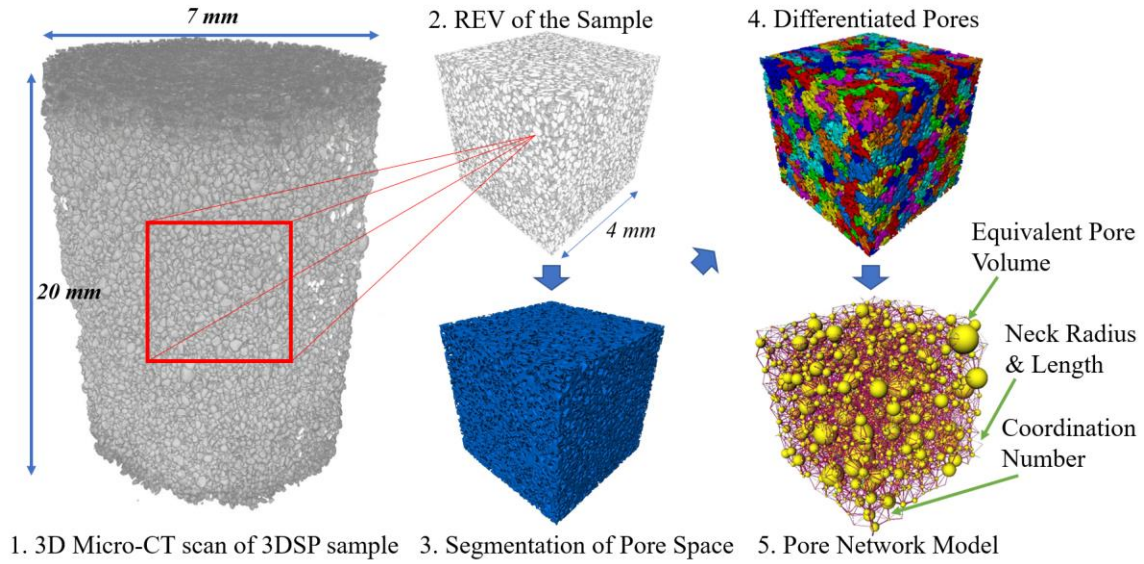

Figure 3-3. A Pore Network Model (PNM) is constructed from a cubic volume of edge length 800vx. % Porosity, pore size and neck radius are calculated for each binder level in Representative Element Volume (REV)

Finally, a Pore Network Model (PNM) was constructed to determine pore size distribution, pore coordination number, throat size and throat length distributions. Each of these values are closely linked to gas permeability and enable advanced characterization of the pore network in sand molds of varying binder saturation (see Fig. 3-3).

3.2.4 Permeability Simulations

Absolute permeability is calculated using AVIZO XLabSuit Extension package via numerical simulation across three orthogonal orientations of the 3DSP samples. Directions X and Y define the printing plane and Z represents the building direction of the 3DSP printer (i.e., the direction in which the successive layers of sand and binder are deposited on the printing bed).

Darcy's law [20], which represents the flow rate Q (m^3/s) of a single-phase fluid across a porous media as a function of pressure differential ΔP (Pa) and absolute permeability k (m^2), a constant that correlates the capacity of the media to permit fluid flow. Higher absolute permeability provides more pathways for the fluid to move within the porous media. The fluid flow is also dependent on the dynamic viscosity μ (Pa·s) of the fluid and the cross-sectional area A (m^2) and length L (m) of the sample, which can be represented as:

$$\frac{Q}{A} = \frac{k\Delta P}{\mu L} \tag{3.1}$$

Differential ΔP across the sample and dynamic viscosity of air, μ are required for the flow simulation to determine the flow rate based on steady-state Navier-Stokes equations for an incompressible Newtonian fluid. The solution is obtained for laminar flow regime [21]. All these assumptions are deemed valid for actual casting conditions. The modeling setup settings are shown in Table 3-2.

Table 3-2. Air properties and boundary conditions used in permeability simulations

Inlet pressures (kPa)	130 (18.85 PSI) and 105 (15.22 PSI)
Outlet pressure (kPa)	100 (14.50 PSI)
Dynamic Viscosity of Air at 200°C (Pa·s) (392 °F)	25.73e-6 (17.28e-6 lb/ft·s)

3.2.5 Representative Element Volume (REV)

In order to establish that the volume analyzed in this work was sufficiently large to represent accurately the pore characteristics of molds printed at the given binder concentration, a radial autocorrelation analysis was performed for each sample along with standard deviation (see Fig. 3-4) to evaluate the accuracy of the methodology employed in this study.

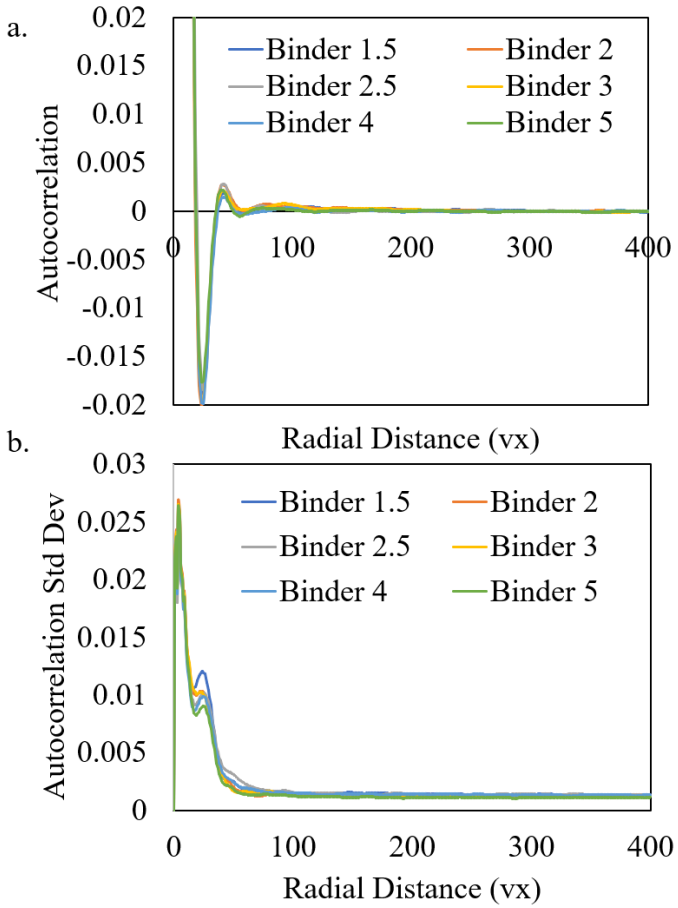

Figure 3-4. (a) Radial autocorrelation function of a CT scanned reconstruction of 3DSP samples for each binder level. For cubic volumes of a 160vx side length or larger, the sample becomes representative of the whole in all cases

Standard deviation of the autocorrelation value falls to about 1.5x10-5 across all levels above a radius of 80vx, i.e., an approximate cubic volume of 800µm (0.0314 in) x 800µm (0.0314 in) x 800µm (0.0314 in) at the voxel resolution used in this study (see Fig. 4-4). This agrees with previously reported representative volume of 3DSP sand [17]. Analysis in this study was performed on a cubic volume of 800vx x 800vx x 800vx (i.e., 4000µm (0.1574 in) x 4000µm (0.1574 in) x 4000µm (0.1574 in)).

3.3 Results

3.3.1 Pore Network Properties

Void volume ranges between 43% and 39% as binder content is increased (see Fig. 3-5). The mean value of porosity from measurements of 3 different sections are shown in the graph. Similar levels of porosity have been reported in the literature using manufacturers settings in an ExOne system. [17] A trend in reduced porosity can be observed across the binder levels, however since only one sample was examined per condition, exact correlation cannot be established. For example, the binder level 3 shows significantly lower porosity. A 37% in unconnected porosity it is observed between the lowest and highest binder content levels, although no clear tendency is observed across levels.

The unconnected porosity remains relatively similar across samples, at 0.0023%, except for the highest binder level (i.e., Binder 5) which shows a 58% increase. However, the total volume of unconnected porosity is so low that its effect on permeability can be considered negligible.

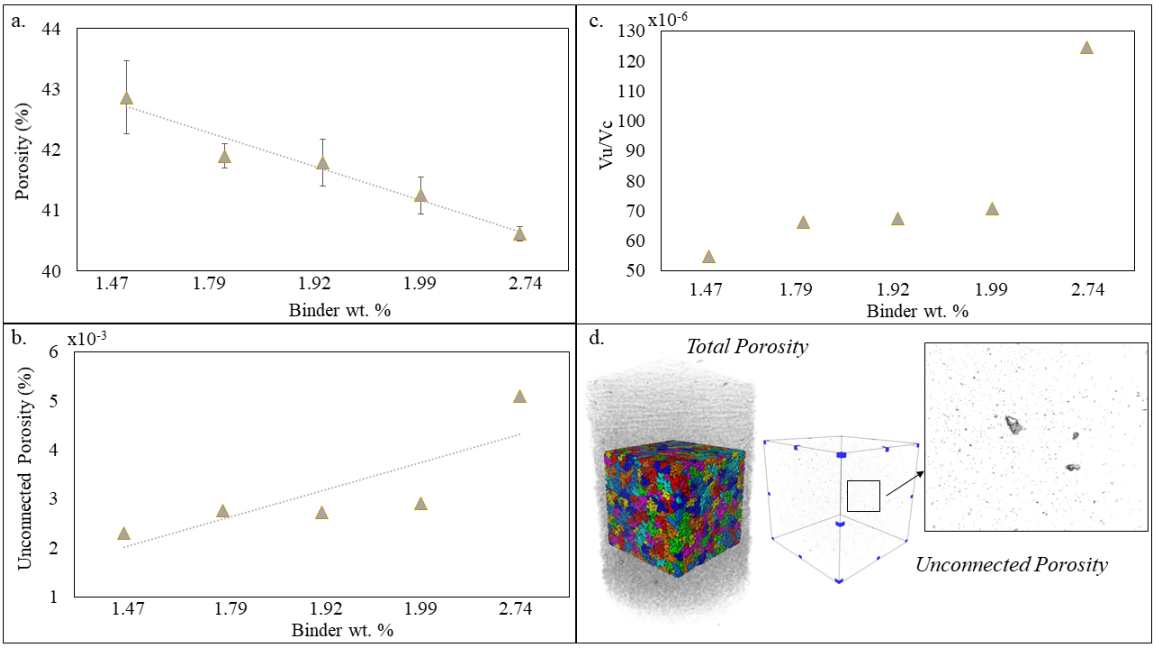

Figure 3-5. (a) Total porosity, (b) unconnected porosity % and (c) ratio of unconnected to connected porosity for the 6 binder levels. (d) Represents a schematic view of both types of porosity

The pore network that directly affects the permeability in a sample are characterized in terms of pore space, pore structure complexity and throat radius. In samples of similar pore space, smaller throat radius can lead to significantly lower permeability [22]. No clear distinction in pore size distribution (see Fig. 3-6a) and throat size is observable (see Fig. 3-6b).

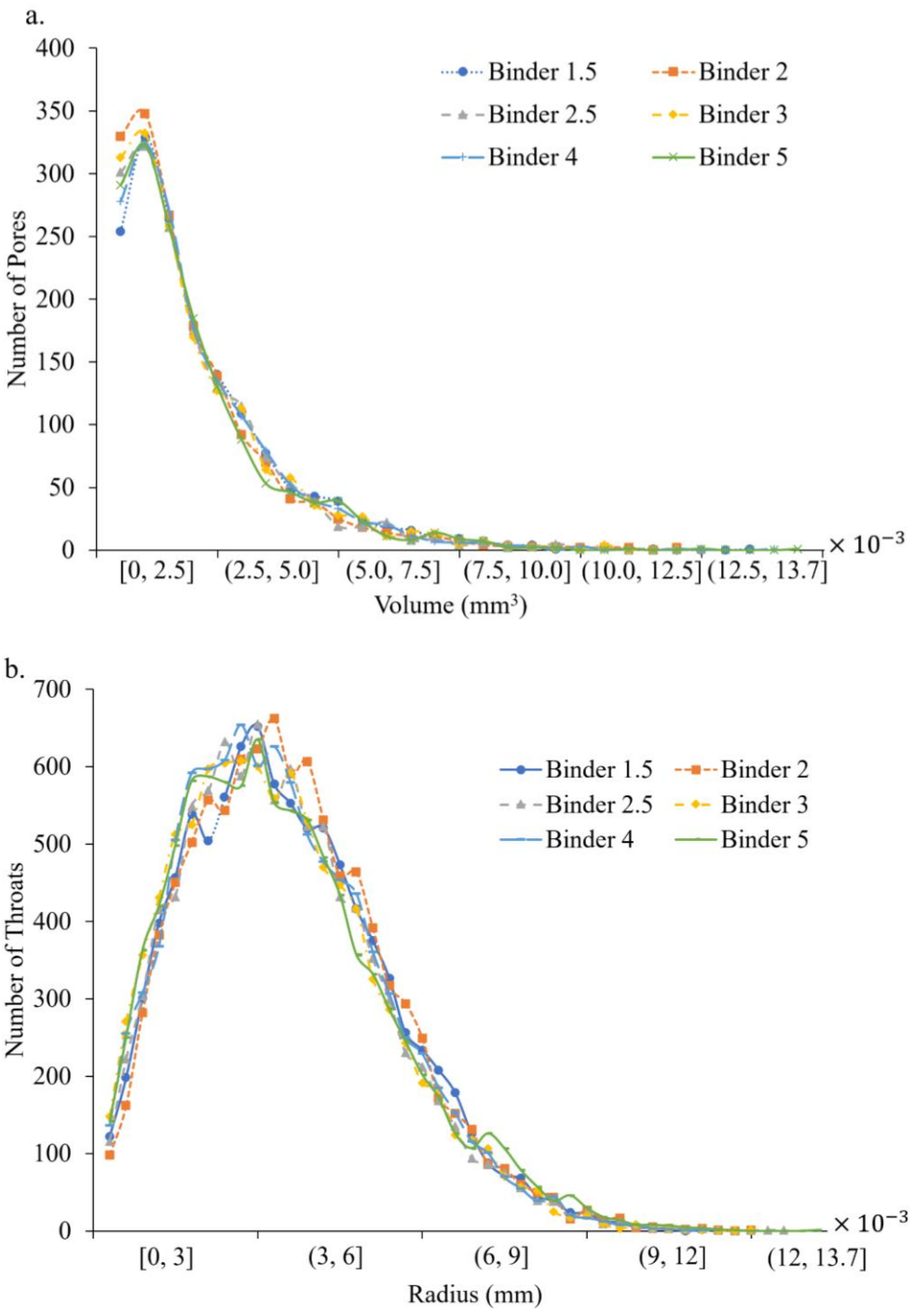

Figure 3-6. (a) Pore size distribution and (b) throat size distribution for each of the 6 binder levels

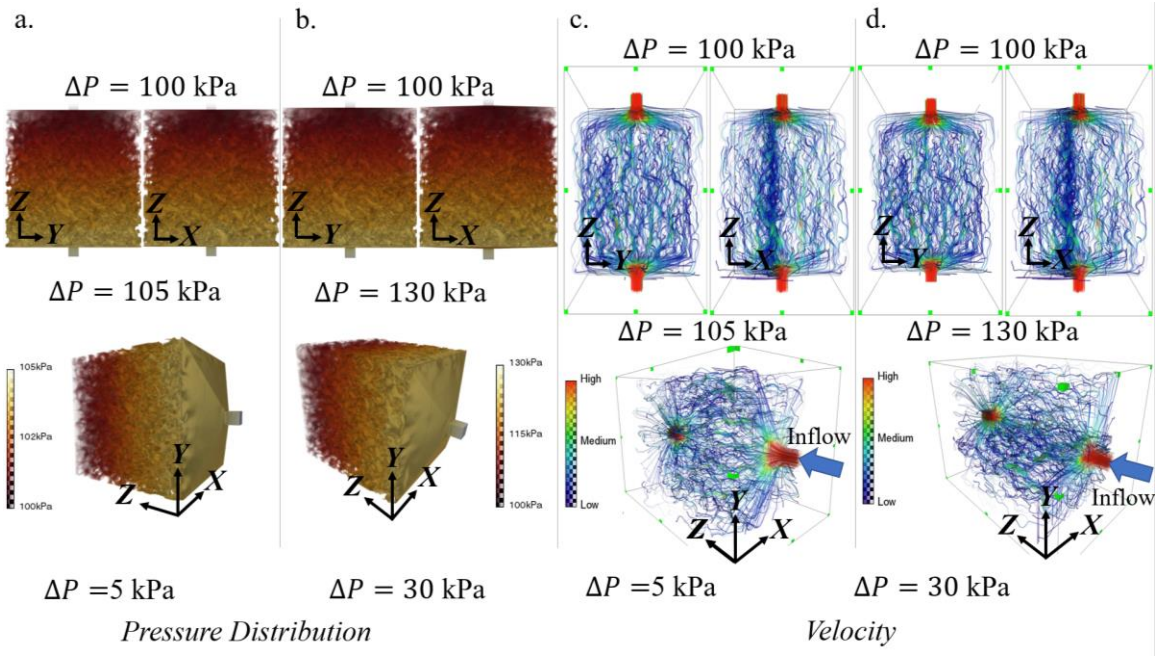

Figure 3-7. Pressure distribution across the analyzed volume of the sample for two different boundary conditions (a) ΔP=5kPa and (b) ΔP=30 kPa. Gas velocity appears to behave similarly in both boundary pressure conditions (c) ΔP=5kPa and (d) ΔP=30 kPa.

4.3.2 Permeability Simulations

The boundary pressures used for simulation does not affect the absolute permeability and only affect the flow rate of air across the modeled sample. Gas pressure applied to the sand mold will depend on the rigging design, location in the mold [23] and melt temperature [24]. In gravity sand casting, molds pressures have been reported of up to 22 kPa [11]. Differential pressure of gas flow in both directions is of interest, since mold degassing and gas flow towards the casting during blow-hole formation due to binder decomposition in the mold and cores.

Gas generation will occur at the mold or core and metal interface by water and binder vaporization [11]. In other types of casting operations such as lost-foam and low-pressure or vacuum sand casting, gas pressure or vacuum within the mold can range between 5-30kPa [24–26]

and 9-20kPa respectively [27, 28]. Simulations were conducted with a differential pressure of 30kPa and 5kPa with no observed difference in pressure distribution across the analyzed volume is observed or in the gas velocity profile (see Fig. 3-7).

Permeability simulation results show similar values in flow direction across the build direction (i.e., directions X and Y). A slight reduction in permeability is observed when the flow is oriented perpendicularly to build direction (see Fig. 3-8). This same effect has been observed in the literature [17].

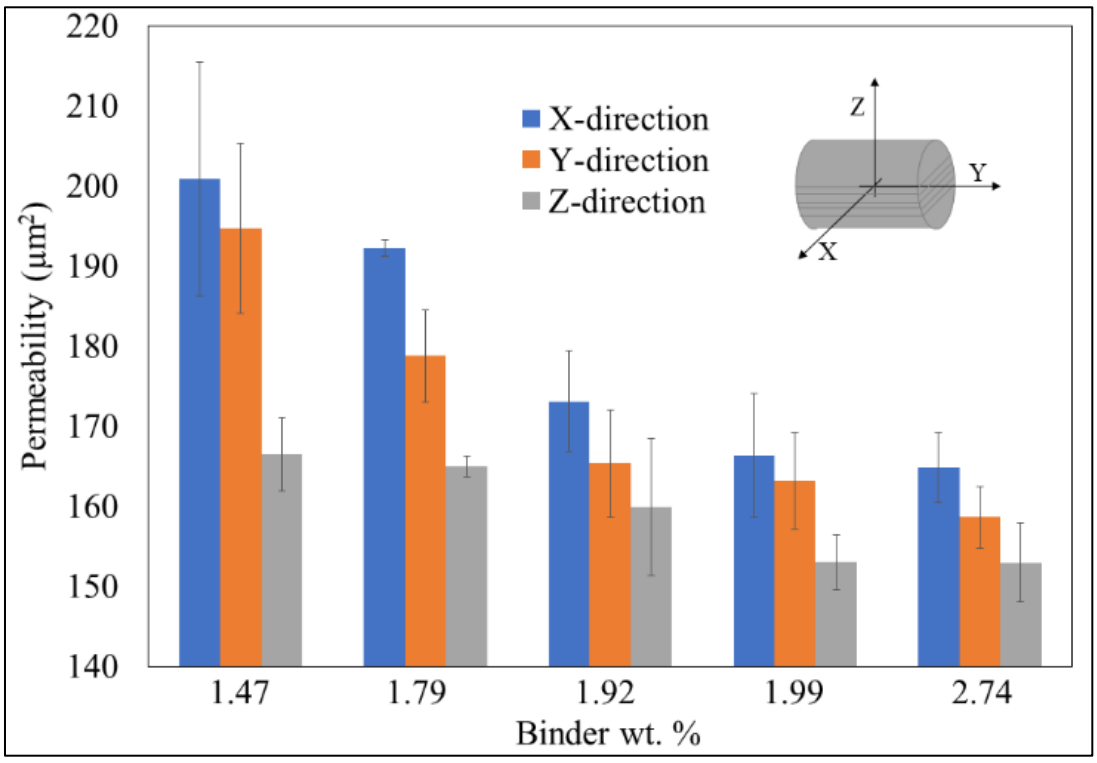

Figure 3-8. Simulation results for absolute permeability in the X (kx), Y (ky) and Z (kz) directions for the 6 binder levels. Error bars indicate standard deviation over 3 different analyzed volumes

The reduction in permeability can be correlated to an increase in the complexity of the path for gas flowing in Z direction as observed in the variation in tortuosity (see Fig. 3-9). No clear distinction observed across different binder levels which suggests that the actual pore structure does not change significantly with binder concentration and affects only the total pore volume within each sample. This same phenomenon explains the relative similarity in pore size distribution seen in the preceding section.

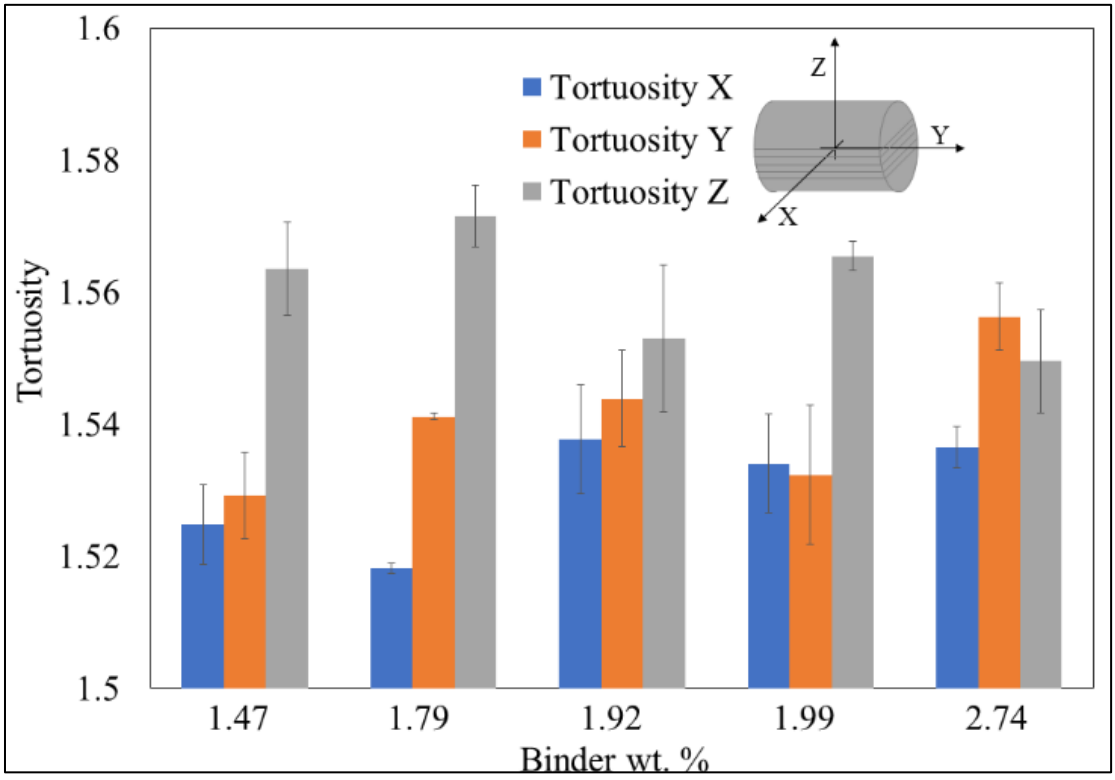

Figure 3-9. Simulation results for tortuosity in the X, Y and Z directions for the 6 different binder levels. Error bars indicate standard deviation over 3 different analyzed volumes

3.4 Conclusions

High resolution Micro-CT with prolonged exposures are required to reach proper noise-to-signal ratio that permit a correct assessment during grayscale thresholding of air, binder and sand within the image. By using 5µm resolution scanning, in this study enough detail is captured to distinguish void spaces within the 3DSP sample. Current work is underway to obtain higher resolution images to determine cured binder distribution around the sand grains. The next objective in this research is to obtain images of gas flow within the sample to allow a comparison to simulated results.

From this work the following conclusions can be drawn:

1. Micro-CT scanning can be employed for identification of pore spaces within 3DSP sample and this technique can be extended to any binder jetting system.
2. Binder concentration reduces the volume of void spaces, but no distinctive change in pore network structure is observed.
3. Permeability reduces as binder concentration increases. Permeability is reduced along the build direction when compared to flow across printing plane.

Acknowledgments

This work was funded by the EESL Green Dollars grant from the Energy and Environmental Sustainability Laboratories (EESL) of the Pennsylvania State University. The authors would like to thank the Center for Quantitative Imaging for their support during data acquisition.

References

[1] Sama SR, Badamo T, Lynch P, Manogharan G. Novel sprue designs in metal casting via 3D sand-printing. Addit Manuf 2019;25:563–78. doi:10.1016/J.ADDMA.2018.12.009.

[2] Wang J, Sama SR, Manogharan G. Re-Thinking Design Methodology for Castings: 3D Sand-Printing and Topology Optimization. Int J Met 2019;13:2–17. doi:10.1007/s40962-018-0229-0.

[3] Almaghariz ES, Conner BP, Lenner L, Gullapalli R, Manogharan GP, Lamoncha B, et al. Quantifying the Role of Part Design Complexity in Using 3D Sand Printing for Molds and Cores. Int J Met 2016;10:240–52. doi:10.1007/s40962-016-0027-5.

[4] Shangguan H, Kang J, Deng C, Hu Y, Huang T. 3D-printed shell-truss sand mold for aluminum castings. J Mater Process Technol 2017;250:247–53. doi:10.1016/j.jmatprotec.2017.05.010.

[5] Shangguan H, Kang J, Deng C, Yi J, Hu Y, Huang T. 3D-printed rib-enforced shell sand mold for aluminum castings. Int J Adv Manuf Technol 2018;96:2175–82. doi:10.1007/s00170-018-1783-6.

[6] Deng C yang, Kang J wu, Shangguan H long, Huang T, Zhang X peng, Hu Y yi, et al. Insulation effect of air cavity in sand mold using 3D printing technology. China Foundry 2018;15:37–43. doi:10.1007/s41230-018-7243-y.

[7] Khandelwal H, Ravi B. Effect of molding parameters on chemically bonded sand mold properties. J Manuf Process 2016;22:127–33. doi:https://doi.org/10.1016/j.jmapro.2016.03.007.

[8] Thiel J. Thermal Expansion of Chemically Bonded Silica Sands. AFS Proc., Schaumburg, IL: 2011, p. 1–10.

[9] Khandelwal H, Ravi B. Effect of binder composition on the shrinkage of chemically bonded

sand cores. Mater Manuf Process 2015;30:1465–70. doi:10.1080/10426914.2014.994779.

[10] Mitra S, Rodríguez de Castro A, El Mansori M. The effect of ageing process on three-point bending strength and permeability of 3D printed sand molds. Int J Adv Manuf Technol 2018;97:1241–51. doi:10.1007/s00170-018-2024-8.

[11] Monroe R. Porosity in castings. AFS Trans. 113, 2005, p. 519–46.

[12] Kimatsuka A, Ohnaka I, Zhu JD, Ohmichi T. Mold filling simulation with consideration of gas escape through sand mold. Int J Cast Met Res 2002;15:149–52. doi:10.1080/13640461.2003.11819475.

[13] Kimatsuka A, Kuroki Y. Mold filling simulation for predicting gas porosity. IHI Eng Rev 2007;40:83–8.

[14] Snelling D, Williams CB, Druschitz AP. A Comparison of Binder Burnout and Mechanical Characteristics of Printed and Chemically Bonded Sand Molds. Solid Free Fabr Symp 2014:197–209.

[15] Feng K, Lombardo SJ. Modeling of the pressure distribution in three-dimensional porous green bodies during binder removal. J Am Ceram Soc 2003;86:234–40. doi:10.1111/j.1151-2916.2003.tb00005.x.

[16] Coniglio N, Sivarupan T, El Mansori M. Investigation of process parameter effect on anisotropic properties of 3D printed sand molds. Int J Adv Manuf Technol 2018;94:2175–85. doi:10.1007/s00170-017-0861-5.

[17] Sivarupan T, El Mansori M, Daly K, Mavrogordato MN, Pierron F. Characterisation of 3D printed sand moulds using micro-focus X-ray computed tomography. Rapid Prototyp J 2019;25:404–16. doi:10.1108/RPJ-04-2018-0091.

[18] Adler PM. 2 - The Geometry of Porous Media. In: Adler PM, editor. Porous Media, Boston: Butterworth-Heinemann; 1992, p. 9–54. doi:https://doi.org/10.1016/B978-0-7506-9236-6.50007-X.

[19] Ghanbarian B, Hunt AG, Ewing RP, Sahimi M. Tortuosity in porous media: A critical review. Soil Sci Soc Am J 2013;77:1461–77. doi:10.2136/sssaj2012.0435.

[20] Darcy H. Les Fontaines Publiques de la Ville de Dijon. Paris: Dalmont; 1856.

[21] ThermoFisher Scientific. Thermo Scientific Avizo Software 9 User's Guide. 2018.

[22] Xu H, Fan Y, Hu F, Li C, Yu J, Liu Z, Wang, F. Characterization of pore throat size distribution in tight sandstones with nuclear magnetic resonance and high-pressure mercury intrusion. Energies 2019;12. doi:10.3390/en12081528.

[23] Mirbagheri SHM, Silk JR, Davami P. Modelling of foam degradation in lost foam casting process. J Mater Sci 2004;39:4593–603. doi:10.1023/B:JMSC.0000034154.00641.0b.

[24] Khodai M, Mirbagheri SMH. Behavior of generated gas in lost foam casting. World Acad Sci Eng Technol 2011;50:479–83.

[25] Liu XJ, Bhavnani SH, Overfelt RA. Measurement of kinetic zone temperature and heat Transfer coefficient in the lost foam casting process. ASME Int. Mech. Eng. Congr., 2004, p. 411–8. doi:10.1115/IMECE2004-59348.

[26] Liu XJ, Bhavnani SH, Overfelt RA. Simulation of EPS foam decomposition in the lost foam casting process. J Mater Process Technol 2007;182:333–42. doi:10.1016/j.jmatprotec.2006.08.023.

[27] Puga H, Barbosa J, Azevedo T, Ribeiro S, Alves JL. Low pressure sand casting of ultrasonically degassed AlSi7Mg0.3 alloy: Modelling and experimental validation of mould filling. Mater Des 2016;94:384–91. doi:https://doi.org/10.1016/j.matdes.2016.01.059.

[28] Jiang W, Fan Z, Liao D, Dong X, Zhao Z. A new shell casting process based on expendable pattern with vacuum and low-pressure casting for aluminum and magnesium alloys. Int J Adv Manuf Technol 2010;51:25–34. doi:10.1007/s00170-010-2596-4.

Chapter 4

Novel Mold Design to Improve Mechanical Properties in Castings

This chapter is currently under-review for publication in Journal of Manufacturing Science and Engineering: Martinez, D., Sama, S. R., Toykoc, H., Sim, J., & Manogharan, G. (2019). Novel Mold Design to Improve Mechanical Properties in Castings.

Abstract

Additive Manufacturing (AM) is accepted as a transformative technology for rapid production of parts based on digital models through direct printing of a range of materials (e.g., metals, polymers, and ceramics). Recent advancements in binder-jetting AM process, i.e. 3D Sand-Printing (3DSP) enables direct production of sand molds and cores for metal casting. AM has been attractive to manufacturers due to the ability to produce complex and customized parts in low batch production. Traditional mold design for gravity castings experience higher scrap rate due to challenges in controlling turbulence and air entrapment. In this research, mathematically designed sprue geometries that can be produced via 3DSP are presented along with its effects on mechanical and metallurgical properties of castings through numerical modeling, computational simulation and experimental validation. The casting properties are contrasted to conventional straight sprue, for two different alloys: aluminum alloy 319 and gray iron Class 30. Scanning electron microscopy (SEM), energy dispersive X-Ray spectroscopy (EDS), computed tomography scanning (CT) and 3-point bending tests are performed to characterize microstructure, casting defects, elemental composition and mechanical properties for castings via each gating design system. It was found that statistically significant increase of 10% in flexural strength using conical-helix sprue geometry and a reduction of 25% in casting defects in Al 319 through the proposed sprue design. In gray iron Class 30, no statistically significant differences are found between the flexural strength of conical-helix and benchmark straight sprue as expected in a short freezing range alloy.

4.1 Introduction

Metal casting industry is one of the largest contributors to the world's economy as castings are incorporated in a large variety of mechanical systems using substantially higher number of qualified alloys (when compared to direct metal AM) [1]. By 2025, the metal casting market is projected to reach 39.94 billion USD, an increase of over 97% from 2017. One of the major drivers for this growth is the fuel efficiency requirements of the motor industry which is expected to occur in lightweight alloys which are often manufactured via casting processes [2]. "In-direct" metal AM through 3D Sand-Printing (3DSP) represents a significantly cheaper and faster means of producing metal parts when compared to direct metal AM [3,4]. 3DSP enables a tooling-less approach to fabricate molds and cores through binder-jetting AM process. Mold fabrication is the longest and most expensive step of the casting process. Implementation of 3DSP has been shown to reduce costs and delays by seamlessly integrating into traditional foundry's manufacturing cycle with minimum disruption on the production floor (i.e., 3DSP → Melt Pouring → Shake-Out/Cleaning) [5–8]. In addition, the layer-by-layer method of manufacturing sand molds increases the achievable complexity of geometries in gravity casting [9]. Finally, the variety of alloys that are qualified for metal casting is much broader than those for direct metal AM [10].

The gating system is a critical design element in a sand mold, since it directly affects the turbulence and velocity of melt flow during mold filling which ultimately affects the mechanical performance of castings [11–13]. Liquid metal flow through confined spaces (i.e., sprues, runners) cause flow turbulence due to surface friction and head loss at bends which often results in entrainment defects [14]. Bi-films are oxide layers formed on the liquid metal surface that are folded onto themselves and often include trapped sand and are among the most common defects that result from entrainment [15]. Bi-films manifest themselves as thin and long voids in the final casting's surface and inner structure resulting in highly detrimental cracks [16]. Larger disturbances

in the liquid metal surface cause the bi-films to entrap air resulting in gas porosity within castings. This detrimental entrainment mechanism must be addressed during mold design and pouring processes to ensure required physical properties of the casting [17]. Over 70% of all metal castings produced every year employ traditional sand-casting with an average scrap rate of 35%, where 87 % of all the scraps are caused by turbulent flow and feeding defects in the mold design [18,19].

Current advancements in flow simulations allow designers to analyze and predict flow characteristics prior to actual casting (in addition to solidification modeling). The main purpose of the flow simulations is to verify whether the mold and filling system design can effectively minimize double-oxide-film defect formation due to surface turbulence, bubble trails and surface arrest [20]. The primary criterion to prevent in-mold turbulence is to preserve the filling velocity under 0.5 m/s, which is the critical ingate velocity for most metals. Above this velocity, the liquid metal surface starts to fold onto itself and causes entrainment [17,20]. However, it is important to note that the current simulation solutions are designed for molds and filling system built using traditional sand-molding techniques and do not consider the design freedom offered by 3DSP.

The recent adoption of 3DSP technology has allowed the manufacturing of highly sophisticated gating system geometries through a binder-jetting AM process which do not require patterns or core/mold boxes [5]. Since the gating system directly influences the flow characteristics of the liquid metal during the casting process, the design freedom offered by 3DSP presents a novel opportunity to achieve drastically improved casting properties by reducing casting defects. A recent study on stainless steel 17-4 casting via 3DSP has established that novel 3D sprue geometries with parabolic and conical-helix profiles provide overall casting defect reductions of 56% and 99.5%, respectively, when compared to a conventional straight sprue. Similarly, analysis of oxide inclusion showed a reduction of 21% and 35%, respectively [21]. However, there is a knowledge gap to evaluate its efficacy on alloys of varying freezing range. Freezing range of a metal is defined as the differential between the liquidus and solidus temperatures in an alloy’s phase diagram. Several

studies have shown the importance of freezing range which is dictated by the alloy composition which modifies the fluidity of the molten alloy and its solidification behavior [22–24]. The overall goal of this research is to address this gap by evaluating flow induced casting defects in short freezing range alloys (e.g., gray iron CL 30) and long freezing range alloys (e.g., aluminum alloy 319) via novel sprue geometries achieved through 3DSP.

4.2 Background

Multiple studies have well established that oxide film defects play a major role in the mechanical properties of aluminum alloy castings [25–29]. The findings extend from illustrating fatigue crack initiation due to oxide films [28], to loss of tensile properties based on areal distribution of oxide films and porosity in aluminum castings [29]. Understanding the effect of oxide films has led researches to explore alternative mold design approach in traditional mold-making, specifically on sprue-runner geometries and ingate orientations in order to reduce oxide formation and improve final quality of metal castings in limited traditional mold-making processes [21,25,27,30,31]. Runner profiles significantly affect the total volume of defects, number of inclusions and their distribution across the casting in aluminum alloys[21]. Incorrectly positioned filling systems result in premature mechanical failing and lower fracture strength in A1−7Si−Mg alloys [25]. In gray cast irons, it has been shown that reducing the ingate flow velocity of the molten metal eliminates turbulent flow and prevent oxidation defects and sand inclusion [32,33].

Other approaches in redesign of traditional sprue-runner system have included diffusing runners [34] and modified sprue wells [32]. Reported studies were aimed at decreasing ingate flow velocity while accounting for the limited design opportunities in conventional fabrication of sand molds for gravity casting. The runner geometry profiles used in these studies were: rectangular, circular or triangular cross-sections and the angles of the sprues were nearly vertical. More recently,

a new pouring basin geometry that employs features such as multiple sprue exits, a slag trap and an undercut to prevent splashes was modeled, as a means of exploring advantageous designs made possible via 3DSP [9], resulting in improved flow regime simulations. A follow up study employed this design system through parabolic and conical-helix profiles, to produce 17-4 stainless steel castings with significant improvements in defect volume and mechanical strength [21].

The relation between the freezing range of materials and porosity has been extensively researched [35–41] and major characteristic behaviors of short and long freezing alloys are summarized in Table 4-1. There are several well-established studies in literature focused on the freezing range of casting alloys and its effects on porosity [42–44]. It must be noted that the two main porosity forming mechanisms (i.e., shrinkage micro-porosity and feeding centerline porosity) are not mutually exclusive and often appear in conjunction. The solidification mode of long freezing alloys which develops dendritic structures across the casting to form a mushy state results in a reduced feeding distance because liquid metal must circulate in what is effectively a “porous” media following Darcy’s law. This phenomenon then relates to the type of porosity common to these alloys and its short feeding distance [39,41]. Micro-porosity is formed as the mushy zone provides nucleation sites that can grow as the pressure drops because of the increased resistance to liquid metal flow [42]. Meanwhile, short freezing range alloys have solidification fronts that are initiated near the mold walls and therefore tend to display centerline shrinkage [41].

Table 4-1. Solidification characteristics of short and long freezing range alloys

Solidification Characteristics	Short Freezing Range	Ref.	Long Freezing Range	Ref.
Initiation	Planar front from walls	[43]	Metal front	[43]
Mode	Clearly defined solid/liquid shell	[41,44]	Mushy transitional state	[41,44]
Direction	Shows directional solidification	[45]	No directional solidification	[45]
Porosity	Centerline shrinkage and hot spots	[41]	Finely dispersed internal porosity and hot spots	[41]
Feeding distance	Long	[43]	Short	[43]

In aluminum alloys, adding Cu tends to increase fluidity, reaching a maximum level at the eutectic alloy (Cu wt.% 33). However, when Cu is below 10 wt.%, fluidity is reduced when compared to the pure element [43,45,46]. The addition of Si tends to increase fluidity at eutectic levels (Si wt.% 12) [46–48]. The combined effect of these alloying elements, intrinsic high fluidity of pure aluminum (~1.3 mPa·s at melting point [49]) and low thermal gradients results in a long freezing range alloy Meanwhile, cast iron exhibits much higher viscosity than aluminum (~9.3 mPa·s at liquidus point [50]) with higher thermal gradients due to higher liquidus temperature, i.e., a short freezing range alloy. In summary, review of current literature illustrates the prevalence of casting defects due to turbulent flow in sand-molds and the potential of 3DSP-enabled mold design to address this challenge. The motivation of this study is to evaluate the effects of freezing range of alloys on the effectiveness of novel 3DSP mold design, i.e., mechanical properties and casting defects.

4.3 Methodology

4.3.1 Sprue Design and Casting

Three fundamental mold design constraints have been established in the casting literature to reduce entrainment via hydrodynamic studies: (1) ingate velocity must be below or equal to the critical velocity [17,51,52], (2) length of the sprue must be minimized to reduce thermal losses [53], and (3) sharp turns should be avoided [17]. Two mathematically designed sprues (conical-helix and parabola) are developed and evaluated under these constraints to derive optimum geometrical parameters via a sequential quadratic programming constrained optimization algorithm. The profile of these sprues can be expressed as:

Conical –Helix Profile

$$x = tr\cos(\alpha t) \quad (4.1.a)$$

$$y = tr\sin(\alpha t) \quad (4.2)$$

$$z = h_{sprue} - t \quad (4.3)$$

Parabolic Profile

$$y = a(x-b)^2 - ab^2 \quad (4.1.b)$$

The primary constraining factor in mold-design is that the velocity of the melt-front at the ingate, this must be less than or equal to the critical velocity (0.5 m/s for most alloys [17,20]). The optimization objective is to minimize the curve length of each sprue profile through respective design variables: α – angular frequency and r- radius of the conical-helix and a and b – geometry parameters of the parabola as a function of alloy properties and casting geometry [9]. After designing the optimized flow curve for the sprue profile, the sprues were designed by lofting a constant circular cross-section along the curves. In this study, the casting benchmark is based on well-studied Yang's offset sprue and mold [20] and the molten alloy properties for aluminum alloy

319 ($T_m = 933\ K$ [54], ρ = 2357 kg/m^3 [55], $\eta_{T_m} = 1.5\ mPa \cdot s$ [54] and CL 30) ($T_{Liquidus}$~$1514\ K$ [56], ρ = 6600 kg/m^3 [57], $\eta_{T_{liquidus}} = 9.3\ mPa \cdot s$ [58]).

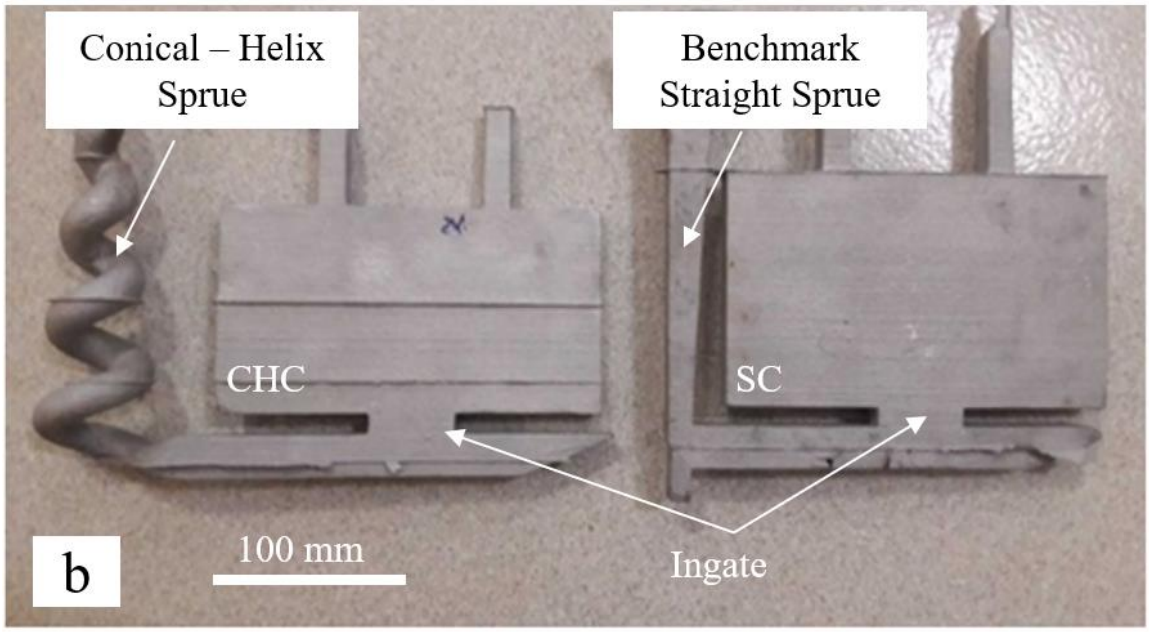

Figure 4-1. Final aluminum alloy 319 castings with straight and conical-helix sprues.

Three types of sprue were examined for gray iron, a conical-helix profile (CHC), a parabolic profile (PC) and a benchmark straight sprue design (SC). For Al 319, a conical-helix profile sprue was compared to the benchmark straight sprue design (see Fig. 4-1). The sprue height was maintained at 200 mm to induce equal head height and sprue wells were not used in 3DSP parabolic and conical-helix castings to disregard its argumentative benefits [17]. The mold dimensions are shown in Fig. 4-2. The molds were printed in a Viridis3D RAM machine at a layer thickness of 0.4 mm using silica sand mixed with an acid catalyst. In this binder-jetting AM process, foundry silica sand is spread layer-by-layer along with selectively deposited furan-based binder based on CAD model until the mold is completed. The number of castings per alloy per sprue

design was n=3. Slag filters were not included in the study in order to isolate the effects of mold-design on flow-related casting performance.

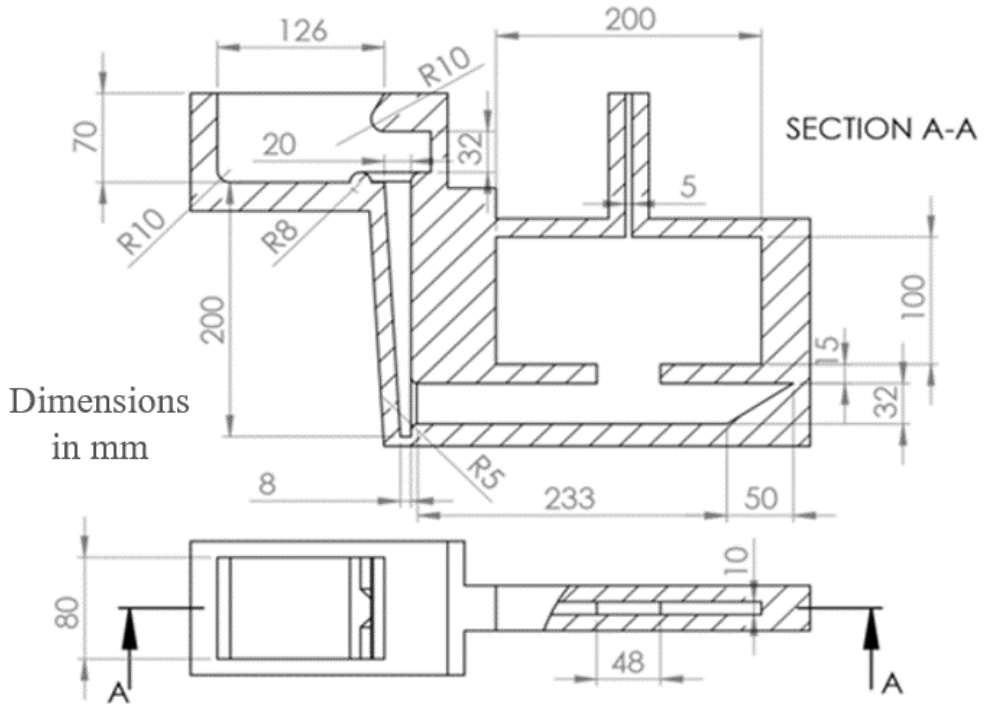

Figure 4-2. Dimensions of straight-gating system and casting. Aluminum alloy 319 cast plates - 15mm thick and gray iron - 10mm thick

4.3.2 Computational Fluid Flow Modelling

Flow simulations were constructed to analyze mold-filling velocity and air entrainment levels in each castings based on alloy properties, mold design and pouring conditions ($T_{pouring} = 923\ K$ with a filling flow rate of 0.00045 m^3/s for Al 319 and $T_{pouring} = 1558\ K$ with the same flow rate for gray iron). Simulations were conducted in Flow-3D Cast (V5.0), by Flow Science, Inc. (Santa Fe, NM). The software solves the Navier-Stokes equations to determine velocity of the

melt, and by applying a volume-of-fluid method, the free surface geometry is calculated, both calculations occur for each time step. Air entrainment is calculated using an imbedded function in Flow-3D which estimates its formation due to free surface disturbances. At the melt-air interface, the rate of entrainment $\left(\frac{\partial \forall}{\partial t} - \frac{m^3}{s}\right)$ is a function of turbulent kinetic energy ($k - \frac{m^2}{s^2}$), surface tension ($\sigma - \frac{kg}{s^2}$) and gravity ($g - \frac{m}{s^2}$) obeying the following rule [59]:

$$\frac{\partial \forall}{\partial t} = C_{air} A_s \left[2 \left(\frac{\rho k - \rho g_n L_t - {}^{2\sigma}/_{L_t}}{\rho} \right)^{1/2} \right] \tag{4.4}$$

4.3.3 Computed Tomography Scanning

3D computed tomography scans of castings were obtained using a GE v|tome|x L300 nano/microCT machine at 270 kV and 300A, with a 0.5mm Cu filter in the detector and a 0.5 Sn filter in the tube. The voxel resolution was set to 109µm in all three directions. Three independent binary classification algorithms were used to determine porosity and size of voids. The motivation for using these three algorithms was to contrast them to one another and confirm that no systematic errors were involved in the image analysis. All three algorithms were developed for multimodal histograms, the first was developed by Yen et al. [60], the second is based on Rényi entropy and developed by Pun [61,62], and the third is the Maximum Entropy Method created by Kapur et al. [63].

4.3.4 Microstructure

SEM analysis was performed using a FEI Nova NanoSEM 630 SEM. Imaging was done in the range from 10 to 500µm for all samples at a maximum energy of 20keV. The alloy samples were extracted from the ingate zone as shown in Fig. 4-3. Sample sizes for Al 319 were 12mm cubes and 12x12x6mm^3 for gray iron. The samples were observed as-polished at 1µm level with no chemical etching.

4.3.5 Mechanical Testing

Effects of novel sprue geometries were assessed via flexural testing performed according to ASTM E290 standard [64]. Eight samples of 80mmx12mmx4.25mm were machined from each casting using a conventional vertical milling machine. Casting "edge effects" were disregarded by extracting four samples, in the vertical and horizontal direction, from the center of the plate as shown in Fig. 4-3. The edge effect in castings results in an increased mechanical strength away from the center of the plate compared to bulk mechanical properties, due to increased cooling rate [65]. Three-point bending test was performed using an MTS QTest/100 machine with a 100 kN cell at a loading rate of 0.42mm/s. Flexural stress (σ_{flex}) was calculated using the following expression:

$$\sigma_{flex} = \frac{3FL}{2wt^2} \tag{4.5}$$

where, F is the applied force (kN), L is the length between supports (mm), w is the width of the specimen (mm) and t is its thickness (mm). The support length was set at $16 \times t$ as per ASTM E290 standard.

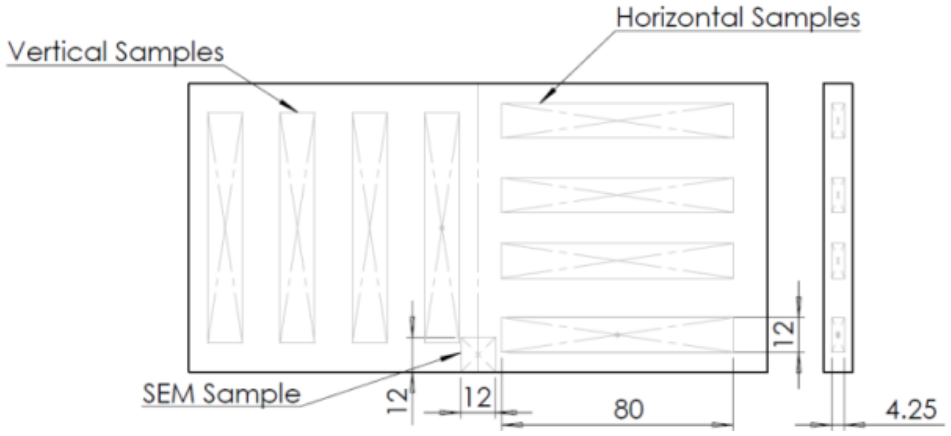

Figure 4-3. Samples extracted from casting plates (Dimensions in mm)

4.4 Results and Discussion

4.4.1 Castings

All cast plates were successfully filled. Visual inspection of the gray iron SC plate showed several surface open pores, whereas no defects were observed on castings with proposed sprue profiles - PC and CHC as shown in Fig. 4-4. These defects were not included in the CT scanning image analysis since all exterior surfaces were cropped before analysis to eliminate cast surfaces for conservative analysis. Al 319 plates showed similar surface finish with no notable defects in PC and CHC profiles.

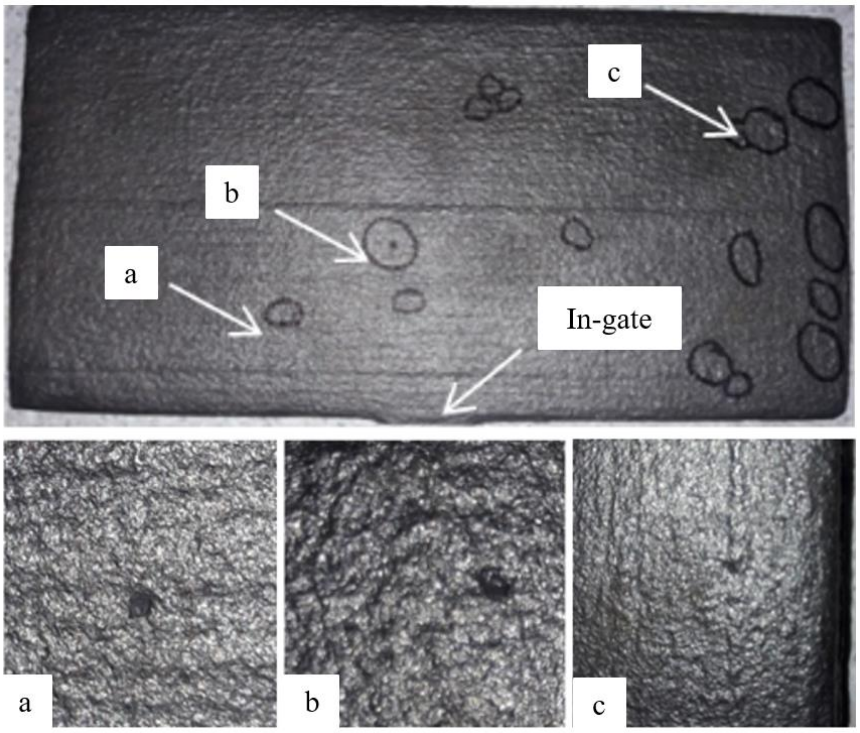

Figure 4-4. Surface defects on gray iron SC plate (a-c)

4.4.2 Flow Simulations

Numerical simulations for cast iron resulted in the expected reduction in velocity at the ingate in CHC sprue. However, the optimized PC sprue still violates the critical velocity limit (see Fig. 4-5). The benchmark sprue displays fountaining towards the sprue which agrees with simulation results from the literature [21]. However, experimental observations from CT analysis show fountaining in the opposite direction [66].

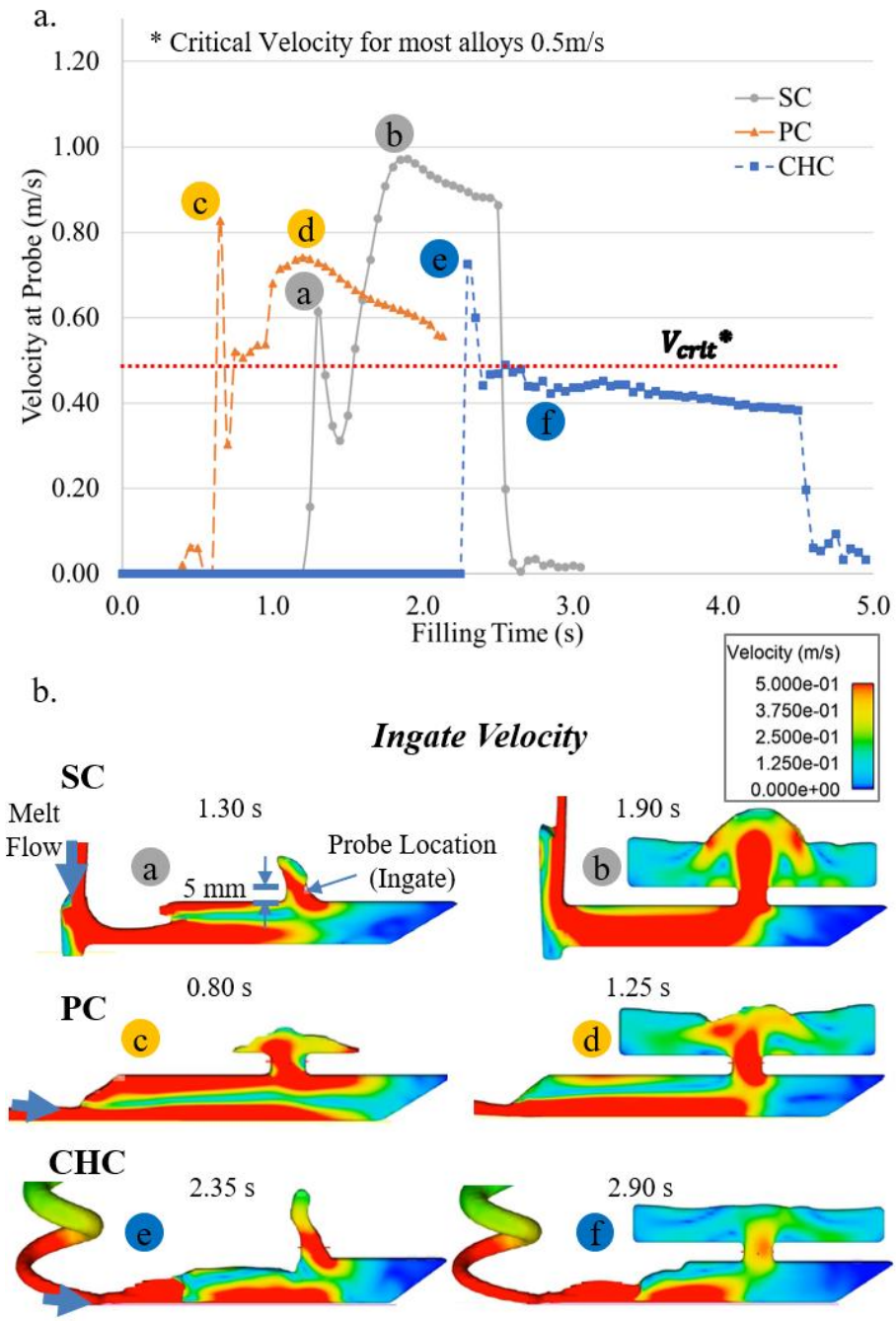

Figure 4-5. Numerical Modeling results for gray cast iron. After initial filling, only in the CHC sprue is velocity at the probe maintained below the critical value (a), significant points during filling are shown in (b). Probe is located 5mm above the center of the ingate in all cases.

This could be attributed to the straight runner end design used in this experimental work. Simulations run show that initial fountaining is due to the reflected melt wave. The pressure peaks shown in Fig. 4-6a are the results of the initial contact of the melt with the mold top. Similar air entrainment is observed in the PC and SC cases, whereas peak entrainment is minimized in the CHC sprue (see Fig. 4-6b). The area under each entrainment curve is calculated to evaluate the total air entrainment entering the mold through the ingate. However, it must be noted that this only represents total air entrainment at the probe point, i.e., center of the ingate.

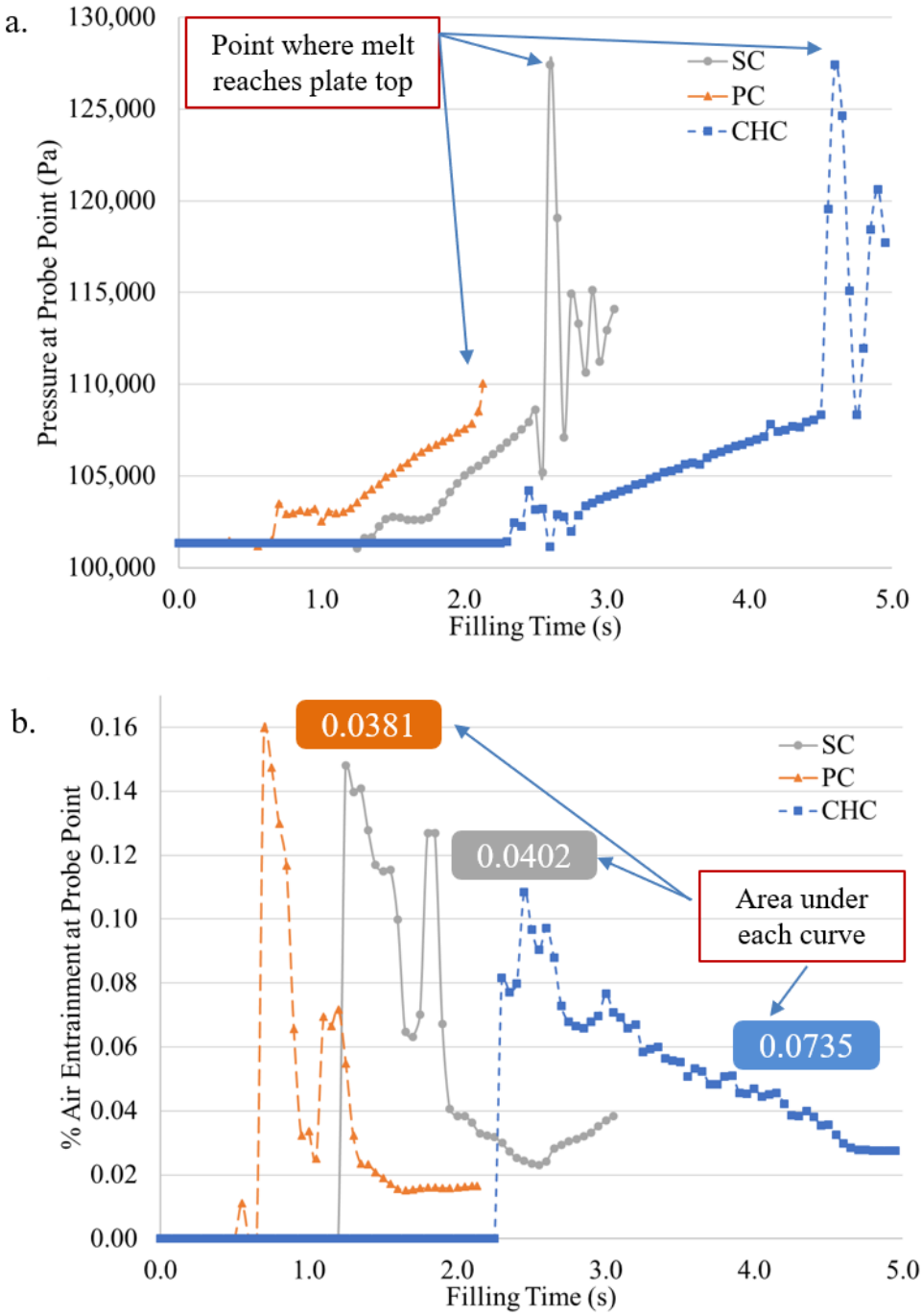

Figure 4-6. (a) Pressure curves at the ingate location of the probe, pressure peak shows time at which gray cast iron melt reaches the plate top. (b) Peak entrainment at the probe point is maximum for PC, while area under the entrainment curve is largest for CHC

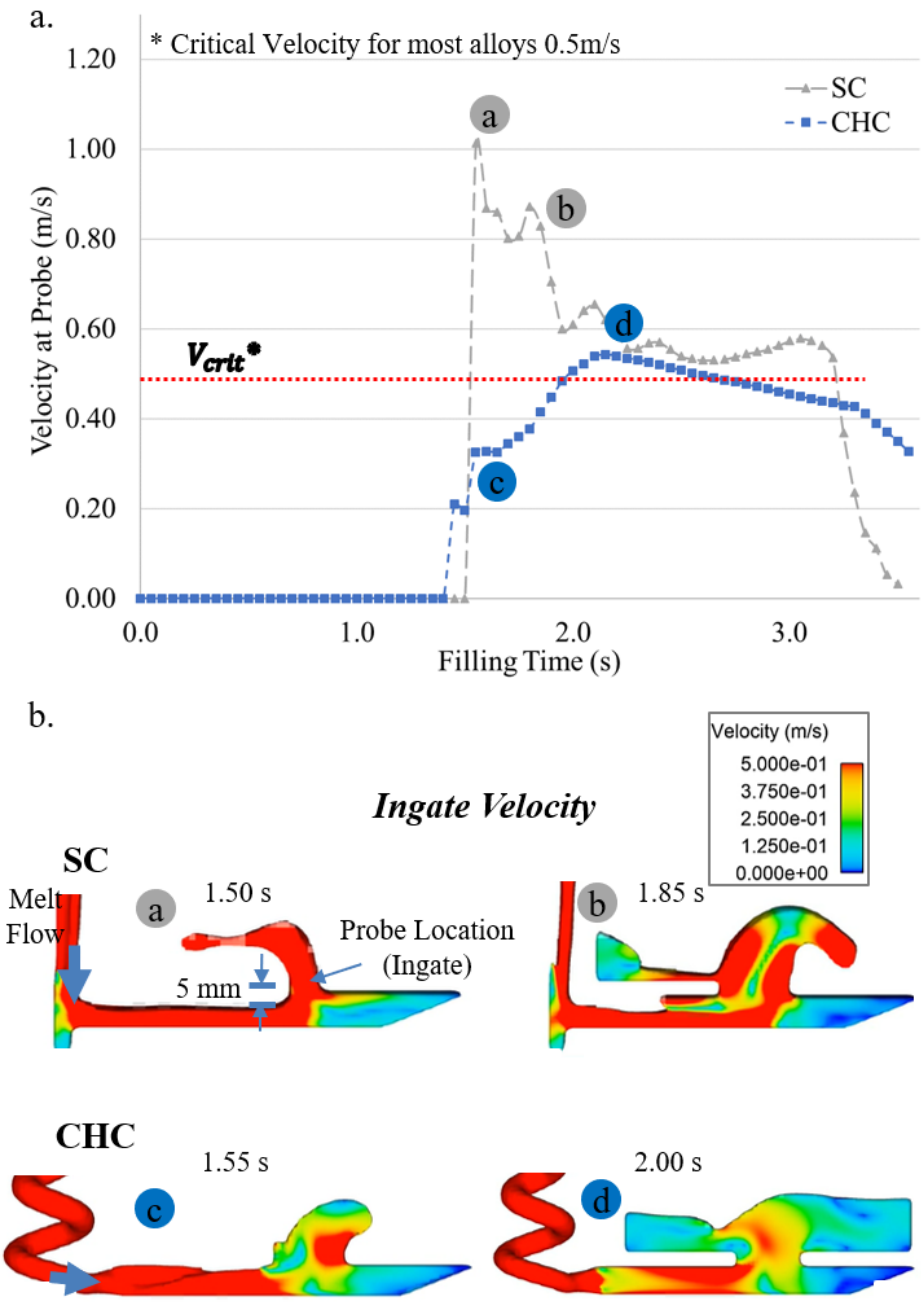

Figure 4-7. Numerical Modeling results for aluminum alloy 319. After initial filling, only in the CHC sprue is velocity at the probe maintained below the critical value (a), significant points during filling are shown in (b). Probe is located 5mm above the center of the ingate in all cases.

In aluminum alloy 319, velocity is once again significantly lowered in the mathematically designed sprue (see Fig. 4-7). Air entrainment is reduced in CHC sprue 42% (see Fig. 4-8). Initial fountaining is observed in the sprue side which is contrary to experimental observations in aluminum [20,67] which could be attributed to the straight runner end design used in this experimental work.

In both alloys, simulations show a reduction in fountaining, reduced turbulence and quiescent filling in mathematically designed sprues which is in agreement with results obtained in other alloys [21].

An effect that is not accounted for in the simulations run for both of these alloys is the effect of melt cooling during mold filling. The mathematically designed sprues tend to fill the mold slower than the conventional straight sprue. This slower cooling allows for more cooling to occur which could have effects on both defect formation and microstructure. The effects of temperature will have to be dissociated from sprue design in a future study.

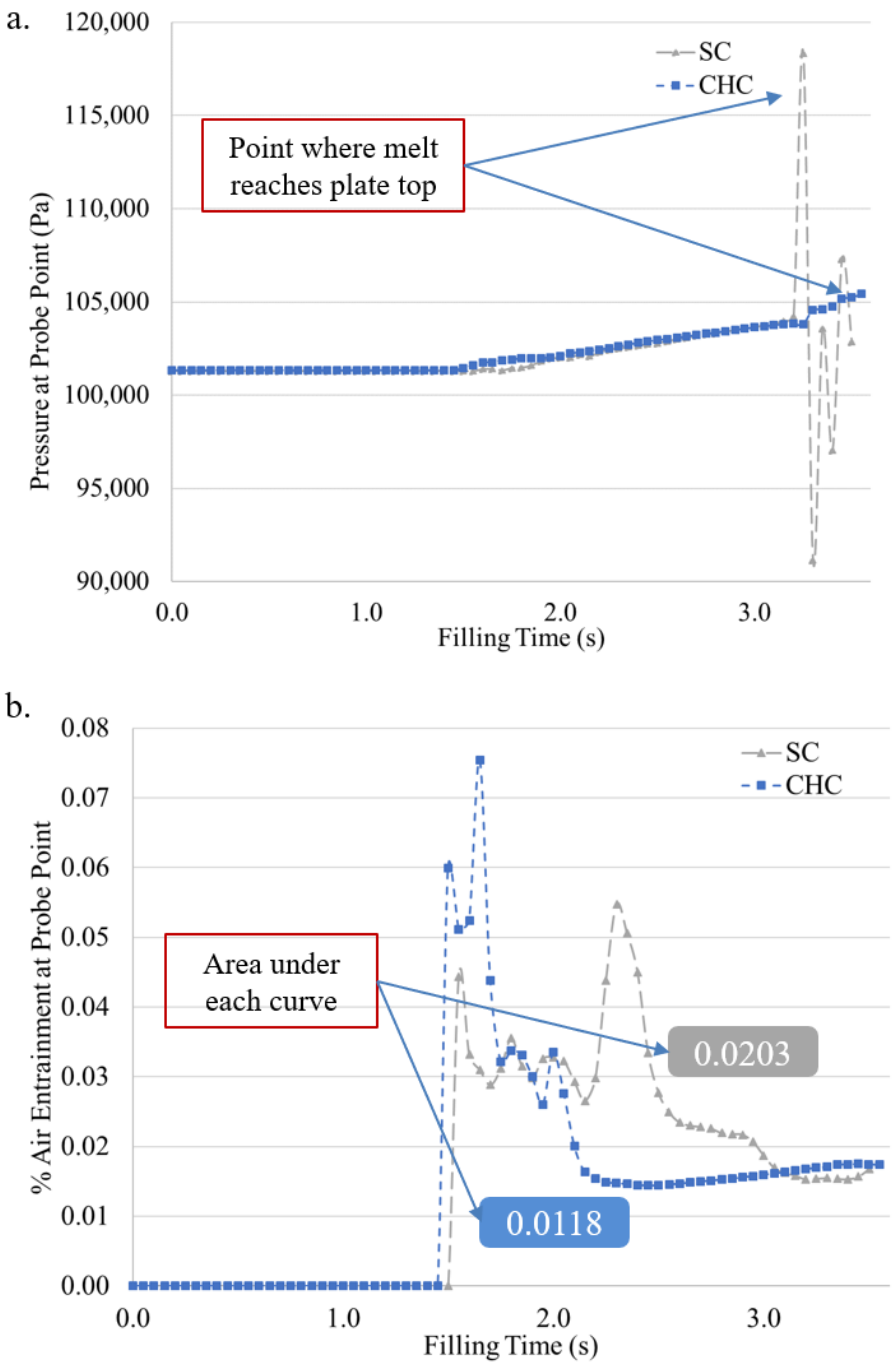

Figure 4-8. (a) Pressure curves at the ingate location of the probe, pressure peak shows time at which aluminum alloy 319 melt reaches the plate top. (b) Peak entrainment at the probe point is maximum for SC, as well as total area under the entrainment curve

4.4.3 Computed Tomography Scanning

The computed tomography (CT) scanning data was processed using open-source ImageJ 1.8.0. The images were converted from 32bit to 16bit and cropped to eliminate scanning artifacts that result from X-ray interaction with the plate edges. Pores were identified in the alloy matrix using three independent binary classification methods based on histogram analysis to validate results. The methods used were the Yen Multilevel Thresholding algorithm (YMT), the Maximum Entropy algorithm (ME) and the Rényi Entropy algorithm (RE). Defect detection is performed slice by slice and pixels are classified as defects by the binary classification algorithms. Fig. 4-9 and 4-10 show views of the defects in the plates cast for Al 316 and gray iron respectively. Average values and standard deviation were calculated using these three algorithms to determine defect volume percentages for each plate (see Fig. 4-11).

Comparison of SC and CHC Al 316 castings show an average reduction of 25% in volumetric defects (See Tables A1 and A2 in Appendix). The pore number and size also are reduced in the CHC sample which indicate that 3DSP novel sprue design resulted in a less turbulent filling process [21]. All defects detected are of macroscopic scale (>109μm) resulting from air entrapment, shrinkage, dissolved gases and dross. The irregular shape and location of defects across the aluminum alloy samples suggest most of the defects originate from internal shrinkage and bifilm formation.

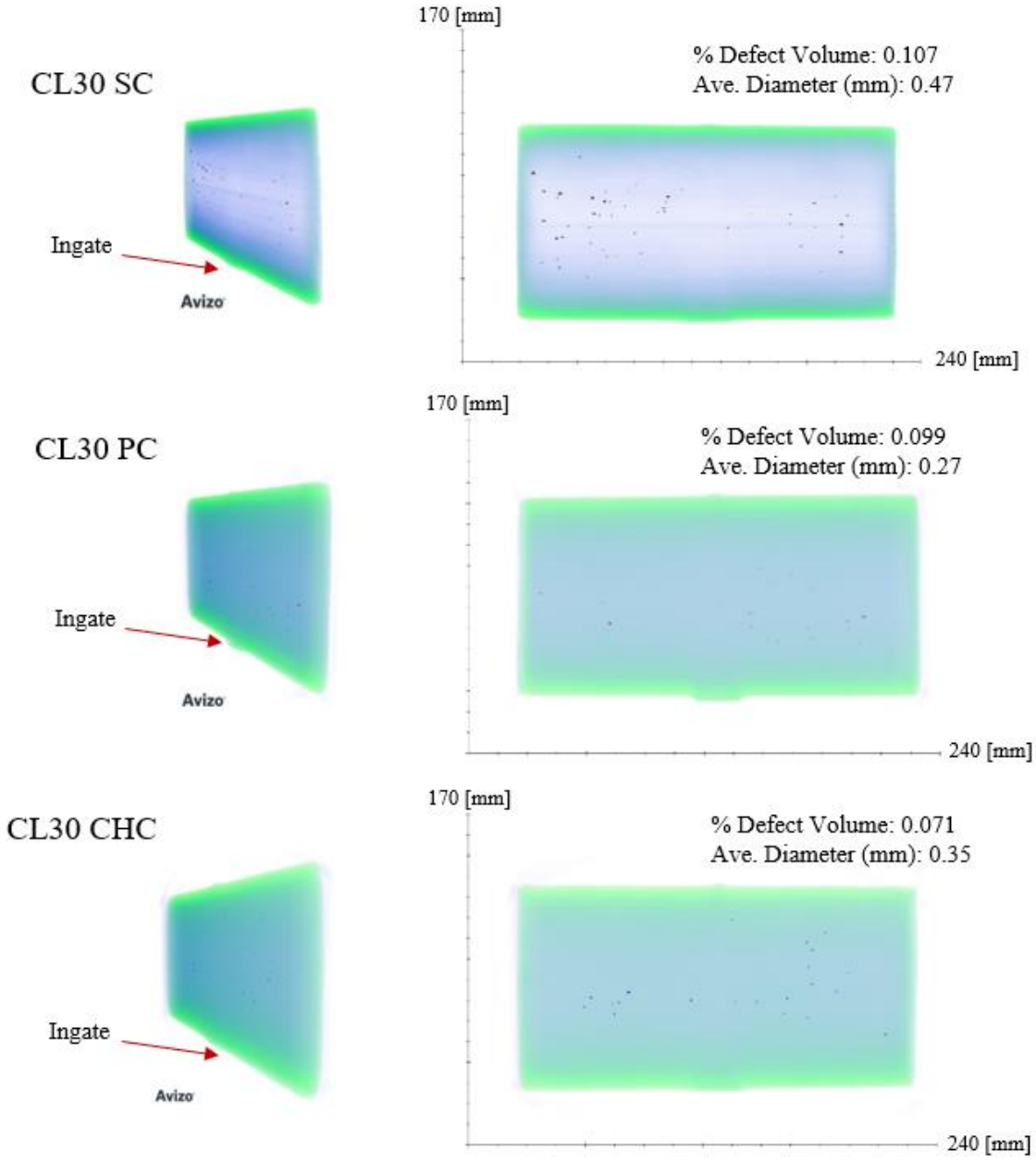

Figure 4-9. Computed tomography results for gray iron samples, percent defect volume and average Feret diameter are obtained using Yen Multilevel Thresholding (YMT) binary classification algorithm. For comparison to the other classification algorithms see table A1 (Appendix A2-1)

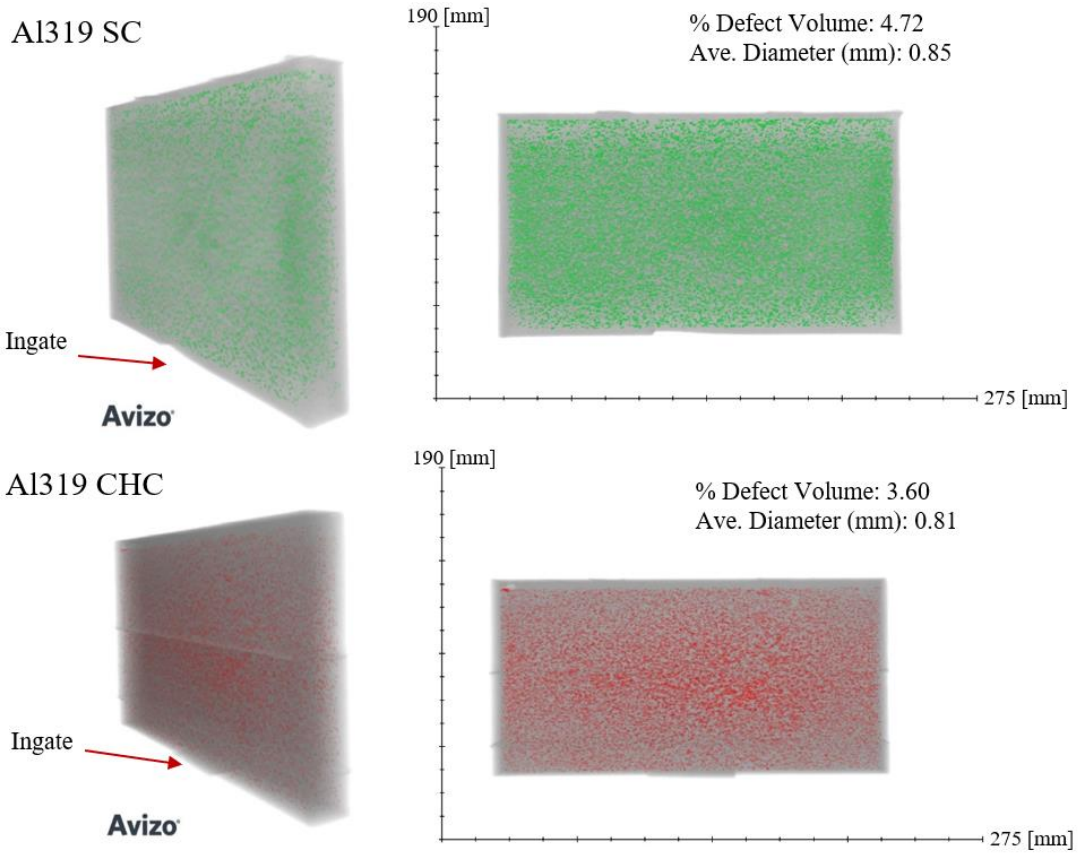

Figure 4-10. Computed tomography results for aluminum alloy 319 samples, percent defect volume and average Feret diameter are obtained using Yen Multilevel Thresholding (YMT) binary classification algorithm. For comparison to the other classification algorithms see table A1 (Appendix A2-2)

As expected, the short freezing range alloy gray iron shows lesser sensitivity to turbulence, and volume of defects is lower than Al 319 castings. However, the influence of novel 3DSP sprue design is evident with a 45.6% in volume of defects when comparing CHC and SC. Regardless of the mold design system, defect volume is <1% in all cases and is in correspondence with typical sound ferrous castings [68].

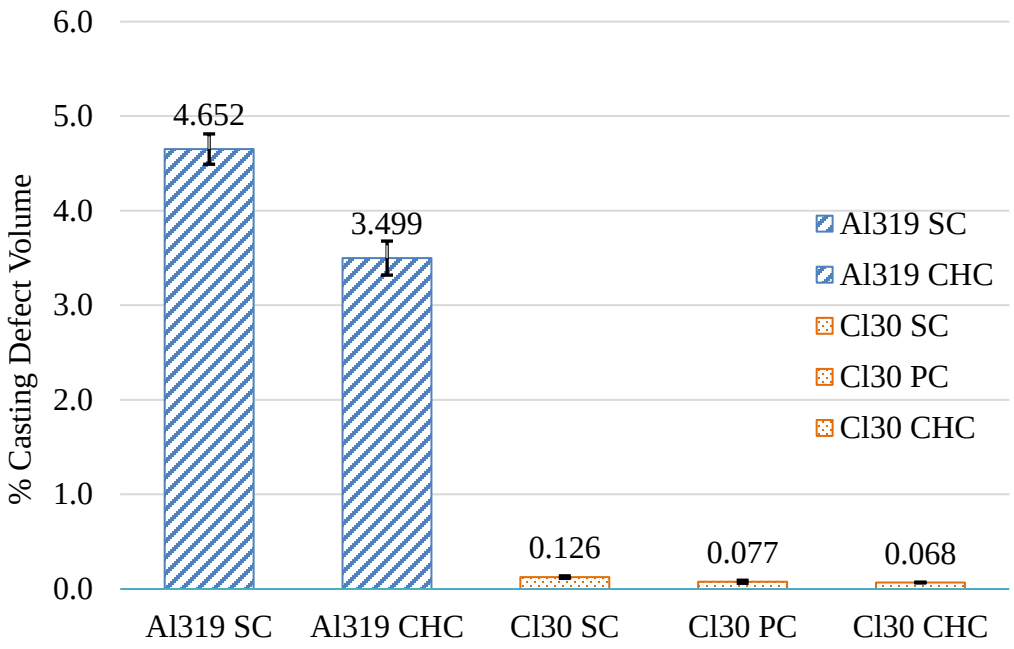

Figure 4-11. Average % defect area density using three independent classification algorithms, error bars show standard deviation

4.4.4 Microstructure

Aluminum alloy 319 microstructure were observed via SEM (see Fig. 4-12) showing similar α-Al matrix in dark gray with cellular formations, eutectic Si is shown in a lighter gray and Cu-based intermetallic phases in white. These observations were confirmed via EDS analysis of the same regions. The internal lamellar structure of Al_2Cu intermetallic phase is clearly observed in Fig. 4-12c. Since the thermal gradient, i.e., solidification rate of the molds was not altered, these results agree with the reported microstructure of this alloy [69,70].

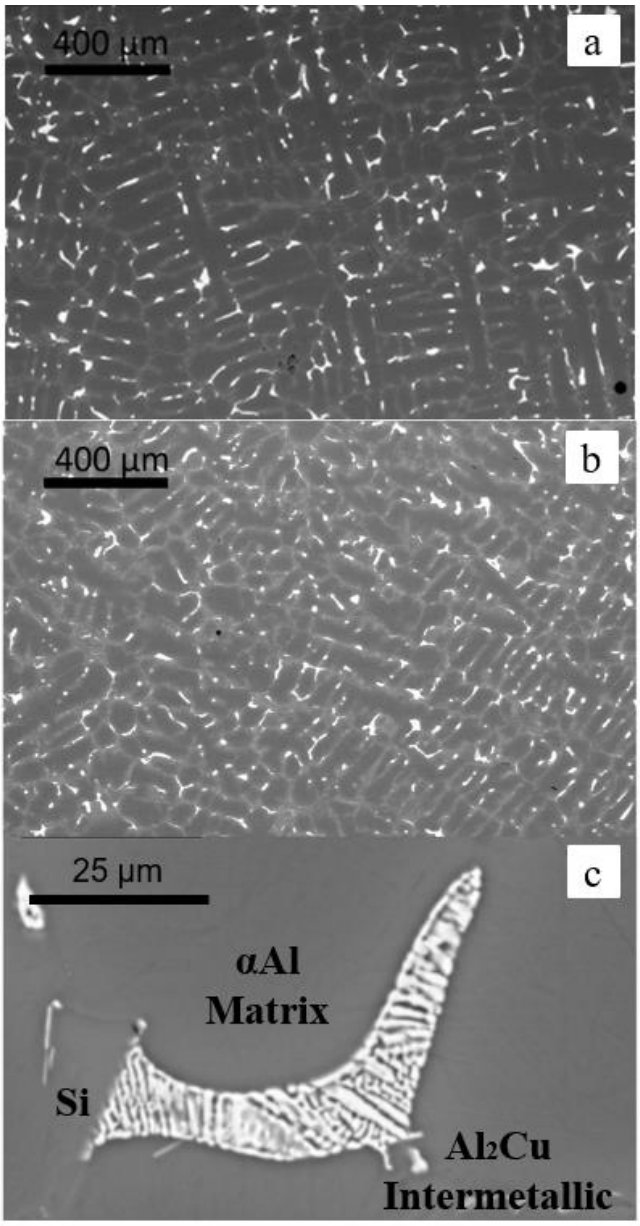

Figure 4-12. Scattered electron microscopy of Al319 samples, CHC at 200x (a), SC at 200x (b) and internal lamellar features of Al_2Cu intermetallic at 5000x imbedded in the aluminum matrix with Si flake visible in the bottom left corner (c)

Similarly, the cast iron (see Fig. 4-13) show identical microstructural formation with coarser graphite flakes 7-10µm thick and a eutectic type flake of coral-like structure [71]. The

presence of undercooled graphite, defined as type D by the ASTM A247 standard [72], indicates high cooling rates. Flake-like graphite is termed type A in the same standard. EDS analysis revealed small inclusions of Mn.

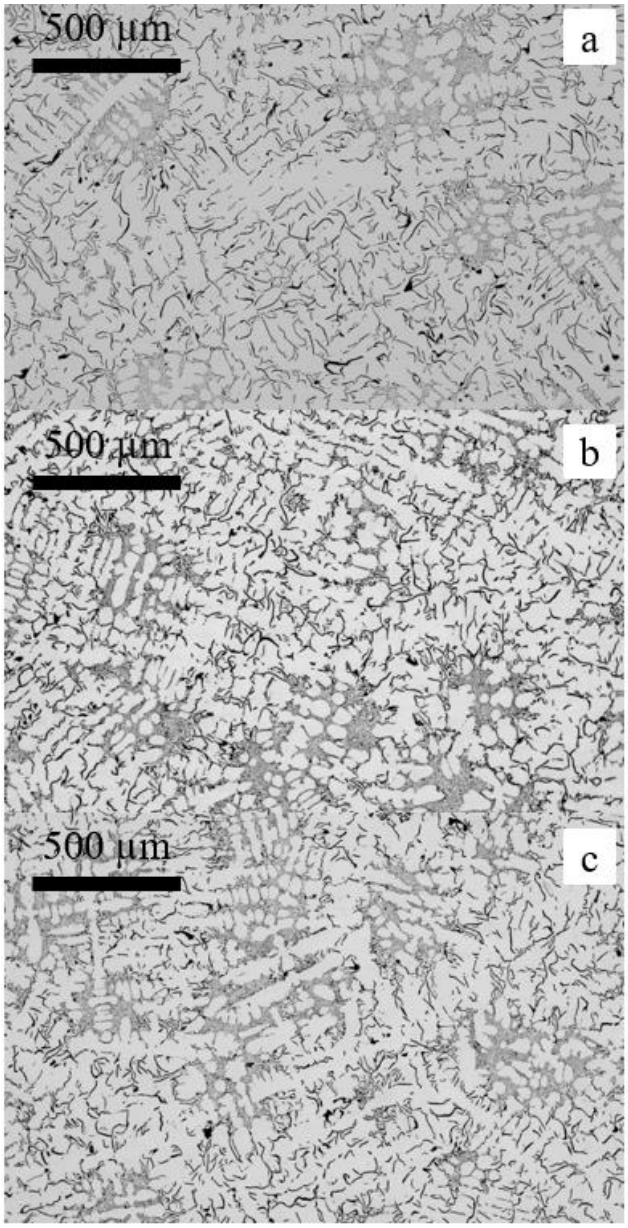

Figure 4-13. SEM of cast iron Cl30 samples, CHC at 200x (a), PC at 200x (b), and SC at 200x (c)

As expected, sprue design does not noticeably affect the microstructural characteristics of these alloys since the filling system will have no appreciable effect on solidification time.

4.4.5 Mechanical Testing

Non-parametric Friedman test was conducted between the two Al 319 mold design (SC and CHC) and three gray iron mold designs (SC, PC and CHC) to evaluate statistical significance between mold design systems. Table 4-2 summarizes the results. The mathematical sprue design increases mean strength by 10% in the aluminum alloy as shown in Fig. 4-14 (p=0.034, 95% CI). Both conical-helix and straight sprues displayed brittle fracture in all tested samples and can be related to porosity detected via CT scanning along center-line of the castings. Porosity has been previously demonstrated to play a highly detrimental role to mechanical strength by acting as crack initiation sites in cast aluminum alloys [70]. In gray iron, parabolic and straight sprues show statistically significant difference of 1.5% in flexural strength. All gray iron samples displayed typical brittle fracture of this alloy [73]. Both Al 319 and gray iron mechanical testing results correlate well with the microstructural and CT scan analysis.

Table 4-2. Friedman tests in Al 319 and Gray Iron (GI) with CI 95%

Material	Sprue Type	Number of Tests	Mean (MPa)	Std. Dev. (MPa)	P-value			
					Al 319	GI CHC/PC	GI PC/SC	GI CHC/PC
Al 319	CHC	8	9.103	1.377	0.034			
Al 319	SC	8	8.235	1.688				
Gray iron	CHC	8	23.459	0.89		0.157		
Gray iron	PC	8	23.416	0.844			0.005	
Gray iron	SC	8	23.771	0.635				0.157

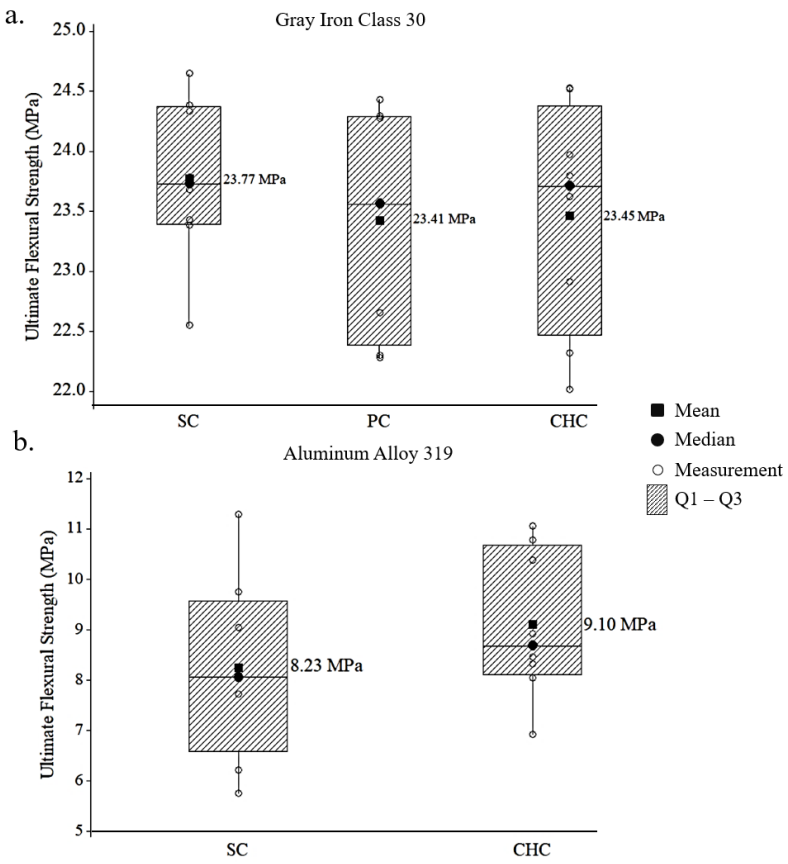

Figure 4-14. Ultimate flexural strength in gray iron (a) and Al 319 (b)

4.5 Conclusion

This study establishes the effects of mathematically designed sprues on alloys with long (e.g., Al 319) and short freezing range alloys (e.g., gray iron CL30). The study shows significant reduction of ingate velocity that can be obtained only by redesigning filling systems during mold design by taking advantage of additive manufacturing via binder jetting, i.e., 3D Sand-Printing (3DSP). This reduction of ingate velocity results in drastically reduced defect volume and increased flexural strength. The main contributions of this research are:

1. Establishing the effectiveness of mathematically designed sprues for reduced filling velocity on a long freezing range alloy (i.e., aluminum alloy 319) and a short freezing range alloy (i.e., gray iron) via numerical flow modeling.

2. Demonstrating reductions in casting defect volume by 32% and 45% for aluminum alloy 319 and gray iron Class 30 respectively, using computer tomography analysis.

3. Establishing an increase in flexural strength of aluminum alloy 319 of 10% when using a mathematically designed sprue for reduced filling turbulence, when compared to a benchmark straight sprue design. No appreciable increase in gray iron Class 30 is observed.

Limitations of this study include a lack of real-time melt flow velocity from experimentation and image analysis via SEM of a reduced area within the casting. Future research efforts will include experimental measurements of ingate velocity as a means of validating numerical and computer simulations. The interaction effect of temperature cooling during mold filling is not accounted for in this study. Its interaction with rigging design will be addressed in future research.

Acknowledgements

The authors would like to thank America Makes for its financial support through AM4MC grant, Hazelton Casting Company for providing the resources for experimentation, FAME Lab for support during casting of the Al319 samples, and the Center for Quantitative Imaging (CQI) - Tim Stecko for his help in acquiring CT scanning data. Thank you to Dr. Robert Voigt for his expert input during the development of this work. Authors also thank Flow 3D-CAST for providing extended research license and PA Department of Community and Economic Development for their (in part) support of this publication.

References

[1] Holtzer M, Danko R, Zymankowka-Kumon S. Foundry industry - Current state and future development. Metalurgija 2012;51:337–40.

[2] Research M. Metal Casting Market by Process (Gravity, High & Low Pressure, Sand), Application (Body Assembly, Engine, and Transmission), Material (Iron, Al, Mg, Zn), Component, ICE & EV (Passenger Car, LCV, HCV, BEV, HEV & PHEV), and Region - Global Forecast to 2025 2018:174. https://www.marketresearch.com/MarketsandMarkets-v3719/Metal-Casting-Process-Gravity-High-11379072/ (accessed October 7, 2019).

[3] Upadhyay M, Sivarupan T, El Mansori M. 3D printing for rapid sand casting—A review. J Manuf Process 2017;29:211–20. doi:10.1016/J.JMAPRO.2017.07.017.

[4] Hackney P, Wooldridge R. 3D sand printing for automotive mass production applications. Int J Rapid Manuf 2017;6:134. doi:10.1504/IJRAPIDM.2017.082156.

[5] Almaghariz ES, Conner BP, Lenner L, Gullapalli R, Manogharan GP, Lamoncha B, Fang, M. Quantifying the Role of Part Design Complexity in Using 3D Sand Printing for Molds and Cores. Int J Met 2016;10:240–52. doi:10.1007/s40962-016-0027-5.

[6] Sama SR, Badamo T, Manogharan G. Case Studies on Integrating 3D Sand-Printing Technology into the Production Portfolio of a Sand-Casting Foundry. Int J Met 2019. doi:10.1007/s40962-019-00340-1.

[7] Mitra S, Rodríguez de Castro A, El Mansori M. On the rapid manufacturing process of functional 3D printed sand molds. J Manuf Process 2019;42:202–12. doi:10.1016/J.JMAPRO.2019.04.034.

[8] Hodder KJ, Chalaturnyk RJ. Bridging Additive Manufacturing and Sand Casting: Utilizing Foundry Sand. Addit Manuf 2019. doi:10.1016/j.addma.2019.06.008.

[9] Sama SR, Wang J, Manogharan G. Non-conventional mold design for metal casting using 3D sand-printing. J Manuf Process 2018;34:765–75. doi:https://doi.org/10.1016/j.jmapro.2018.03.049.

[10] Seifi M, Salem A, Beuth J, Harrysson O, Lewandowski JJ. Overview of Materials Qualification Needs for Metal Additive Manufacturing. JOM 2016;68:747–64. doi:10.1007/s11837-015-1810-0.

[11] Kermanpur A, Mahmoudi S, Hajipour A. Numerical simulation of metal flow and solidification in the multi-cavity casting moulds of automotive components. J Mater Process Technol 2008;206:62–8. doi:https://doi.org/10.1016/j.jmatprotec.2007.12.004.

[12] Ahmad R, Hashim MY. Effect of Vortex Runner Gating System on the Mechanical Strength ff Al-12Si Alloy Castings. Arch Metall Mater 2011;56:991–7. doi:10.2478/v10172-011-0109-6.

[13] David P, Massone J, Boeri R, Sikora J. Gating system design to cast thin wall ductile iron plates. Int J Cast Met Res 2006;19:98–109. doi:10.1179/136404605225023171.

[14] Campbell J. Entrainment defects. Mater Sci Technol 2006;22:127–45. doi:10.1179/174328406X74248.

[15] Nayebi B, Divandari M. Characteristics of dynamically formed oxide films on molten aluminium. Int J Cast Met Res 2012;25:270–6. doi:10.1179/1743133612Y.0000000026.

[16] Liu L, Samuel F. Effect of inclusions on the tensile properties of Al–7% Si–0.35% Mg (A356.2) aluminium casting alloy. J Mater Sci 1998;33:2269–81. doi:10.1023/A:1004331219406.

[17] Campbell J. Chapter 2 - Entrainment. In: Campbell J, editor. Cast. (Second Ed. Second Edi, Oxford: Butterworth-Heinemann; 2003, p. 17–69. doi:https://doi.org/10.1016/B978-075064790-8/50019-X.

[18] American Foundry Society. AFS Casting Scrap Survey Results | American Foundry Society

2014. https://www.afsinc.org/files/AFS/SurveyFiles/castingscrapsurvey.pdf (accessed June 5, 2018).

[19] Masoumi M, Hu H, Hedjazi J, Boutorabi MA. Effect of Gating Design on Mold Filling. AFS Trans 2005:12.

[20] Yang X, Din T, Campbell J. Liquid metal flow in moulds with off-set sprue. Int J Cast Met Res 1998;11:1–12. doi:10.1080/13640461.1998.11819253.

[21] Sama SR, Badamo T, Lynch P, Manogharan G. Novel sprue designs in metal casting via 3D sand-printing. Addit Manuf 2019;25:563–78. doi:https://doi.org/10.1016/j.addma.2018.12.009.

[22] Sabatino M Di, Arnberg L. A review on the fluidity of Al based alloys. Metall Sci Technol 2004;22:9–15.

[23] Sabatino M Di, Arnberg L, Brusethaug S, Apelian D. Fluidity evaluation methods for Al–Mg–Si alloys. Int J Cast Met Res 2006;19:94–7. doi:10.1179/136404606225023345.

[24] Mohiuddin MV, Hussainy SF, Krishnaiah A, Laxminarayana P. Experimental investigation to produce thin-walled sand casting using combination of casting simulation and additive manufacturing techniques. Int J Adv Manuf Technol 2017;90:3147–57.

[25] Dai X, Yang X, Campbell J, Wood J. Effects of runner system design on the mechanical strength of Al–7Si–Mg alloy castings. Mater Sci Eng A 2003;354:315–25. doi:10.1016/S0921-5093(03)00021-2.

[26] Green N, Campbell J. Statistical distributions of fracture strengths of cast Al-7Si-Mg alloy. Mater Sci Eng A - Struct Mater Prop Microstruct Process 1993;173:261–6. doi:10.1016/0921-5093(93)90226-5.

[27] Yang X, Huang X, Dai X, Campbell J, Tatler J. Numerical modelling of entrainment of oxide film defects in filling of aluminium alloy castings. Int J Cast Met Res 2004;17:321–31. doi:10.1179/136404604225022748.

[28] Nyahumwa C, Green NR, Campbell J. Effect of mold-filling turbulence on fatigue properties of cast aluminum alloys. Trans Am Foundrymen's Soc 1998;106:215–24.

[29] Caceres C, Snelling B. Casting defects and the tensile ductility of an Al-Mg-Si alloy. Mater Sci Eng A 1996;220:109–25.

[30] Green NR, Campbell J. Statistical distributions of fracture strengths of cast Al-7Si-Mg alloy. Mater Sci Eng A 1993;173:261–6. doi:10.1016/0921-5093(93)90226-5.

[31] Dojka R, Jezierski J, Campbell J. Optimized Gating System for Steel Castings. J Mater Eng Perform 2018;27:5152–63. doi:10.1007/s11665-018-3497-1.

[32] Modaresi A, Safikhani A, Noohi A, Hamidnezhad N, Mostafa Maki S. Gating System Design and Simulation of Gray Iron Casting to Eliminate Oxide Layers Caused by Turbulence. Int J Met 2016;11. doi:10.1007/s40962-016-0061-3.

[33] Majidi H, Beckermann C. Modelling of air entrainment during pouring of metal castings. Int J Cast Met Res 2017:1–15. doi:10.1080/13640461.2017.1307624.

[34] Hsu F-Y, Lin H-J. A Diffusing Runner for Gravity Casting. Metall Mater Trans B 2009;40:833–42. doi:10.1007/s11663-009-9272-9.

[35] Kleiner S, Ogris E, Beffort O, Uggowitzer PJ. Semi-Solid Metal Processing of Aluminum Alloy A356 and Magnesium Alloy AZ91: Comparison Based on Metallurgical Consideration. Adv Eng Mater 2003;5:653–8. doi:10.1002/adem.200300358.

[36] Kurz W, Fisher DJ. Fundamentals of Solidification. trans tech publications Aedermannsdorf, Switzerland; 2018. doi:10.31399/asm.hb.v09.a0003724.

[37] Ohnaka I, Kang I. Solidification Processing. In: Beech J, Jones H, editors. Proc. 4th Decenn. Int. Conf. Solidif. Process., 1997, p. 346–9.

[38] Chen CP, Tsao C-YA. Semi-solid deformation of non-dendritic structures—I. Phenomenological behavior. Acta Mater 1997;45:1955–68. doi:https://doi.org/10.1016/S1359-6454(96)00312-6.

[39] Reis A, Houbaert Y, Xu Z, Tol R Van, Santos AD, Duarte JF, Magalhaes, AB. Modeling of shrinkage defects during solidification of long and short freezing materials. J Mater Process Technol 2008;202:428–34. doi:https://doi.org/10.1016/j.jmatprotec.2007.10.030.

[40] Bounds S, Moran G, Pericleous K, Cross M, Croft TN. A computational model for defect prediction in shape castings based on the interaction of free surface flow, heat transfer, and solidification phenomena. Metall Mater Trans B 2000;31:515–27. doi:10.1007/s11663-000-0157-1.

[41] Reis A, Xu ZA, Tol R V, Houbaert Y, Duarte JF, Santos AD, Magalhaes, AB. Model for prediction of shrinkage defects in long and short freezing range materials. Int J Cast Met Res 2007;20:171–5. doi:10.1179/136404607X239771.

[42] Khalajzadeh V. Modeling of shrinkage porosity defect formation during alloy solidification. University of Iowa, 2018. doi:https://doi.org/10.17077/etd.by3ja27x.

[43] Campbell J. Review of fluidity concepts in casting. Cast Met 1995;7:227–37. doi:10.1080/09534962.1995.11819183.

[44] Sigworth GK, Wang C. Evolution of porosity in long freezing range alloys. Metall Trans B 1993;24:365–77. doi:10.1007/BF02659139.

[45] Heidarzadeh A, Emamy M, Rahimzadeh A, Soufi R, Sohrabi Baba Heidary D, Nasibi S. The Effect of Copper Addition on the Fluidity and Viscosity of an Al-Mg-Si Alloy. J Mater Eng Perform 2014;23:469–76. doi:10.1007/s11665-013-0794-6.

[46] Ravi KR, Pillai RM, Amaranathan KR, Pai BC, Chakraborty M. Fluidity of aluminum alloys and composites: A review. J Alloys Compd 2008;456:201–10. doi:https://doi.org/10.1016/j.jallcom.2007.02.038.

[47] Kim JM, Kim DG, Kwon HW, Loper CR. Pore behavior at the solid/liquid interface during solidification. Scr Mater 1998;39:969–75. doi:https://doi.org/10.1016/S1359-6462(98)00242-5.

[48] Di Sabatino M. Fluidity of Aluminium Foundry Alloys. Norwegian University of Science and Technology, 2005.

[49] Dinsdale A, Quested P. The viscosity of aluminium and its alloys—A review of data and models: Special Section: Proceedings of the 2003 International Symposium on Liquid Metals (Guest Editors: P. D. Lee, A. Mitchell, A. Jardy, J.-P. Bellot). J Mater Sci 2004;39. doi:10.1023/B:JMSC.0000048735.50256.96.

[50] Barfield R. The Viscosity of Liquid Iron and Iron Alloys. Imperial College, 1954.

[51] Campbell J. Invisible macrodefects in castings. J Phys Iv - J PHYS IV 1993;03. doi:10.1051/jp4:19937135.

[52] Runyoro J, Boutorabi SMA, Campbell J. Critical gate velocities for film-forming casting alloys. A basis for process specification. Trans Am Foundrymens Soc 1992;100:225–34.

[53] Tiryakioglu M, Askeland D, Ramsay CW. Fluidity of 319 and 356: An Experimental Design Approach. AFS Trans 1995;102:17–25.

[54] Turchi PA. Viscosity and Surface Tension of Metals, Technical Report LLNL-TR-750486, Livermore, CA, USA, 2018.

[55] Hatch JE. Aluminum : properties and physical metallurgy. Metals Park, OH: American Society for Metals; 1984.

[56] Saeger CM, Ash EJ. Properties of Gray Cast Iron as Affected by Casting Conditions, Research Paper RP726, J. Res. Nat. Bur Stand., vol. 13. 1934.

[57] Hellström K, Diószegi A, Diaconu L. A Broad Literature Review of Density Measurements of Liquid Cast Iron. Metals (Basel) 2017;7:20. doi:10.3390/met7050165.

[58] Nakagawa Y, Suzuki K, Momose A. Study on the Viscosity of Molten Iron. Trans Japan Inst Met 1968;9:67–72. doi:10.2320/matertrans1960.9.67.

[59] Fox B. Air Entrainment Analysis. Flow Sicence, Inc 2018:https://users.flow3d.com/flow-3d-technical-webinar.https://users.flow3d.com/flow-3d-technical-

webinars/airentrainment-analysis/ (accessed July 7, 2019).

[60] Yen J-C, Chang F-J, Chang S. A new criterion for automatic multilevel thresholding. IEEE Trans Image Process 1995;4:370–8. doi:10.1109/83.366472.

[61] Pun T. A new method for grey-level picture thresholding using the entropy of the histogram. Signal Processing 1980;2:223–37. doi:https://doi.org/10.1016/0165-1684(80)90020-1.

[62] Pun T. Entropic thresholding, a new approach. Comput Graph Image Process 1981;16:210–39. doi:https://doi.org/10.1016/0146-664X(81)90038-1.

[63] Kapur JN, Sahoo PK, Wong AKC. A new method for gray-level picture thresholding using the entropy of the histogram. Comput Vision, Graph Image Process 1985;29:273–85. doi:https://doi.org/10.1016/0734-189X(85)90125-2.

[64] ASTM. E290-09: Standard Test Methods for Bend Testing of Material for Ductility 2009:1–10. doi:10.1520/E0290-14.

[65] ASM International. Casting Design and Performance. First Edit. Materials Park, OH: ASM International; 2009.

[66] Sun W, Bates CE. Visualizing defect formation in gray iron castings using real time X-rays. Trans Am Foundry Soc 2003;111:859–67.

[67] Sirrell B, Holliday M, Campbell J. Benchmark testing the flow and solidification modeling of AI castings. JOM 1996;48:20–3. doi:10.1007/BF03222885.

[68] Campbell J. Origin of Porosity in Cast Metals. University of Birmingham, 1967.

[69] Li Z, Samuel AM, Samuel FH, Ravindran C, Valtierra S. Effect of alloying elements on the segregation and dissolution of CuAl2 phase in Al-Si-Cu 319 alloys. J Mater Sci 2003;38:1203–18. doi:10.1023/A:1022857703995.

[70] Ammar HR, Samuel AM, Samuel FH. Effect of casting imperfections on the fatigue life of 319-F and A356-T6 Al–Si casting alloys. Mater Sci Eng A 2008;473:65–75. doi:https://doi.org/10.1016/j.msea.2007.03.112.

[71] Fraś E, Górny M. Inoculation Effects of Cast Iron. Arch Foundry Eng 2012;12:39–46. doi:10.2478/v10266-012-0104-z.

[72] ASTM International. ASTM A247-19, Standard Test Method for Evaluating the Microstructure of Graphite in Iron Castings 2019. doi:10.1520/A0247-19.

[73] Altenbach H, Stoychev GB, Tushtev KN. On elastoplastic deformation of grey cast iron. Int J Plast 2001;17:719–36. doi:https://doi.org/10.1016/S0749-6419(00)00026-7.

Chapter 5

Conclusions and Future Work

As Additive Manufacturing (AM) technologies are integrated into the mainstream manufacturing, hybrid productive methods will need to be developed in order exploit fully the advantages of the technology. By combining AM processes such as 3D Sand-Printing (3DSP) with conventional manufacturing technologies like as metalcasting, both technologies benefit from each other. On the one hand, AM offers the freedom of design and manufacturing molds of great geometric complexity and control of thermo-mechanical properties on the sand molds, while traditional metalcasting offers its variety of certified alloys and the possibility of casting large metal components that cannot be fabricated with any other AM process at the same cost. Chapter 1 highlighted some of the aspects where this integration has been achieved in the past and indicates areas where the manufacturing control that 3DSP offers can still be taken advantage of.

Chapter 2 proposes a novel approach to 3DSP mold design, by considering the fact that printing parameters can be engineered to modify mechanical, thermal and pore properties of the mold. This feature of 3DSP is explored by modifying the binder concentration during printing. As binder deposition was increased during printing, the dimensional accuracy of the printed parts diminished. Meanwhile, binder concentration increased mechanical strength both in the tensile and flexural experiments. Highest mechanical performance was obtained for the binder level B_5, containing wt.% 2.76 of furanic binder. However, this increased mechanical strength comes at the cost of significant reductions in permeability. No change in pore structure was observed across binder levels in the Mercury Intrusion Porosimetry (MIP) test, where all samples showed a pore mean size between 56µm and 62µm. Thermal conductivity and heat capacity at room temperature tended to increase as binder concentration increased. As the molds degraded due to temperature rise, thermal conductivity was observed to diminish in all the tested samples. This occurred after

the temperature cycle surpassed the binder decomposition temperature (180 °C). Using thermal conductivity and heat capacity in combination with density results obtained from Helium Pycnometry tests, the heat accumulation coefficient of 4 of the binder levels was calculated, these results fall in the middle range of typical rammed sand molds. Heat accumulation coefficient varied between 1120 and 1500 $Ws^{-0.5}m^{-2}K^{-1}$ when binder presence varied between 1.48 and 2.74 wt.%. Finally, a framework for a novel approach to metalcasting mold design by applying Design for Additive Manufacturing (DfAM) concepts was presented, where point-by-point control of binder deposition can permit variations in mechanical strength and permeability across the mold.

The objective of Chapter 3 was to delve deeper into the effects of binder on the pore network characteristics of a 3DSP sample. Since in the previous chapter, MIP could not provide sufficient differentiation in pore space properties and because from this test, no knowledge of the geometry of pores can be obtained, micro-Computed Tomography (CT) Scanning was selected to fill this knowledge gap. Micro-CT was used to obtain high-resolution 3D images of 6 samples of different binder concentration. Using image analysis tools, it was observed that void space volume varies between 39% and 43%, and reduces with binder concentration. A very small portion of this void space was observed to be unconnected porosity, regardless of the content of binder. This unconnected porosity does not benefit degassing of the mold. Very similar Pore Size Distribution and Neck Size Distribution was observed in all cases. The 3D images were then used to run permeability simulations. These simulations represent flow of gas generated during burnout as the molten metal interacts with the mold and cores. By applying a differential pressure across the analyzed volume, permeability, tortuosity, pressure distribution and gas velocity vector fields were observed. Absolute permeability ranged between 130 and 150 μm^2 and was dependent on the direction in which the flow simulation was performed. Minimum permeability was observed in the z direction, the printing direction, with a reduction by 20% in some cases, when compared to the permeability in the directions within the printing plane. This study also highlighted the need for

high-resolution scanning at 5 μm voxel size or lower, in order to achieve enough differentiation in grayscale between open spaces and solidified furanic binder.

Chapter 4 presented a second approach to mold design by taking advantage of 3DSP. Complex sprue designs were utilized to increase mechanical performance of castings and reduce defects generated during mold filling, by controlling melt flow behavior. The aim of this chapter was to experimentally verify the effects of using non-conventional sprue designs (i.e., conical-helix and parabolic sprues) for casting alloys of very different flow behaviors and solidification patterns. Using an analytical approach to estimate the velocity of the melt at the sprue bottom, molds with optimized sprue geometry were designed for long-freezing range and short-freezing range alloys. By using different characterization techniques such as numerical simulation, scanning electron microscopy, energy-dispersive spectroscopy, mechanical testing and computed tomography, a clearer understanding of the effect of these gating systems on turbulence control was obtained. In the case of long-freezing range alloys (i.e., aluminum alloy 319) a much stronger influence was observed than in the short-freezing range alloy (i.e., gray iron Class 30). Only in the first case was a significant increase in mechanical strength observed. When comparing a casting poured using benchmark straight sprue, the mathematically design conical-helix sprue increased the flexural strength by 10%. In gray iron Class 30, although the casting defect volume was seen to diminish, no substantial increase in mechanical performance was observed.

This thesis represents an effort towards advancing metalcasting by utilizing the design freedom and 3D printed mold properties to increase mechanical performance of metal components. At the same time, it calls attention to areas where 3DSP remains to be researched, some of these aspects are mentioned here.

If framework proposed in Chapter 2 is to be realized, point-by-point control of binder deposition during 3DSP will need to be developed. An algorithm for continuous binder deposition gradation will need to be integrated into the 3DSP software.

Efforts should be directed towards multi-objective topology optimization algorithms that can consider mold strength, permeability and thermal properties, in order automate the process of mold printing parametrization.

In the process of researching what has been presented in Chapter 3, it was observed that binder is very difficult to segment during CT image analysis. Grayscale values of binder are very similar to the surrounding air within the 3DSP sample. In order to achieve higher contrast to facilitate image analysis, the samples could be flooded with a liquid or gas that would allow for clear distinction between sand grains, solidified binder and open spaces.

The previous point can be extended further, by using a 4D scanning approach. This would involve live observation of gas flow across the samples during a period of time. These results could be used to validate numerical gas flow simulations as performed in Chapter 3.

The analytical model, used in Chapter 4, for sprue optimization can be extended to runner geometries, by optimizing length and number of runners that feed one or multiple castings.

It remains unclear whether the explored sprue geometries can be applied across different ranges of casting sizes. The effects on pressure head will need to be examined in future work.

During flow simulations, it was observed in many instances that a bounce-back wave was generated as the runner extension was filled. This returning wave was responsible for the fountaining effect at the casting ingate. This effect should be investigated further and efforts should be directed to redesigning runner extension to dampen bounce-back while at the same time retaining the initial melt that has been in contact with the air for the longest time. If this can be achieved, cleaner melt will enter the mold while oxide films, entrained sand and air bubbles will be trapped at the runner end.

Appendix

Table A1. Image analysis results for aluminum alloy 319

Algorithm	Sprue Type	Total Volume (mm^3)	Total Defects Volume (mm^3)	Average Pore Area (mm^2)	N_P (mm^{-3})	Average Feret Diameter (mm)	ρ_p (%)	Change in ρ_p (%)
YMT	CHC	209 089.03	6 788.82	0.267	1.090	0.788	3.246	-26.72
	SC	264 480.70	9 262.98	0.287	1.183	0.835	4.430	
ME	CHC	209 089.03	7 537.32	0.282	1.127	0.810	3.604	-23.70
	SC	264 480.70	9 878.24	0.299	1.119	0.852	4.724	
RE	CHC	209 089.03	7627.99	0.283	1.167	0.813	3.648	-24.04
	SC	264 480.70	10043.76	0.302	1.135	0.856	4.803	

Table A2. Image analysis results for gray Class 30

Algorithm	Sprue Type	Total Volume (mm^3)	Total Defects Volume (mm^3)	Average Pore Area (mm^2)	NP (mm^{-3})	Average Feret Diameter (mm)	ρ_p (%)
YMT	CHC	72 859.15	5.697	0.076	0.0087	0.359	0.071
	PC	72 859.15	8.006	0.051	0.0222	0.271	0.099
	SC	72 859.15	8.584	0.142	0.0079	0.475	0.107
ME	CHC	72 859.15	4.987	0.076	0.0081	0.352	0.062
	PC	72 859.15	5.027	0.099	0.0075	0.402	0.062
	SC	72 859.15	10.57	0.135	0.0100	0.464	0.132
RE	CHC	72 859.15	5.781	0.074	0.0104	0.345	0.072
	PC	72 859.15	5.535	0.098	0.0087	0.393	0.069
	SC	72 859.15	11.088	0.135	0.0105	0.458	0.138

Table A3. List of Relevant Papers

Under Review:

1. Martinez, D., Sama, S. R., Toykoc, H., Sim, J., & Manogharan, G. (2019). Novel Mold Design to Improve Mechanical Properties in Castings
2. Martinez, D., Bate, C., & Manogharan, G. (2019). Towards Functionally Graded Sand Molds for Metal Casting: Engineering Thermo-Mechanical Properties using 3D Sand Printing
3. Martinez, D., Stecko, T., & Manogharan, G. (2019). Pore Networks in 3D Sand-Printed Molds – A Computed Tomography Scanning Study

Table A4. Table of Authors

Author	**Department**	**University/Company**
Daniel Martinez	Mechanical Engineering	Penn State
Santosh Reddy Sama	GE Transportation	GE Transportation
Hakan Toykoc	Industrial Engineering	Penn State
Jay Sim	Mechanical Engineering	Penn State
Casey Bate	MC Dean Inc.	MC Dean Inc.
Timothy Stecko	Center for Quantitative Imaging (EESL)	Penn State
Guha Manogharan	Mechanical Engineering	Penn State